Constraints on Crustal Stress From Coseismic Slip Models and Focal Mechanisms

by

Lorena Medina Luna

A dissertation submitted in partial fulfillment
of the requirements for the degree of
Doctor of Philosophy
(Geology)
in the University of Michigan
2015

Doctoral Committee:

Assistant Professor Eric A. Hetland, Chair
Assistant Professor Jeremy Bassis
Associate Professor Marin Clark
Professor Jeroen Ritsema
Professor Ben A. van der Pluijm

To my family and friends,

near and far,

on earth and gone,

and to all those curious minds

that ask what earthquakes are.

Para mi familia, amigas y amigos,

cerca y lejanos,

en la tierra y en el cielo,

y por todos los que preguntan,

porqué tiembla la tierra.

ACKNOWLEDGEMENTS

I would like to thank my parents, family, and friends for their love, support and words of encouragement. To my soon-to-be husband, thank you for your patience and motivational talks, we survived the Ph.D process!

I thank my advisor for setting the bar high and for his guidance in helping me achieve my goals towards completion of the Ph.D. Thank you for nominating me as a Rackham Merit Fellow which helped fund three years of my education and research. Additional funding for research was made possible by two NSF grants to E. Hetland: (1) EAR 1045372, The Dependence of Surface Deformation on Rheology Throughout the Seismic Cycle; and (2) EAR 1245263, Postseismic Deformation at the İzmit-Düzce, Turkey Earthquake Sequence: Implications for the Mechanics of the Earthquake Cycle and Rheology of the Continent.

To all the professors, faculty, and staff at the University of Michigan whom I have met, I am grateful that I got to know you. Thank you for your mentorship, conversations, and help throughout my time at the university.

Lastly, I would like to thank the members of my committee who have provided me with feedback during our annual meetings towards the completion of this dissertation.

PREFACE

The department of Earth and Environmental Sciences was previously known as the department of Geological Sciences.

The degree conferred from completion of this dissertation is a Ph.D. in Geology with a focus in Geophysics. Within the Geophysics research group, I worked in the crustal mechanics and lithospheric dynamics group (CMLD) under the direction of Eric A. Hetland.

This dissertation encompasses partial work completed over the course of my 4.5 years at the University of Michigan. The Bayesian Monte Carlo estimation techniques developed to estimate crustal stress from earthquake data were applied extensively on coseismic slip models and focal mechanisms of the 2011 Tohoku-Oki earthquake, but were not discussed in the chapters of this dissertation. Coseismic stress change inferences from parts of that work can be found in a co-authored paper: L. Bai, L. Medina Luna, E. A. Hetland, and J. Ritsema, (2013). Focal depths and mechanisms of Tohoku-Oki aftershocks from teleseismic P wave modeling. Earthquake Science, 27, p. 1-13, doi: 10.1007/s11589-013-0036-x. Preliminary results were presented at various conferences from 2011-2013.

"...it starts with an earthquake..."

—R.E.M.

TABLE OF CONTENTS

LIST OF FIGURES

Figure

LIST OF TABLES

Table

LIST OF APPENDICES

Appendix

ABSTRACT

Constraining crustal stress that leads to earthquakes is an active area of research with profound implications on understanding the forces that deform the surface of the earth and generate slip on faults. Surface deformation related to strain accumulation on faults prior to, during and following earthquakes are recorded geodetically (InSAR and GPS). These data are used to infer fault geometries and models of coseismic slip of an earthquake. Seismic energy radiated during earthquakes are used to produce focal mechanisms, which are geometric representations of faults, and provide insight on stress changes due to earthquakes. However, earthquakes are the response to stress accumulation on faults, but direct measurements of accumulated stress are difficult. In this dissertation, I develop, test, and apply a Bayesian Monte Carlo (BMC) estimation technique to infer crustal stress from both focal mechanisms and coseismic slip models, the latter of which has never been done prior to the work I present here.

I apply the BMC method to investigate stresses leading to the 2008 Wenchuan, China, earthquake, and to the 1999 İzmit and Düzce, Turkey, earthquakes. I use various coseismic slip models from all three events, aftershock focal mechanisms of the Wenchuan earthquake, and seismicity recorded in the Sea of Marmara, adjacent to the İzmit earthquake. I find that a homogeneous stress is statistically consistent with slip during the Wenchuan earthquake, and that heterogeneous stresses along the trace of the mainshock, previously argued for based on aftershock focal mechanisms, may simply reflect ambiguities in the interpretation of stress from focal mechanisms.

Coseismic slip models from the İzmit and Düzce earthquakes are also consistent with a homogeneous stress along all fault segments that slipped in those earthquakes, particularly if the coefficient of fault friction is about 0.2 or less. In the Sea of Marmara, inferred stresses from focal mechanisms indicate that stress differs from the eastern to the western segments of the Main Marmara fault. Additionally, results indicate a potential stress rotation along the western segment between about 1999 and 2003, towards a transform stress regime similar to the stress leading to the İzmit and Düzce earthquakes.

CHAPTER 1

Introduction

Earthquakes occur on pre-existing planes of weakness in the Earth's crust, rupturing different fault geometries along different fault lengths, but are all due to accumulated stress on the faults. Inferring stress from earthquakes is an active area of research, and although we have a plethora of data from prehistoric and recent seismicity, each study provides only part of the answer to the following two questions: Why do earthquakes occur the way they do? Knowing how a fault previously slipped and the stresses that led to that earthquake, can we say anything about the potential for future fault failure?

In this dissertation, I consider both geodetic and seismological constraints to estimate stress along the Longmenshan fault zone (LMSfz) in China, and along the western North Anatolian fault in Turkey. Heterogenous slip during the Wenchuan earthquake, in the LMSfz, begs the question of whether heterogeneous stresses are partitioned along the rupture zone, or whether geometric complexities dominate the diversity in slip. The diversity in aftershock focal mechanisms along the LMSfz may not directly reflect regional stresses, but rather stress changes following the Wenchuan earthquake. We therefore incorporate the use of coseismic slip models to understand the stresses leading to the Wenchuan earthquake and focal mechanisms of seismicity that followed, keeping in mind that stress inferences using focal mechanisms may lead

to ambiguities in the interpretation of stress.

Earthquakes have progressively migrated from east to west along the North Anatolian fault culminating in the 1999 İzmit and Düzce earthquakes (e.g., Barka, 1996; Stein *et al.*, 1997; Ayhan *et al.*, 2001; Şengör *et al.*, 2005). An earthquake to the west of the İzmit rupture in the Sea of Marmara is expected in the future, and poses a seismic risk for the city of İstanbul (e.g., Stein *et al.*, 1997; Parsons *et al.*, 2000; Hubert-Ferrari *et al.*, 2000; King *et al.*, 2001; Le Pichon *et al.*, 2003; Şengör *et al.*, 2005). We therefore consider seismicity in the Sea of Marmara to understand the stress localized on recently unruptured faults to test whether the same stress that led to the İzmit and Düzce earthquake sequence is also loading the faults in the Sea of Marmara.

This thesis is self contained in that it develops, tests, and applies a Bayesian Monte Carlo (BMC) estimation of stress from earthquake data with a novel application to coseismic slip models. Additionally, I investigate the ambiguities in stress inferences when using focal mechanisms using synthetic focal mechanisms. In the following sections, I first briefly define earthquakes and the data recorded from them. Second, I discuss how data collected from earthquakes has been used to infer crustal stress. I finally summarize the three research chapters in this dissertation.

1.1 Generation of Earthquakes and Data Acquisition

Earthquakes occur when a stress threshold on a fault exceeds the frictional resistance of fault movement (Anderson, 1951; Jaeger and Cook, 1979). Fault slip occurs in a matter of seconds to minutes (earthquakes), or over periods of days to months (aseismic creep or slow slip). The rapid slip generates seismic waves that are recorded by seismometers, and are what we feel as an earthquake. Aseismic creep or slow slip events can be recorded by global positioning system (GPS) instruments. What causes regions to slip seismically or by creep is not fully understood (Schleicher *et al.*, 2010;

Çakir *et al.*, 2012).

Direct measurements of accumulated stress are difficult to obtain; however, geodetic (Interferometric Synthetic Aperture Radar [InSAR] and GPS) measurements of ground deformation can be used to infer patters of strain accumulation (e.g. Meade and Hager, 2005) which can be used to infer earthquake potential on faults. Therefore, regions exhibiting surface strain accumulation, and thus stress accumulation on faults, are of concern because these areas have the propensity for future fault failure. Paleoseismology provides a historical record of seismicity along fault zones from which a recurrence interval of earthquakes is estimated (e.g. Weldon *et al.*, 2004). Data from both geodesy and paleoseismology provide information on the earthquake potential of a region, and thus its seismic hazard. Relating surface strain to stress is dependent on mechanical models of fault loading, and although current implementation of paleoseismic studies are incorporated into seismic hazard assessment, these mechanical models are rarely used in earthquake hazard assessments.

The sense of slip motion on a fault (*i.e.*, transform, extension, compression), depends on the orientation of principal stresses acting on the lithosphere. Stress can be defined by three principal components, most, intermediate, and least compressive stress (MCS, ICS and LCS, respectively; Figure 1.1). In the idealized Andersonian view of faulting (Anderson, 1951), transform regimes are characterized by horizontal MCS and LCS with a vertical ICS, and thus two crustal blocks slide horizontally past each other along a near vertical fault (Figure 1.1a). Extensional regimes are characterized by a vertical MCS with horizontal ICS and LCS, where one crustal block, the hanging wall, slides down relative to the other, the footwall (Figure 1.1b). Compressional regimes are characterized by horizontal MCS and ICS with a vertical LCS, where the hanging wall slides up relative to the footwall (Figure 1.1c).

Fault zones are composed of multiple fault segments and fault splays on pre-existing fractures in the crust that are prone to slip. Under the same state of stress,

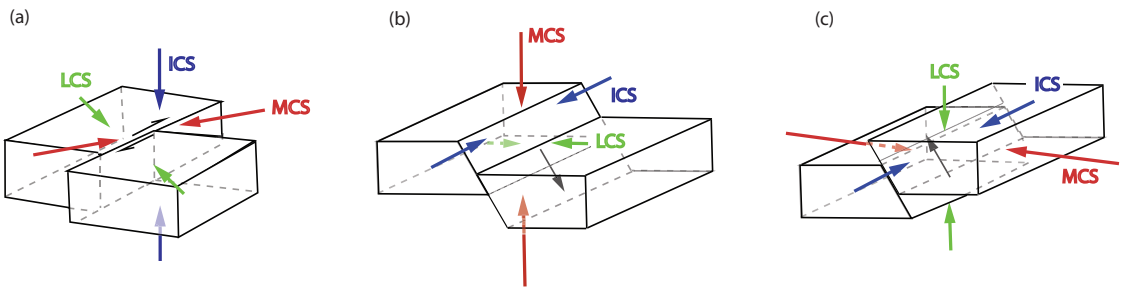

Figure 1.1: Illustration of principal stresses on a crustal body. MCS, ICS and LCS are the most, intermediate and least compressive stresses, respectively. Orientation of principal stress at which an optimally oriented fault will fail as (a) strike slip, (b) normal slip, and (c) thrust slip. Magnitudes of MCS, ICS, and LCS are σ_1, σ_2, and σ_3, respectively ($\sigma_1 \leq \sigma_2 \leq \sigma_3 \leq 0$ for compressive stresses).

multiple fault segments oriented in different manners can slip as different mechanisms (McKenzie, 1969; Michael, 1984). Field observations of fault scarps help identify the geometry of fault segments and direction of slip. This is done by measuring the orientation of offset surface features and/or slickensides/striations on rock exposures (scratches on the rock surface caused by grinding of material between two surfaces).

The waves produced by earthquakes, recorded on seismograms, are also used to produce geometric representations of faults. The radiation pattern of seismic waves can be used to estimate a point-source fault plane solution, or focal mechanism, that is the geometric representation of the faults that slipped. The focal mechanism provides two possible fault plane orientations and fault slip directions. Deciphering which of the two planes is the slip surface is not possible without prior knowledge of the regional geology, tectonic history, field observations of exposed offset features, or finite fault modeling of the region. A cluster of aftershocks has the potential to delineate a fault zone, however since faults are an amalgamation of pre-existing fractures in the crust, it is not possible to uniquely determine which plane of any given focal mechanism slipped.

The assumption of a point source and constant slip rake in a focal mechanism solution does not properly describe the slip in large earthquakes. Geodetic data,

such as InSAR and GPS are used to measure the ground deformation during large earthquakes (e.g., Reilinger *et al.*, 2000; Delouis *et al.*, 2002; Çakir *et al.*, 2003a, 2003b; Feng *et al.*, 2010; Tong *et al.*, 2010; Zhang *et al.*, 2011). These data can be used to infer fault geometry and coseismic slip along the faults at depth, thereby resolving the nodal plane ambiguity from focal mechanisms. Field observations, seismometer recordings, and coseismic slip models can all be used to estimate the stress that leads to earthquakes. However, coseismic slip models have not been used prior to the work I present in Chapter 2.

1.2 Estimation of Stress

Stresses that lead to earthquakes are inferred using field observations (Angelier, 1979), focal mechanisms (Gephart and Forsyth, 1984; Michael 1984), coseismic slip models (Medina Luna and Hetland, 2013), and where available, in situ measurements of stress from boreholes (McGarr and Gay, 1978).

From multiple rock exposures, Angelier (1979) used the orientation of slickensides to estimate stress via linear least squares. It is assumed that slip occurs in the direction of the maximum shear stress applied on the fault surface (Bott, 1959; McKenzie, 1969; Angelier, 1979; Gephart and Forsyth, 1984) and that slip on multiple fault surfaces is due to a uniform state of stress (McKenzie, 1969; Angelier, 1979).

The well established techniques of Gephart and Forsyth (1984) and of Michael (1984, 1987) use linear least squares to invert for stress from focal mechanisms. Although quadrants of a focal mechanism delineate the compressional and tensional regimes, the direction of the principal stresses can lie anywhere in the corresponding focal quadrant (McKenzie, 1969). To better constrain stress using least squares, Célérier (1988) demonstrated that at least four focal mechanisms should be used. To account for uncertainty in the stress estimation, Michael (1984, 1987) incorporated a bootstrapping technique. Recently Arnold and Townend (2007) proposed a Bayesian

estimation of stress from focal mechanisms, resulting in a probability density function of stress.

1.3 Objectives of the Dissertation

In this dissertation, I describe the development and implementation of a BMC estimation technique, (Chapter 2; Medina Luna and Hetland, 2013) similar to that of Arnold and Townend (2007), to estimate stress from geodetically constrained coseismic slip models, which has never been done before, and focal mechanisms. This dissertation aims to answer the following questions:

- Can a homogenous regional stress explain observed heterogeneity of fault slip during the M_w 7.9 Wenchuan, China, earthquake? Is heterogeneous slip along the Wenchuan rupture predominantly dictated by fault geometry?

- What are the ambiguities that arise in the interpretation of stress inferred from focal mechanisms? Can these ambiguities explain the variability in the Wenchuan aftershock slip mechanisms?

- What is the state of stress of the western North Anatolian fault in the Sea of Marmara, and is this stress consistent with the stress that generated the M_w 7.4 İzmit and M_w 7.2 Düzce, Turkey, earthquakes?

In addressing these questions, I particularly focus on the uncertainties in the estimation of stress. I incorporate uncertainties in the inferred coseismic slip rake in both coseismic slip models and focal mechanisms as well as uncertainties in the nodal plane geometries of focal mechanisms. The Bayesian method allows for the determination of the probability of a model being consistent with the given data and any initial information on the model. The models are the tensorial stresses, defined as the orientations of the principal stress and relative stress magnitudes, that produced

slip on a fault surface with a slip direction defined by a slip rake λ. Orientations of the stress tensor are defined through the Euler angles given by the trend and plunge of the MCS, ϕ_{MCS} and θ_{MCS}, respectively, and a rotation of the ICS and LCS about the MCS orientation, ρ_{MCS} (Figure 1.2). The magnitudes of the MCS, ICS, and LCS are defined to be σ_1, σ_2, and σ_3, respectively ($\sigma_1 \leq \sigma_2 \leq \sigma_3 \leq 0$ for compressive stresses). Relative stress magnitudes are defined as

$$\Delta = \frac{(\sigma_2 - \sigma_3)}{(\sigma_1 - \sigma_3)} \tag{1.1}$$

(e.g., Angelier, 1979; Etchecopar *et al.*, 1981), and

$$R_3 = \frac{\sigma_3}{\sigma_1}. \tag{1.2}$$

Δ defines the magnitude of the intermediate compressive stress (ICS) relative to the MCS and LCS. This is defined between 0 and 1, where $\Delta = 1$ indicates that the magnitudes of MCS and ICS are the same $\sigma_1 = \sigma_2$, and $\Delta = 0$ indicates $\sigma_2 = \sigma_3$. R_3 is defined between 0.21 to 1, where $R_3 = 1$ corresponds to an isotropic stress and the lower bound of $R_3 = 0.21$ avoids stress tensors with unreasonably high deviatoric stresses. $R_3 = 0.21$ corresponds to stresses in which a fault would fail at a coefficient of static friction, μ_f, of 0.85 along an optimally oriented plane.

The BMC method is first applied to geodetically constrained coseismic slip models of the 2008 M_w 7.9 Wenchuan, China, earthquake (Chapter 2). Slip in this earthquake transitioned from predominantly thrust on shallow dipping fault segments to right-lateral strike slip on steeply dipping fault segments. Results indicate that slip on all fault segments is consistent with a homogeneous state of stress irrespective of the chosen coseismic slip models. Models of stress that generated this earthquake are consistent with a subhorizontal MCS trending NW-SE, an ICS subhorizontal and trending nearly N-S, and a vertical LCS. I therefore conclude that fault geometry

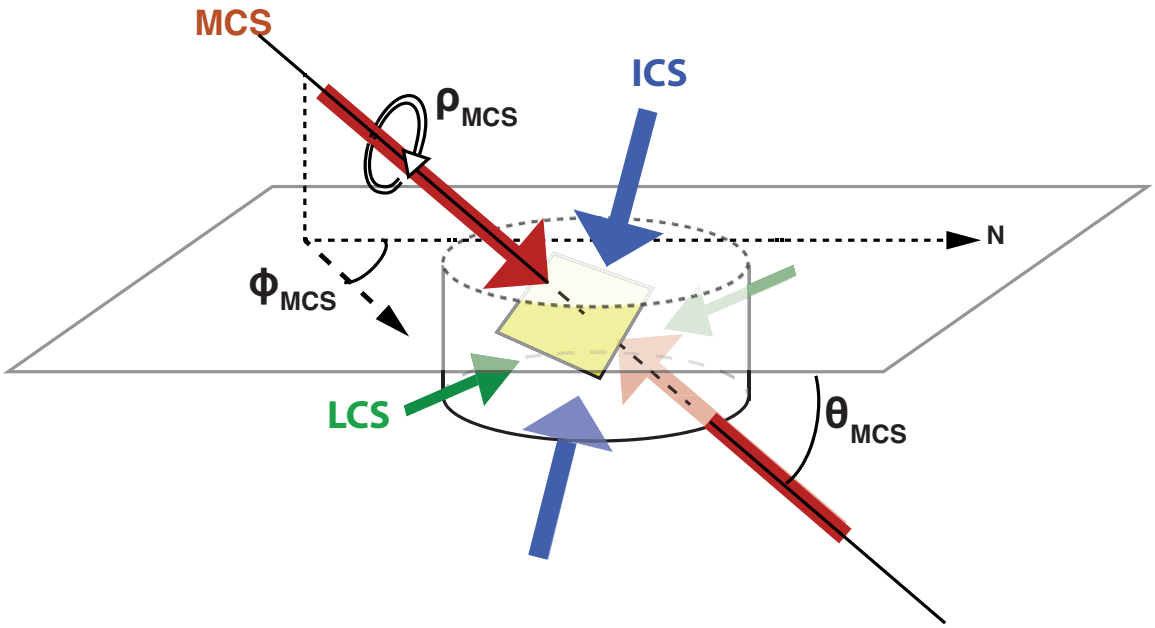

Figure 1.2: Illustration of principal stress orientations relative to a crustal body. MCS, ICS and LCS are the most, intermediate and least compressive stresses, respectively. Orientation of principal stress in terms of $\phi_{\mathrm{MCS}}, \theta_{\mathrm{MCS}}$, and ρ_{MCS}.

predominantly dictates the heterogeneous slip along the Wenchuan earthquake rupture. Since the coseismic slip is consistent with a homogenous state of stress, any heterogeneity in the stress that led to the earthquake must be slight. In contrast to the interpretation that a homogeneous stress led to the Wenchuan earthquake, Wang *et al.* (2009) and Cai *et al.* (2011) argued for a heterogenous stress inferred from focal mechanisms of the Wenchuan earthquake.

Aftershocks reflect stress changes due to an earthquake in addition to any pre-mainshock stresses present in the region. Therefore, the use of aftershocks alone may not reflect the stress prior to the mainshock. Additionally, stress inferences from focal mechanisms alone may indicate a potential for ambiguities in the interpretation of stress. In Chapter 3, I apply the BMC method to synthetic focal mechanisms where I clearly depict cases where ICS is mis-identified as either MCS or LCS. I then re-examine the stress inferences for the Wenchuan aftershocks, where fault planes may not be optimally oriented for failure and ambiguities in the stress interpretation

can explain the proposed stress heterogeneities along the Wenchuan rupture. Using aftershock focal mechanisms of Cai *et al.* (2011), I conclude that the heterogeneity of stress along the Longmenshan fault zone may simply be due to incorrect interpretation of principal stress orientations.

In Chapter 4, I turn my attention to the 1999 İzmit and Düzce earthquakes. The August 17, 1999, M_w 7.4 İzmit earthquake occurred along the western portion of the North Anatolian fault (NAF) and propagated east towards the city of Düzce where on November 12, 1999, the M_w 7.2 Düzce earthquake occurred. Predominantly right-lateral strike slip occurred on nearly vertical fault segments in the İzmit rupture (Reilinger *et al.*, 2000; King *et al.*, 2001; Barka *et al.*, 2002; Delouis *et al.*, 2002, Çakir *et al.*, 2003b), while predominantly right-lateral slip with a normal component of slip occurred on relatively shallow segments in the Düzce earthquake (Ayhan *et al.*, 2001; Bürgmann *et al.*, 2002; Çakir *et al.*, 2003a; Konca *et al.*, 2010). Results indicate a homogenous state of stress is statistically consistent with coseismic slip during the İzmit-Düzce earthquakes, with MCS subhorizontal and trending NW-SE, ICS nearly N-S, and LCS vertical.

Since one fault segment greatly deviates in fault strike, I investigate the Mohr-Coulomb failure conditions under which each fault segment slips. Results indicate that for the same state of stress, all segments slip with low frictional properties, and that failure along the deviating fault segment consistently requires lower friction than the surrounding faults to fail. Alternatively, all fault segments may have the same frictional properties; however, for slip to simultaneously occur on all fault segments, localized heterogeneous stresses need to be considered. Çakir *et al.*, (2003a) made no formal attempt to quantify the deviating fault segment in their coseismic slip model, therefore their model provides inferences of stresses leading to slip on all fault segments at higher frictional values.

West of the İzmit rupture the NAF extends through the Sea of Marmara as multiple fault segments, including the northern Main Marmara fault strand (MMF; Le Pichon *et al.*, 2001). To further investigate the stress on the MMF near Istanbul, we invert several focal mechanisms of M_w 1.4 to 4.5 earthquakes along the MMF both prior to and following the İzmit-Düzce earthquake sequence (Ergin *et al.*, 1997; Kiratzi, 2002; Pinar *et al.*, 2003; Bulut *et al.*, 2009; Örgülü 2011). Results indicate that offshore stresses along the MMF segments are rotated from the onshore stresses inferred from the İzmit and Düzce coseismic slip models. Rotation of stress from onshore to offshore may have played a role in the termination of slip in the İzmit rupture to the east. Furthermore, there is a suggestion that stress along the western portion of the MMF has rotated from an E-W trending MCS prior to the İzmit earthquake to a more NW-SE trending MCS after the İzmit earthquake. This rotation is such that the stress has become closer to a transform stress regime, capable of producing strike-slip on the Western fault, corroborating studies that indicate predominant transform slip on the MMF (Şengör *et al.*, 2005; Pinar *et al.*, 2010). No rotation is observed along the eastern segment of the MMF closer to the İzmit rupture between 1999 and 2003, I therefore do not attribute stress rotation on the Western Fault to coseismic stress changes of the İzmit earthquake.

Results from these studies answer the questions posed at the beginning of this section:

- A homogeneous regional stress is statistically consistent with patterns of heterogeneous slip along the Longmenshan fault zone, and fault geometry predominantly dictates the slip partitioning exhibited during the 2008 Wenchuan, China, earthquake (Chapter 2; Medina Luna and Hetland, 2013).

- Using focal mechanisms alone for a stress inversion may lead to ambiguities in the interpretation of stress between ICS and MCS or LCS, specifically when Δ is near 0 or 1, and when non-optimally oriented faults are considered (Chapter

3; Medina Luna and Hetland, in prep). Heterogeneities along the Wenchuan rupture previously proposed from aftershock focal mechanisms (Wang *et al.*, 2009; Cai *et al.*, 2011) can be explained by ambiguities in the interpretation of stress.

- A homogeneous state of stress is consistent with the coseismic slip inferred in the 1999 İzmit and Düzce earthquakes, particularly if all fault segments have a low coefficient of friction. Stress inferred from focal mechanisms of small earthquakes in the Sea of Marmara indicate stress partitioning along the western and eastern segments of the MMF, with stress differing from that inferred from the coseismic slip models to the east.

1.4 References

Anderson, E. M., 1951. The Dynamics of faulting and dyke formations with applications to Britain, 2nd Edition. Edinburgh: Oliver and Boyd. Print.

Angelier, J., (1979). Determination of the mean principal directions of stresses for a given fault population. Tectonophysics **56**, T17T26, doi: 10.1016/0040-1951(79)90081-7.

Arnold, R., and J. Townend, (2007). A Bayesian approach to estimating tectonic stress from seismological data. Geophys J. Int., **170**, 1336-1356. doi: 10.1111/j.1365-246X.2007.03485.x.

Ayhan, M. E., Bürgmann, R., McClusky, S., Lenk, O., Aktug, B., Herrece, E., and Reilinger, R. E., (2001). Kinematics of the Mw = 7.2, 12 November 1999, Düzce, Turkey Earthquake. Geophys. Res. Let., **28**, no. 2, p. 367-370.

Barka, A., Akyüz, H. S., Altunel, E., Sunal, G., Çakir, Z., Dikbas, A., Yerli, B., Armijo, R., Meyer, B., de Chabalier, J. B., Rockwell, T., Dolan, J. R., Hartleb, R., Dawson, T., Christoferson, S., Tucker, A., Fumal, T., Langridge, R., Stenner, H., Lettis, W., Bachhuber, J., and Page, W., (2002). The surface rupture and slip distribution of the 17 August 1999 İzmit earthquake (M7.4), North anatolian Fault. Bull. Seism. Soc. Am., **92**, no. 1, p. 43-60.

Bott, M. H. P., (1959). The mechanics of oblique slip faulting. Geological Magazine, **96**, Issue 2, 109-117. doi: 10.1017/S0016756800059987.

Bulut, F., Bohnhoff, M., Ellsworth, W. L., Aktar, M., and Dresen, G., (2009). Microseismicity at the North Anatolian Fault in the Sea of Marmara offshore Istanbul, NW Turkey. J. Geophys. Res., **114** B09302, doi: 10.1029/2008JB006244.

Bürgmann, R., Ayhan, M. E., Fielding, E. J., Wright, T. J., McClusky, S., Aktug, B., Demir, C., Lenk, O., and Türkezer, A., (2002). Deformation during the 12 November 1999 Düzce, Turkey, Earthquake from GPS and InSAR Data. Bull. Seism. Soc. Am., **91**, no. 1, p. 161-171.

Cai, C., Yu, C., Tao, K., Hu, X., Tian, Y., Zhang, H., Cui, X., Ning, J., (2011). Spatial distribution and focal mechanism solutions of the Wenchuan earthquake series: results and implications. Earthquake Science, **24**, 115125, doi: 10.1007/s11589-011-0775-5.

Çakir,Z., Barka, A. A., de Chabalier, J. B., Armijo, R., and Meyer, B., (2003a). Kinematics of the November 12, 1999 (Mw=7.2) Düzce earthquake deduced from SAR interferometry. Turkish J. Earth Sci., **12**, p. 105-118.

Çakir, Z., de Chabalier, J. B., Armijo, R., Meyer, B., Barka, A., and Peltzer, G., (2003b). Coseismic and early post-seismic slip associated with the 1999 Izmit earthquake (Turkey), from SAR interferometry and tectonic field observations. Geophys. J. Int., **155**, 93-110, doi: 10.1046/j.1365-246X.2003.02001.x.

Çakir,Z., Ergintav, S., Özener, H., Dogan, U., Akoglu, A. M., Meghraoui, M., and Reilinger, R., (2012). Onset of aseismic creep on major strike-slip faults. Geology, **40**, no. 12, p. 1115-1118, doi: 10.1130/G33522.1.

Célérier, B., (1988). How much does slip on a reactivated fault plane constrain the stress tensor? Tectonics, **7**, no. 6, 1257-1278.

Delouis, B., Giardini, D., Lundgren, and P., Salichon, J., (2002). Joint Inversion of InSAR, GPS, Teleseismic, and Strong-Motion data for the spatial and temporal distribution of earthquake slip: Application to the 1999 Izmit mainshock. Bull. Seism. Soc. Am., **92**, no. 1, 278-299, doi: 10.1785/0120000806.

Engelder, T., (1993). Stress Regimes in the Lithosphere. Princeton University Press: Princeton, New Jersey. Print.

Etchecopar, A., Vasseur, G., and Daignieres, M., (1981). An inverse problem in micro tectonics for the determination of stress tensors from fault striation analysis. J. Structural Geology, **3**, no. 1, 51-65.

Feng, G., Hetland, E., Ding, X., Li, Z., and Zhang, L., (2010). Coseismic fault slip of the 2008 Mw 7.9 Wenchuan earthquake estimated from InSAR and GPS

measurements. J. Geophys. Res., **37**, L01302, doi:10.1029/2009GL041213.

Gephart, J. and Forsyth, D., (1984). An improved method for determining the regional stress tensor using earthquake focal mechanism data: Application to the San Fernando earthquake sequence. J. Geophys. Res., **89**, 9305-9320, doi: 10.1029/JB089iB11p09305.

Hardebeck, J. L., and Michael, A. J., (2006). Damped regional-scale stress inversions: Methodology and examples for southern California and the Coalinga aftershock sequence. J. Geophys. Res., **111**, B11310, doi:10.1029/2005JB004144.

Hauksson, E., (1994). State of stress from focal mechanisms before and after the 1992 Landers earthquake sequence. Bull. Seism. Soc. Am., **84**, No. 3, 917-734.

Jaeger, J. C. and Cook, N. G. W., (1979). Fundamentals of rock mechanisms, third edition. London: Chapman and Hall. Print.

Kanamori, H. and Brodsky, E., (2004). The physics of earthquakes. Rep. Prog. Phys., **67**, p. 1429-1496.

King, G. C. P., Hubert-Ferrari, A., Nalbant, S. S., Meyer, B., Armijo, R., and Bowman, D., (2001). Coulomb interactions and the 17 August 1999 Izmit, Turkey earthquake. Earth Planet. Sci., **333**, p. 557-569.

Konca, O., Leprince, S., Avouac, J. P., and Helmberger, (2010). Rupture process of the 1999 M_w 7.1 Duzce earthquake from joint analysis of SPOT, GPS, InSAR, Strong-Motion, and Teleseismic data: A supershear rupture with variable rupture velocity. Bull. Seism. Soc. Am., **100**, no. 1, p. 267-288, doi: 10.1785/0120090072.

Le Pichon, X., Şengör, A.M.C., Demirbağ, Rangin, C., İmren C., Armijo, R., Görür, N., Çağatay, N., Mercier de Lepinay, B., Meyer, B., Saatçliar, R., and Tok, B., (2001). The active Main Marmara fault. Earth Planet. Sci. Lett., **192**, p. 595-616

LePichon, X., Chamot-Rooke, N., and Rangin, C., (2003). The North Anatolian

fault in the Sea of Marmara. J. Geophys. Res., **108**, no. B4, 2179, doi: 10.1029/2002JB001862.

McGarr, A., and Gay, N. C., (1978). State of stress in the Earth's crust. Ann. Rev. Earth Planet. Sci., **6**, 705-36.

McKenzie, D. P., (1969). The relation between fault plane solutions for earthquakes and the directions of the principal stresses. Bull. Seism. Soc. Am., **59**, No. 2, 591-601.

Meade, B. J., and Hager, B. H., (2005). Spatial localization of moment deficits in southern California. J. Geophys. Res. **110**, B04402, doi: 10.1029/2004JB003331.

Medina Luna, L., and Hetland, E. A., (2013). Regional stresses inferred from co-seismic slip models of the 2008 Mw 7.9 Wenchuan, China, earthquake. Tectonophysics, **584**, 43-53, doi: 10.1016/j.tecto.2012.03.027.

Michael, A. J., (1984). Determination of stress from slip data: faults and folds. J. Geophys. Res., **89**, B13, 11,517-11,526, doi: 10.1029/JB089iB13p11517.

Michael, A. J., (1987). Use of focal mechanisms to determine stress: a control study. J. Geophys. Res., **92**, B1, 357-368. doi: 10.1029/JB092iB01p00357.

Pinar, A., Honkura, Y., and Kuge, K., (2001). Seismic activity triggered by the 1999 Izmit earthquake and its implications for the assessment of future seismic risk. Geophys. J. Int., **146**, p. F1-F7.

Pinar, A., Kuge, K., Honkura, Y., (2003). Moment tensor inversion of recent small to moderate sized earthquakes: implications for seismic hazard and active tectonics beneath the Sea of Marmara. Jeophys. J. Int., **153**, No. 1, 133-145, doi: 10.1046/j.1365-246X.2003.01897.x.

Pinar, A., Üçer, S. B., Honkura, Y., Sezgin, N., Ito, A., Bariş, Ş, Kalafat, D., Matsushima, M., and Horiuchi, S., (2010). Spatial variation of the stress field along the fault rupture zone of the 1999 Izmit earthquake. Earth Planets Space, **62**, p. 237-256.

Reilinger, R. E., Ergintav, S., Bürgmann, R., McClusky, S., Lenk, O., Barka, A., Gurkan, O., Hearn, L., Feigl, K. L., Cakmak, R., Aktug, B., Ozener, H., andÇakir Toksoz, M. N., (2000). Coseismic and Postseismic Fault Slip for the 17 August 1999, M = 7.5, Izmit, Turkey Earthquake. Science, **289**, 1519-1524, doi: 10.1126/science.289.5484.1519.

Schleicher, A. M., van der Pluijm, B. A., and Warr, L. N., (2010). Nano-coatings of clay and creep of the San Andreas Fault at Parkfield, California. Geology, **38**, p. 667-670, doi:10.1130/G31091.1.

Şengör, A.M.C., Tüysüz, O., İmren, C., Sakinç, M., Eyidoğan, H., Görür, N., Le Pichon, X., and Rangin, C., 2005. The North Anatolian Fault: A New Look. Annu. Rev. Earth Planet. Sci., **33**, 37-112, doi: 10.1146/annurev.earth.32.101802.120415.

Tong, X., Sandwell, D., and Fialko, Y., (2010). Coseismic slip model of the 2008 Wenchuan earthquake derived from joint inversion of interferometric synthetic aperture radar, GPS, and field data. J. Geophys. Res., **115**, B04314, doi: 10.1029/2009JB006625.

Wang., Q. C., Chen, Z. L., and Zheng, S. H., (2009). Spatial segmentation characteristic of focal mechanism of aftershock sequence of Wenchuan Earthquake. Chinese Sci. Bull., **54**, 2263-2270, doi: 10.1007/s11434-009-0367-0.

Weldon, R., Scharer, K., Fumal, T., and Biasi, G., (2004). Wrightwood and the earthquake cycle: What a long recurrence record tells us about how faults work. GSA Today, **14**, no. 9, p. 4-10, doi: 10.1130/1052-5173.

Zhang, G., Qu, C., Shan, X., Song, X., Zhang, G., Wang, C., Hu, J.C., and Wang, R., (2011). Slip distribution of the 2008 Wenchuan Ms 7.9 earthquake by joint inversion from GPS and InSAR measurements: A resolution test study. Geophys. J. Int. **186**, 207220, doi: 10.1111/j,1365 246X.2011.05039.x.

Zoback, M. L., and Zoback, M., (1980). State of stress in the conterminous United States. J. Geophys. Res., **85**, No. B11, 6113-6156.

CHAPTER 2

Regional Stresses Inferred from Coseismic Slip Models of the 2008 Mw 7.9 Wenchuan, China, Earthquake

2.1 Abstract

The 12 May 2008, Mw 7.9 Wenchuan earthquake occurred on the Beichuan fault in the southwest to northeast trending Longmenshan fault zone (LMSfz), marking the border of the Sichuan basin and eastern Tibet. During the Wenchuan earthquake, the Beichuan fault slipped primarily in thrust motion on moderately dipping fault segments in the southwest, and as largely right lateral strike slip motion on more steeply dipping segments in the northeast. Additionally, the shallowly dipping Pengguan fault, located to the east of the Beichuan fault, slipped as mostly thrust slip. In this study, we explore the connection between sense of slip and fault geometry, and investigate whether models of coseismic slip yield information about the pre-earthquake background stress in the region of the Wenchuan earthquake. Specifically, we test

This chapter was published as: Medina Luna, L., and Hetland, E. A., (2013). Regional stresses inferred from coseismic slip models of the 2008 Mw 7.9 Wenchuan, China, earthquake. Tectonophysics, **584**, 43-53, doi: 10.1016/j.tecto.2012.03.027.

whether coseismic slip models are consistent with a homogeneous regional stress, or if a heterogeneous stress field is required to explain the change in slip rake along strike. We assume that coseismic slip is parallel to the direction of the maximum shear stress on the fault, and consider several published coseismic slip models with differing fault geometries. Using a Bayesian probabilistic estimation, we find that the coseismic slip of the Wenchuan earthquake is consistent with a constant orientation of principal stresses along the strike of the LMSfz. This suggests a homogeneous state of stress prior to the earthquake, although our analysis only provides weak constraints on the relative magnitudes of the principal stresses. The inferred most compressive stress direction is sub-horizontal and approximately east-west trending. The intermediate compressive stress is sub-horizontal and north-south trending, and is most likely about 30% the magnitude of the most compressive stress. The least compressive stress is near-vertical.

2.2 Introduction

As the first recorded large earthquake in the Longmenshan fault zone (LMSfz), the Mw 7.9 Wenchuan earthquake of 12 May 2008 provides an opportunity to investigate the stresses in the Longmenshan region, thereby gaining insight into the present day tectonics of this region. The SW-NE striking LMSfz marks the transition between the 4-5 km high Tibetan Plateau and the roughly 500 m high Sichuan Basin (Fig. 2.1; *e.g.*, *Chen and Wilson*, 1996; *Burchfiel et al.*, 2008). About 500 km long and 30-50 km wide, the Longmenshan are characterized by steep topographic relief in the central region, which decreases to a lower relief towards the north-east (*Chen and Wilson*, 1996; *Zhang et al.*, 2011b). Two end-member models have been proposed to explain the deformation within the LMSfz. The first is that crustal shortening, in which the upper and lower crust are decoupled by detachment faults, is solely responsible for the uplift of the Longmenshan (*Hubbard and Shaw*, 2009). *Chen and Wilson* (1996)

similarly concluded that the LMSfz was due to upper crustal shortening adjacent to the Sichuan basin, but also argued that the higher topography Longmenshan was more consistent with "thick-skinned" tectonics. The latter is consistent with the model of the evolution of the Tibetan plateau proposed by *Tapponier et al.* (2001). The second model to explain the deformation of the LMSfz is that general eastward flow of the lower crust, driven by the elevated central Tibetan plateau, is inhibited by the rigid Sichuan Basin, resulting in the sharp topographic gradients of the Longmenshan (*Clark and Royden*, 2000; *Clark et al.*, 2005; *Royden et al.*, 2008).

The Wenchuan earthquake initiated on the Yingxiu-Beichuan-Qingchuan fault, and propagated to the NE along this N32°E trending, NW dipping fault (Fig. 2.1; *e.g.*, *Burchfiel et al.*, 2008; *Liu et al.*, 2009; *Lin et al.*, 2009; *Xu et al.*, 2009). We refer to the section of the fault that ruptured simply as the Beichuan fault, of which almost 300 km slipped during the earthquake (*e.g.*, *Liu et al.*, 2009; *Lin et al.*, 2009; *Shen et al.*, 2009; *Xu et al.*, 2009). A smaller segment ($\sim$70 km) of the parallel Pengguan fault (also referred to as the Guanxian-Anxian fault), to the SE of the Beichuan fault, also slipped during the Wenchuan earthquake (Fig. 2.1a; *e.g.*, *Kobayashi et al.*, 2009; *Liu et al.*, 2009; *Lin et al.*, 2009; *Xu et al.*, 2009). Coseismic fault scarps, as well as seismologically and geodetically constrained coseismic slip models, reveal a complicated pattern of slip, with both thrust and strike slip offsets. The largest coseismic slip in the Wenchuan earthquake is in the rather shallow crust, and there does not appear to be a significant near-surface coseismic slip deficit, as is commonly observed in continental earthquakes (*Fialko et al.*, 2005; *Tong et al.*, 2010). Although there are slight differences in the details of the coseismic slip models, the emerging consensus is that the Wenchuan earthquake was dominated by thrust slip on moderately dipping fault segments closer to the SW end of the Beichuan fault, with more right-lateral slip on more steeply dipping fault segments in the NE (*Kobayashi et al.*, 2009; *Liu et al.*, 2009; *Lin et al.*, 2009; *Xu et al.*, 2009; *Shen et al.*, 2009; *Hashimoto et al.*, 2010; *Feng*

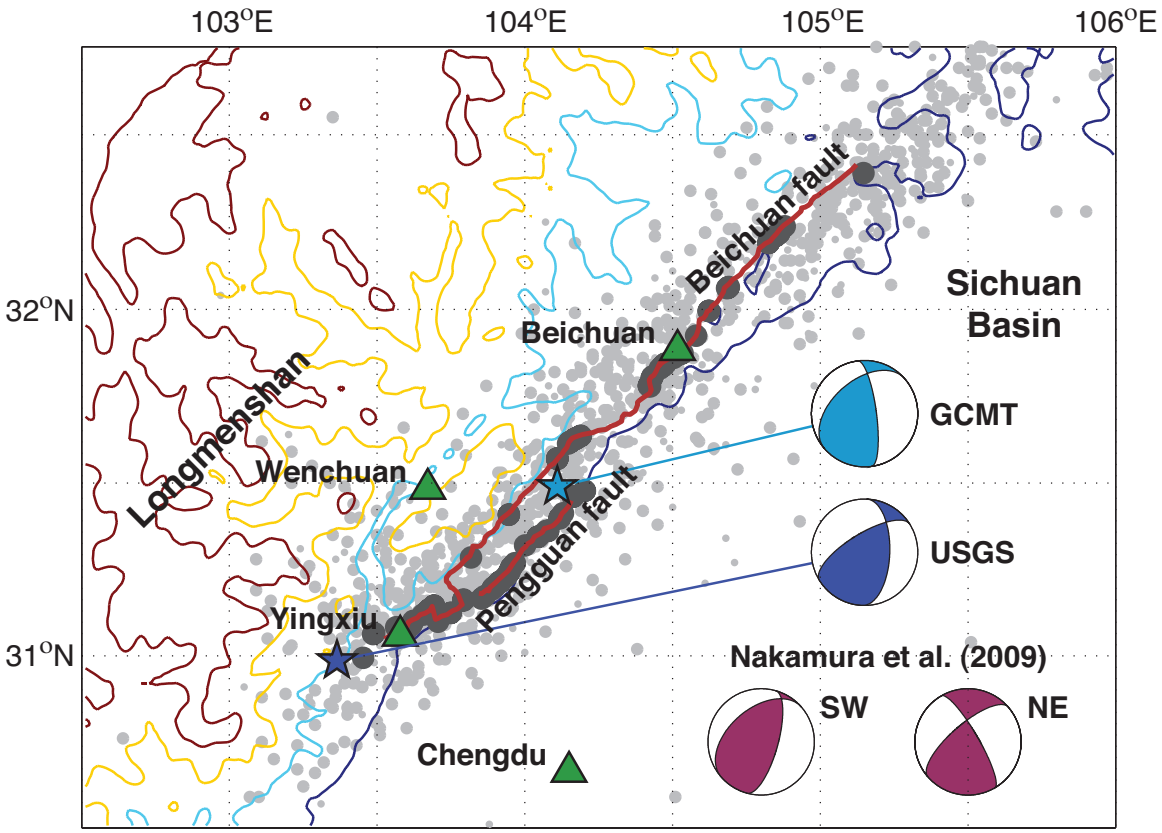

Figure 2.1: Map of the Longmenshan fault zone region. Dark blue, cyan, yellow, and dark red lines depict the 1, 2, 3, and 4 km elevation contours, respectively. The surface rupture of the Beichuan fault, determined from InSAR pixel tracking offsets by *Feng et al.* (2010), is shown as red lines, and locations where surface ruptures were mapped by *Liu et al.* (2009), *Lin et al.* (2009) and *Xu et al.* (2010) are shown as large dark gray circles. Also shown are location of aftershocks in the year following the mainshock (light grey dots), prominent cities (green triangles), the global CMT (GCMT) centroid location (blue star) and focal mechanism, the USGS centroid location (cyan star) and focal mechanism, and the focal mechanisms of the two fault solution of *Nakamura et al.* (2010).

et al., 2010; *Tong et al.*, 2010; *Zhang et al.*, 2011a). In addition to the slip along the Beichuan fault, the more shallowly dipping Pengguan fault ruptured almost entirely as thrust slip (*Kobayashi et al.*, 2009; *Liu et al.*, 2009; *Lin et al.*, 2009; *Shen et al.*, 2009; *Xu et al.*, 2009). Aftershocks and mapped fault scarps also indicate that the dip of the Beichuan fault increases to the NE (*e.g.*, *Huang et al.*, 2008; *Liu et al.*, 2009; *Lin et al.*, 2009; *Wang et al.*, 2009; *Xu et al.*, 2009). *Nakamura et al.* (2010)

noted that the synthetic waveforms generated from the Global CMT focal mechanism solution, consisting of a single shallowly dipping nodal plane taken to be the primary fault plane, are not a good fit to the the observed seismograms. Rather, *Nakamura et al.* (2010) found that a two segment fault model, with the fault dip increasing on the NE segment (Fig. 2.1), provided a better prediction of the observed seismograms. Based on geodetically and seismologically constrained coseismic slip models, there appears to be a strong correlation between the slip rake and fault dip, with moderately dipping fault segments rupturing in largely thrust slip at the SW end, and more steeply dipping fault segments rupturing in largely right-lateral slip at the NE end.

The Longmenshan is likely indicative of cumulative offsets from earthquakes (*e.g.*, *Burchfiel et al.*, 2008), although this region has been surprisingly devoid of earthquakes prior to the 2008 Wenchuan earthquake. Estimates of the rate of thrust and strike slip strain accumulation on the LMSfz vary markedly. *Chen and Wilson* (1996) noted that slickensides on the Beichuan fault were consistent with NW-SE trending shortening across the LMSfz. In contrast, based on paleoseimologic field investigations along the Beichuan and Pengguan faults, *Densmore et al.* (2007) inferred a thrust slip rate of less than 1 mm/yr, with strike slip rates of up to 10 mm/yr over the Quaternary. Based on GPS measurements and an elastic block model, *Meade* (2007) inferred that strain was accumulating in the LMSfz region with a ratio of thrust to strike slip of 2:3. Using a similar analysis, *Thatcher* (2007) concluded that strain was not accumulating on the LMSfz at a rate discernible with the GPS data, but found that a pure right-lateral fault was required about 100 km west of the LMSfz. Following the Wenchuan earthquake, *Burchfiel et al.* (2008) constructed a new pre-earthquake interseismic model concluding that the accumulation rate of thrust slip on the LMSfz in the region of the Wenchuan rupture increased by a factor of three from SW to NE. *Shen et al.* (2009) also re-interpreted the pre-earthquake interseismic GPS observations to infer a thrust to strike slip accumulation ratio of about 1:2

on the Beichuan fault, with only thrust slip accumulating on the Pengguan fault. The most recent geodetic-based strain accumulation rates estimated by *Loveless and Meade* (2011) find almost a 1:1 ratio of thrust to strike slip accumulation across the LMSfz.

The apparent correlation between the sense of coseismic slip and the dip of the ruptured fault segments may be indicative of the tectonic stresses in the LMSfz region (*e.g.*, *Xu et al.*, 2008; *Feng et al.*, 2010; *Nakamura et al.*, 2010; *Cai et al.*, 2011). The change in rake of coseismic slip along the Beichuan fault may simply reflect that the LMSfz is being loaded largely in thrust in the SW and largely in strike-slip in the NE. Since there is not a large variation of the strike of the LMSfz along the Wenchuan rupture (Fig. 2.1), this change in fault loading along the 300 km long rupture would indicate a heterogeneous pre-earthquake stress. This may be reasonable, as the GPS resolved motion of the Tibetan plateau with respect to the Sichuan basin is in a more northerly direction to the north of the Sichuan basin, compared to a more easterly motion to the west of the basin (*Zhang et al.*, 2004; *Royden et al.*, 2008). That the fault segments that ruptured on the NE end of the Beichuan fault during the Wenchuan earthquake appear to be more steeply dipping, may be a result of simple Andersonian theory of faulting (*Anderson*, 1951). For instance, *Nakamura et al.* (2010) do not find evidence in the Global CMT catalogue of large strike-slip earthquakes on shallowly dipping faults. Geomorphic evidence also suggests a strong variation in elevation along the strike of the LMSfz (*Zhang et al.*, 2011b). This may be consistent with the view that the stresses loading the LMSfz in the SW result in more thrust earthquakes, leading to larger topography, whereas stresses consistent with primarily strike-slip earthquakes in the NE result in lower topographic relief. The alternative hypothesis is that a homogeneous pre-earthquake stress is consistent with the change in coseismic slip rake along strike of the Wenchuan rupture, with existing fault dip determining the style of faulting.

In this paper, we test whether a homogeneous pre-earthquake stress field is consistent with the sense of coseismic slip in the Wenchuan earthquake, or whether a heterogeneous stress field needs to be appealed to. We consider three geodetically constrained coseismic slip models (*Feng et al.*, 2010; *Tong et al.*, 2010; *Zhang et al.*, 2011a). Each of these models are based on essentially the same geodetic observations, but assume different fault geometries, and utilize a different inversion strategy in order to estimate the coseismic slip. We do not consider frictional stability of the faults, rather we assume that once the fault fails, the resulting static coseismic slip on each of the fault segments will be in the direction of the maximum pre-earthquake shear stress (*e.g.*, *Angelier*, 1979; *Gephart and Forsyth*, 1984). The pre-earthquake shear stress reflects the cumulative stress accumulated during the interseismic period, and we note that we do not quantify the magnitudes of the accumulated shear stress nor the coseismic stress drop during the Wenchuan earthquake. Our analysis follows that of *Angelier* (1979) who used slickensides to constrain the directions of principal stresses, while here we use geodetically constrained models of coseismic fault slip at depth. Using a probabilistic Bayesian inversion procedure, we find that coseismic slip models of the Wenchuan earthquake can be explained remarkably well by a pre-earthquake stress field in which the orientation of the three principal stress directions do not vary along strike of the LMSfz. That the stress orientations do not vary suggests a homogeneous pre-earthquake stress field, although our results do not fully constrain the magnitudes of the principal stresses. We find that the most compressive stress is near horizontal and oriented roughly east-west, and that the intermediate compressive stress is roughly north-south trending and also sub-horizontal. We find that the magnitude of the intermediary compressive stress is about 30% the magnitude of the most compressive stress. An understanding of the pre-earthquake stresses in this LMSfz region can be used as a constraint on geodynamic models of deformation and interseismic strain accumulation at the eastern edge of the Tibetan plateau.

Moreover, knowing the pre-earthquake stress field may yield insight into the future earthquake hazards facing this region.

2.3 Coseismic Slip Models

We consider three published geodetically constrained coseismic slip models, those of *Feng et al.* (2010), *Tong et al.* (2010), and *Zhang et al.* (2011a), referred to as F10, T10, and Z11, respectively. Several more coseismic slip models have been published (*e.g.*, *Zhang et al.*, 2008; *Hao et al.*, 2009; *Shen et al.*, 2009; *Hashimoto et al.*, 2010; *Nakamura et al.*, 2010; *Wang et al.*, 2010), most of which are consistent in their large scale features. Each of the three considered coseismic slip models are constrained by both interferometric synthetic aperture radar (InSAR) and GPS measurements, but use different fault geometries and inversion strategies. These coseismic models approximate the fault geometry using four or five planar fault segments, with strike of the fault segments determined from InSAR pixel offsets and mapped surface ruptures, and fault dip on each of the segments constant with depth. F10 assumed the dip of the fault segments *a priori*, based largely on field scarps and aftershock hypocenters. Both T10 and Z11 varied the dip of each of their fault segments, selecting the fault dips that minimized the data misfit. We do not describe or compare the details of these coseismic slip models here, rather we limit our description of the models to those features which are important for our analysis.

The model of F10 consists of four fault segments, three of which compose the Beichuan fault and one that composes the Pengguan fault (Table 2.1). The InSAR catalogue used by F10 differs slightly from those used by T10 and Z11, in that F10 did not use radar acquisitions strongly affected by ionospheric anomalies that occurred during a several week interval bracketing the Wenchuan earthquake (*Zhao et al.*, 2008; *Yu et al.*, 2009; *Zhou et al.*, 2009; *Feng*, 2011). F10 imposed constraints that coseismic slip was composed of thrust to right-lateral slip on the Beichuan fault segments, and

purely thrust slip on the Pengguan fault. The latter constraint was imposed because differentiation of right-lateral coseismic slip on the two closely spaced faults was difficult due to the lack of near-field geodetic data (*Feng et al.*, 2010). Additionally, mapped surface offsets are consistent with predominantly thrust slip on the Pengguan fault (*Liu et al.*, 2009; *Lin et al.*, 2009; *Xu et al.*, 2009). F10 found that the ratio of thrust to strike slip coseismic offset was about 3:2 in the SW and 2:3 in the NE.

		Pengguan	Beichuan segments (SW-NE)			
F10	ϕ (°)	133	134	133	144	
	θ (°)	35	47	67	67	
	λ (°)	-180.0 ± 15.0	-155.2 ± 16.7	-132.6 ± 18.9	-122.6 ± 15.0	
	MLE λ (°)	-160.4	-149.1	-126.2	-131.3	
T10	ϕ (°)	137	128	137	128	
	θ (°)	25	35	50	70	
	λ (°)	-165.8 ± 19.6	-155.6 ± 11.3	-140.9 ± 10.1	-120.3 ± 16.9	
	MLE λ (°)	-170.3	-162.3	-146.6	-120.3	
Z11c	ϕ (°)	138	138	115	138	130
	θ (°)	33	47	60	70	80
	λ (°)	-166.7 ± 12.1	-150.0 ± 14.5	-142.6 ± 15.5	-121.2 ± 12.0	-110.0 ± 11.8
	MLE λ (°)	-161.5	-149.5	-144.5	-123.8	-104.2
Z11f	ϕ (°)	138	138	115	138	130
	θ (°)	33	47	60	70	80
	λ (°)	-99.5 ± 146.7	-141.3 ± 15.9	-139.1 ± 21.9	-120.4 ± 13.0	-109.1 ± 9.1

Table 2.1: Fault segment strike, ϕ (counterclockwise from East), dip, θ (NE dip from horizontal), and coseismic slip rake, λ, for each of the fault segments representing the Pengguan and Beichuan faults in the coseismic models of *Feng et al.* (2010; F10), *Tong et al.* (2010; T10), or *Zhang et al.* (2011a; Z11c and Z11f are the rake constrained and unconstrained estimations). Coseismic rake is given as the weighted average ± one standard deviation of the slip rake on the fault segments in the coseismic models; only the upper 15 km of the models was considered in F10 and Z11. Also listed is the slip rake predicted by the most likely estimate (MLE) of the homogeneous stress determined jointly from the coseismic models of F10, T10, and Z11c.

T10 approximated the Beichuan fault into a northern, central and southern segment, with a single segment for the Pengguan fault (Table 2.1). The number of fault segments in the T10 model are the same as that in the F10 model, although the end-points of the fault segments are not the same in the two models. The dip of each of the fault segments in T10 was determined through a grid search, where the fault

dips were chosen as those resulting in the smallest data misfit in the least-squares solution of the coseismic slip model. Fault dip in the south is shallow at 35° and is steeper in the north with a dip of 70°, with all segments extending to 25 km depth (*Tong et al.*, 2010). T10 constrained fault slip to have only thrust or right-lateral components. In contrast to the coseismic model of F10, T10 used a model resolution based fault discretization.

Z11 approximated the Beichuan fault using four fault segments, with one segment approximating the Pengguan fault (Table 2.1). As in T10, Z11 determined the optimum dips of the fault segments through a grid search over dip. Z11 also considered several fault discretizations and rake constraints. All of their resulting models were largely consistent, with the exception of a coseismic slip model in which they relaxed the constraints on coseismic slip rake. Here we only consider two of their coseismic slip models, both with uniform fault discretization. We mainly focus on their model in which coseismic slip rake is constrained to be thrust slip to right-lateral strike slip, but we also consider their model in which there are no constraints imposed on the sense of coseismic slip. As expected, inferred coseismic slip has a much higher variability in rake in the model with no constraints on rake (Table 2.1, Z11f), with inference of significant normal and left-lateral fault slip in several places, opposite to what would be expected in this oblique-thrust earthquake. Most of the regions of slip opposite to the general trend are below about 15 km depth, leading Z11 to conclude that resolution of coseismic slip below this depth was poor. Considering only the slip in the upper 15 km in the models of Z11, the weighted average and standard deviation of estimated coseismic slip rake on each of the Beichuan fault segments is comparable in the slip models estimated with or without constraints on slip rake (Table 2.1). However, the variability of estimated coseismic slip on the Pengguan fault is much larger in the unconstrained model, indicating the high degree of model noise in the inversion when rake constraints are not imposed (Zhang et al., 2011a).

We only consider the non-rake-constrained model in order to test whether our model results are biased by using coseismic slip models in which the inferred coseismic slip rake is constrained.

In each of the coseismic slip models, slip rake (*i.e.*, the direction of coseismic fault slip) varies on each of the planar fault segments. It is important to note that the fault geometries in these coseismic slip models are approximations of more complex fault geometries. We compute the weighted average and variation of coseismic slip rake on each of the planar fault segments in each of the three models. The average slip rake is computed as the mean rake in all of the fault patches that discretize each segment, weighted by the magnitude of the slip so that fault patches with negligible inferred slip have little effect on the estimate of the average slip rake (Table 2.1). We calculate the variability of the slip rake on each segment as the square root of the weighted variation (*i.e.*, the weighted standard deviation). Whether we use a weighted or unweighted standard deviation results in a similar estimate of variability, and we use the weighted standard deviation to be consistent with our use of a weighted mean. In the models of F10 and Z11, the fault segments are approximated by uniform discretization down to about 30 km. As the geodetic data for the Wenchuan earthquake have little constraints on the inferred slip at depths below about 15 km (*Tong et al.*, 2010; *Zhang et al.*, 2011a), we only consider the inferred slip above 15 km in F10 and Z11. If we include the slip below 15 km in our analysis, there is a slightly larger variability in the slip rake on each segment, and as a result there is a slightly larger range of permissible stress directions, as discussed below. The model of T10 used a model-resolution based discretization, with large fault patches at depth where resolution is poor. In the case of T10, we use the entire coseismic model, as the model resolution is accounted for in the fault discretization. Coseismic slip on the fault segment approximating the Pengguan fault in the model of F10 is constrained to be pure thrust, and thus the variation of rake is zero. This lack of variability is purely a result of modeling choices

made by F10, and to avoid biasing our results based on their restrictive *a priori* constraint, we arbitrarily assign a standard deviation of 15° for the Pengguan fault segment in the F10 model. Likewise, the standard deviation of slip rake is slightly below 15° on the north-easternmost segment of the Beichuan fault in the F10 model, and we arbitrarily assign a standard deviation of 15° for this fault segment.

2.4 Stress Model and Estimation Methods

In this paper we test whether a homogeneous pre-earthquake stress field is consistent with the above coseismic slip models. We construct a relationship between a homogeneous pre-earthquake stress field and the expected direction of coseismic slip by assuming that each fault segment slips, on average, in the direction of the maximum shear stress on those fault segments. The assumption that slip and stress are co-linear, which is to say that a fault will slip in the direction of the maximum shear stress, is common in mechanical models of fault slip (*e.g.*, *Angelier*, 1979; *Gephart and Forsyth*, 1984; *Barbot et al.*, 2009; *Hetland et al.*, 2010). Furthermore, we assume that the stress on the fault is the same as in the immediate region, which is to say that we assume that the shear stresses on the Beichuan and Pengguan faults are due to the regional stresses along these faults.

2.4.1 Relationship between stress and coseismic slip

We describe a homogeneous stress tensor using the principal stress magnitudes and the angles describing the principal stress directions (Fig. 2.2a). Compressive stresses are assumed to be negative, and we refer to the most, intermediate, and least compressive stresses as MCS, ICS, and LCS, respectively. We denote the strike and dip of the principal stress directions as ϕ_{X} and θ_{X}, respectively, where X is either MCS, ICS, or LCS. The reference frame we use to describe the stress orientation is one in which an east-west aligned stress direction has a zero degree strike, with

$\phi_X = 90°$ referencing a north-south trending stress direction. We take $\theta_X = 0$ to be a horizontal stress direction. Note that due to the symmetry of stresses, a principal stress direction with orientation ϕ_X and θ_X can be described by $\phi_X \pm 180°$ and $-\theta_X$.

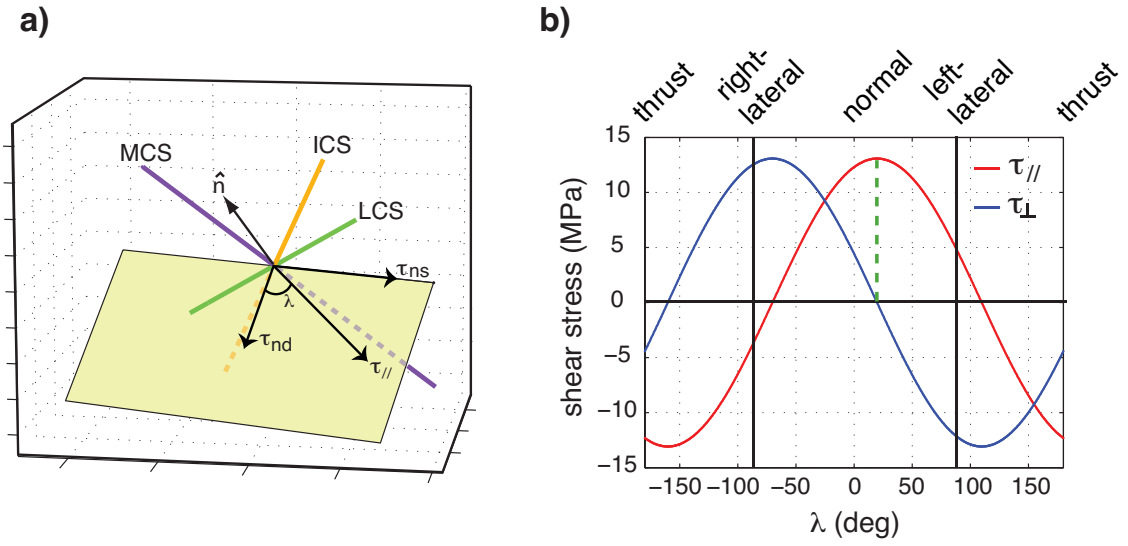

Figure 2.2: a) Illustration of a planar fault segment and principal stress directions: MCS (purple), ICS (orange), and LCS (green) are the most, intermediate, and least compressive stresses, respectively. Also show are fault normal, $\hat{n}$, fault rake, λ, and shear stresses on the fault plane (arrows indicate the shear stress acting on the upper side of the fault plane, τ_{nd}, τ_{ns}, and $\tau_{\|}$ are shear stresses in the dip, strike, and rake direction, respectively). b) Variation of shear stress on the fault parallel, $\tau_{\|}$, and perpendicular, $\tau_{\perp}$, with fault rake, λ, for the fault plane and stress shown in (a). The rake at which $\tau_{\|}$ is maximum and $\tau_{\perp} = 0$ is depicted by vertical green dashed line. $\lambda = \pm 180$, -90, 0, and 90 corresponds to pure thrust, right-lateral, normal, and left-lateral fault rake, respectively.

We determine the shear stresses on each planar fault segment by rotating a given stress tensor onto the plane (Fig. 2.2a). The strike and dip of each of the fault segments are taken from the three considered coseismic slip models (Table 2.1). We find the direction of maximum shear stress on the fault segment by further rotating the stress tensor about the normal of the planar segment (Fig. 2.2). As stated above, we assume that the coseismic slip on each fault segment is in the direction of the maximum shear stress on the fault segment (*Angelier*, 1979; *Gephart and Forsyth*, 1984), which we describe by the coseismic slip rake, λ. We adopt a notation such

that $\lambda = 0^\circ$ or $\pm 180^\circ$ is pure normal or thrust slip, respectively, and $\lambda = -90^\circ$ or 90° is pure right- or left-lateral strike slip, respectively (Fig. 2.2b). We do not focus on issues of frictional stability in this paper, and thus we do not use the magnitude of the shear stress or the inferred stress drop during the earthquake as constraints on plausible pre-earthquake stresses. By definition, the shear stress on a fault segment in a direction perpendicular to the direction of maximum shear stress is zero (Fig. 2.2b). The direction of the maximum shear stress on a fault segment is not sensitive to the absolute magnitudes of the principal stresses, but only to the relative magnitudes of the stresses (*e.g.*, *Sibson*, 1985). Due to this fact and the symmetries of the stress tensor, in our estimation we parameterize the stress tensor using the relative magnitudes of the principal stresses ($\sigma_{\mathrm{ICS}}/\sigma_{\mathrm{MCS}}$ and $\sigma_{\mathrm{LCS}}/\sigma_{\mathrm{ICS}}$), ϕ_{MCS}, θ_{MCS}, and a rotation of the ICS and LCS directions about the MCS direction, ρ_{MCS}. Finally, we reiterate that our analysis is as proposed by *Angelier* (1979) although we use estimates of coseismic slip as constraints on stress directions, whereas *Angelier* (1979) used slickensides.

2.4.2 Estimation strategy

We adopt a Monte Carlo, Bayesian estimation strategy to find homogeneous pre-earthquake stress fields which are consistent with the above coseismic slip models. Bayesian estimation can be stated as

$$p(m) = kL(m;d)p'(m), \tag{2.1}$$

where d are the observations, m is the model, $L(m;d)$ is the likelihood of the model predictions being compatible with the given observations, $p'(m)$ is the prior probability density function (PDF) of the model (*i.e.*, the prior assumptions or knowledge of m), $p(m)$ is the posterior PDF, and k is a normalization constant (*e.g.*, *Mosegaard and*

Tarantola, 1995; *Sambridge and Mosegaard*, 2002; *Tarantola*, 2005). In our case, d represents the average coseismic slip directions on each of the fault segments in the above coseismic slip models, and $m = (\phi_{\mathrm{MCS}}, \theta_{\mathrm{MCS}}, \rho_{\mathrm{MCS}},\ \sigma_{\mathrm{ICS}}/\sigma_{\mathrm{MCS}}, \sigma_{\mathrm{LCS}}/\sigma_{\mathrm{ICS}})$. As we show below, our results are weakly dependent on the relative magnitudes of the principal stresses, and thus for many of the results presented here $m = (\phi_{\mathrm{MCS}}, \theta_{\mathrm{MCS}}, \rho_{\mathrm{MCS}})$. We assume Gaussian statistics to compute the model likelihood, $L(m; d)$, using the weighted standard deviation of slip directions on each fault plane as the errors on d. A Gaussian likelihood is equivalent to exp(−L2-norm), where the L2-norm is the measure of misfit of the predictions to the observations (*e.g.*, *Mosegaard and Tarantola*, 1995; *Scales and Tenorio*, 2001). We select trial models using a Monte Carlo sampling of the prior, and then retain models randomly with a probability proportional to the model likelihood. We construct a prior using a uniform von Mises-Fisher distribution (*Fisher*, 1996), such that any given direction of the principal stresses is equally likely *a priori*. In the cases where we attempt to estimate the relative magnitudes of the principal stresses, we assume that $\log_{10}[\sigma_{\mathrm{ICS}}/\sigma_{\mathrm{MCS}}]$ and $\log_{10}[\sigma_{\mathrm{LCS}}/\sigma_{\mathrm{ICS}}]$ are uniformly distributed between -1.5 and 0. In other cases, we assume $\sigma_{\mathrm{ICS}}/\sigma_{\mathrm{MCS}} = \sigma_{\mathrm{LCS}}/\sigma_{\mathrm{ICS}} = 10^{-0.3} \approx \frac{1}{2}$. The retained (*i.e.*, accepted) models are then samples of the posterior, where high (low) density of accepted models is equivalent to a high (low) likelihood of that stress orientation being consistent with the coseismic slip models.

2.5 Regional Stresses Consistent with Coseismic Slip

In this section, we estimate an ensemble of pre-earthquake, homogeneous stress tensors that are consistent with the three coseismic slip models described above. Specifically, we determine the samples of the posteriors estimated in the Monte Carlo, Bayesian procedure. We describe the pre-earthquake stress tensor by its orientation, given by the directions of the principal stresses and the relative magnitudes of the

principal stresses. To illustrate how each of the coseismic slip models contribute to the final solution, we first determine stress orientations for each of the models independently, assuming a fixed stress magnitude. We then estimate stress orientations that are simultaneously consistent with all three of the coseismic slip models, again assuming fixed stress magnitude. We finally, estimate the orientations and relative magnitudes of stress from all three models simultaneously.

2.5.1 Independent estimation of stress orientation

We first consider each of the coseismic slip models independently, and to initially reduce the number of unknown model parameters, we fix $\sigma_{\mathrm{ICS}}/\sigma_{\mathrm{MCS}} = \sigma_{\mathrm{LCS}}/\sigma_{\mathrm{ICS}} = 10^{-0.3}$. We find that all of the models are consistent with nearly the same homogeneous pre-earthquake stress tensor. The details of the stresses inferred from each of the models differ, but all of the inferences are of an E-W trending, near horizontal MCS, a N-S trending, near horizontal ICS, and a near vertical LCS. In Fig. 2.3 we show the piercing points of the principal stress directions on the lower hemisphere of a unit sphere (*i.e.*, lower hemisphere piercing points) that were found to be statistically likely with the coseismic slip models (we do not show the results of the non-rake-constrained models of Z11). These piercing points are samples of the posterior PDFs, and the density of points indicates the likelihood of the stress direction. We also show the most likely estimate (MLE), which is the stress model resulting in the smallest misfit of the predicted slip rakes on each of the fault segments in the coseismic slip models.

The MLE of stress from each of the coseismic slip models is remarkably similar when estimated separately (Fig. 2.3). As is expected, coseismic slip models with a higher variability of slip rake on the planar fault segments result in a higher variability in the inferred directions of the principal stresses. The largest variability is in the posteriors estimated from the non-rake-constrained coseismic slip model of Z11 (model

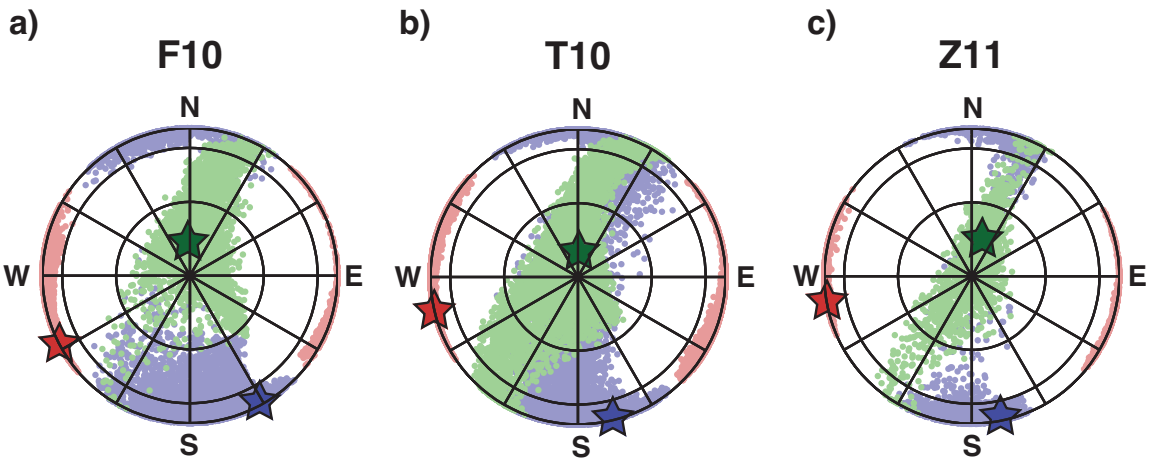

Figure 2.3: Piercing points of principal stress directions on the lower hemisphere of a unit sphere, for stresses estimated from the coseismic models of *Feng et al.* (2010; F10), *Tong et al.* (2010; T10), and *Zhang et al.* (2011a; Z11) assuming fixed relative magnitudes of the principal stresses (see main text for description of the prior). Outer circle represents horizontal directions, each circle moving inward is an increase of 30° of dip, and straight lines indicate 30° increments of azimuth. Red, blue, and green dots are most, intermediate, and least compressive stresses, respectively. Red, blue, and green stars are the most likely principal stress directions.

Z11f in Table 2.1), which is a direct manifestation of the the larger variation of inferred coseismic slip rake in that unconstrained model (Zhang et al., 2011a). As the difference between the rake-constrained and non-rake-constrained coseismic slip models of Z11 is mainly manifest in the degree of variability, we only consider the rake-constrained model of Z11 in the remainder of this section. The posterior principal stress directions estimated from the slip model of T10 also have a larger variability compared to the posteriors estimated from F10 and the rake-constrained Z11. If we include the slip below 15 km in the models of F10 and Z11, there is a similarly larger variability in the slip rake on each fault segment that results in a larger variability of permissible stress directions than those shown in Fig. 2.3a or c. Hence, the larger variability in the posteriors from the model of T10 may result from fault geometries that extend into the lower crust.

The most likely strike of the MCS is ENE-WSW, about 28°, 13°, or 10° off of

E-W in F10, T10, or Z11, respectively. The most likely MCS direction has a slight westward dip of about 5°, 3°, or 7° in F10, T10, or Z11, respectively. The most likely ICS is sub-horizontal, trending NWN-SES with a strike off of N-S of about 29°, 14°, or 11°, and a dip of about 12°, 10°, or 14° to the southwest in F10, T10, and Z11, respectively. We note that the MCS and ICS are orthogonal to each other, although the strikes of the MCS and ICS do not differ by 90° owing to the slight dips of these principal stress directions. As the LCS direction is normal to the sub-horizontal plane defined by the MCS and ICS (*i.e.*, the MCS-ICS plane), the most likely LCS direction is near vertical with a dip of about 77°, 80°, or 75° in F10, T10, or Z11, respectively (Fig. 2.3).

2.5.2 Joint estimation of stress orientation

We next estimate a homogeneous stress from the three coseismic slip models jointly, assuming fixed relative magnitudes of the principal stresses ($\sigma_{\mathrm{ICS}}/\sigma_{\mathrm{MCS}} = \sigma_{\mathrm{LCS}}/\sigma_{\mathrm{ICS}} = 10^{-0.3}$). As above, we consider the coseismic slip resolved above 15 km in models of F10 and Z11, use the rake-constrained model of Z11, and use the entire slip model of T10. As each of the three coseismic slip models use independently determined fault model geometries, we consider all three of the models jointly in order to try to capture some of the inherent variability in simplifying the actual geometry of the Wenchuan rupture using a small number of planar fault segments. We do not assign any weighting on the coseismic slip models, instead we treat each model as an equally viable representation of the coseismic slip. The error associated with any trial stress tensor is then the sum of the L2-norm misfit of the predicted rake to the observed average slip rake on each of the 13 fault segments. The standard deviation of the slip rake on each segment (Table 2.1) effectively provides a weighting of the models, whereby fault segments with a small variation of slip rake will influence the error to a larger degree as fault segments with large variation of slip rake. However,

the variation of the inferred slip rake on all of the fault segments in the three coseismic slip models is of the same order (Table 2.1), and thus no one model or fault segment influences the final estimated slip to a significantly larger degree than the others. Determining the stresses that are consistent will all three of the coseismic slip models is equivalent to the product of the three independently estimated posteriors in Fig. 2.3.

As expected, principal stress directions found to simultaneously fit the estimated coseismic slip rakes of the three coseismic slip models are consistent with the most likely stress directions found when considering the models independently (Fig. 2.4a). The orientations of the principal stresses are slightly more constrained when the three models are considered jointly compared to independently, which may be due to slight systematic biases in each of the models. Such systematic biases might result from the estimation strategies, the data, or correlations between model fault geometries (including number of segments, segment dips and strikes, etc.) and the coseismic slip estimated from the geodetic data. If present, any systematic biases in the three models may be minimized by considering all three models simultaneously.

The most likely strike and dip of the MCS, ICS, and LCS directions are $\phi_{\mathrm{MCS}} = -169^\circ$ and $\theta_{\mathrm{MCS}} = 5^\circ$, $\phi_{\mathrm{ICS}} = 102^\circ$ and $\theta_{\mathrm{ICS}} = -11^\circ$, and $\phi_{\mathrm{LCS}} = 77^\circ$ and $\theta_{\mathrm{LCS}} = 77^\circ$, respectively. The highest likelihood MCS directions are dipping about 0–10° westward and striking approximately E-W from about 10° north of west to about 15–20° south of west (Figs. 2.3 and 2.4a). There is a lower likelihood that the MCS direction is eastward dipping, and there is a strong trade-off between the strike and dip of the MCS (Fig. 2.5a). In general, horizontal to eastward dipping MCS orientations are more ESE-WNW trending, while westward dipping MCS orientations are more ENE-WSW trending. The inferred ICS directions are also sub-horizontal, and roughly N-S trending (Fig. 2.4). The highest likelihood in ICS directions are southward dipping, with dips up to about 20–30°, there is no apparent correlation between the strike

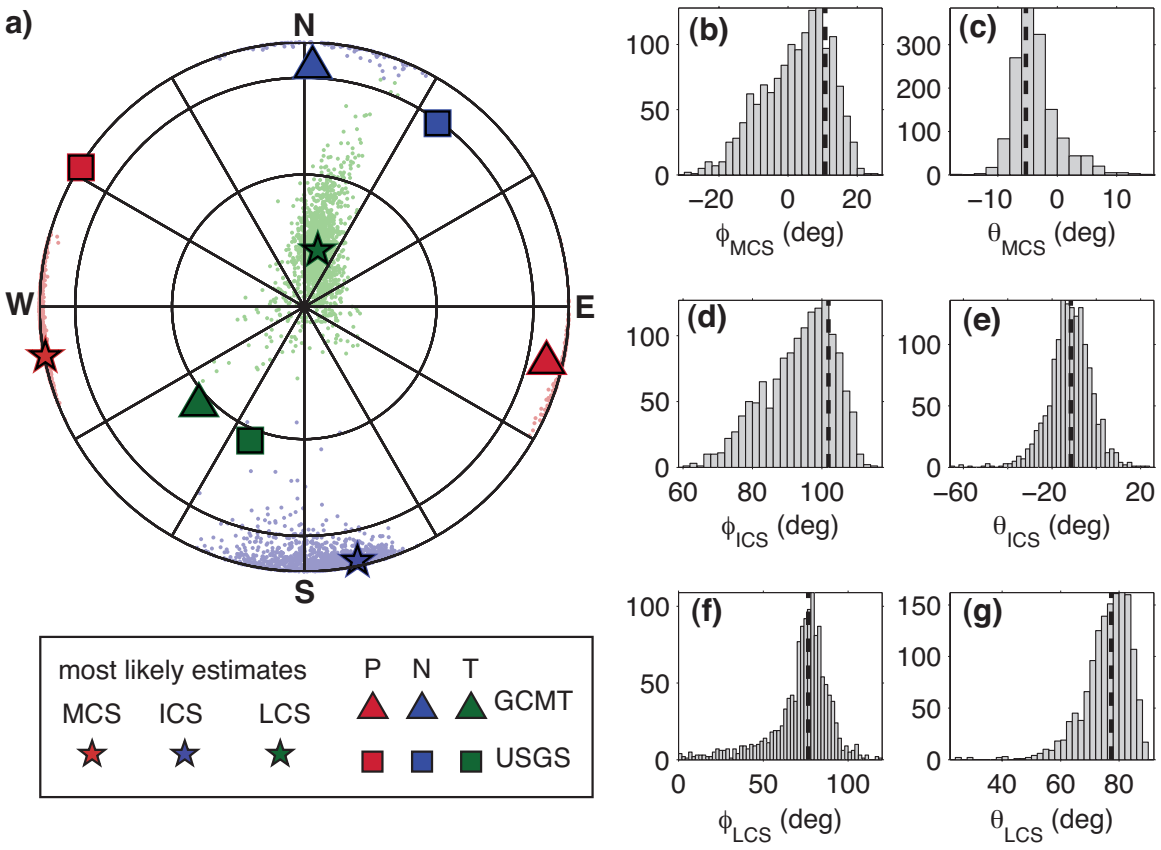

Figure 2.4: Principal stress directions from a joint estimation of the coseismic models of *Feng et al.* (2010), *Tong et al.* (2010), and *Zhang et al.* (2011a) assuming fixed relative magnitudes of the principal stresses. (a) Lower hemisphere piercing points of the principal stress directions (symbols are as in Fig. 2.3, and the principal axes of the Global CMT (GCMT; triangles) and USGS (squares) focal mechanism solutions are also shown. (b–g) Histograms of the strike, ϕ_X, and dip, θ_X, of the MCS, ICS and LCS directions depicted in (a); note that a principal stress can be described by (ϕ_X,θ_X) or ($\phi_X \pm 180°$,$-\theta_X$). Vertical dashed lines represent the most likely orientations.

and dip of the ICS directions (Fig. 2.5b). The highest likelihood in LCS directions are 0–30° off of vertical and trending NEN-SWS, about 20° off of north (Fig. 2.4). LCS directions that are dipping less than about 50° from horizontal are less likely. These inferred directions of the LCS are in contrast to the principal stress directions estimated independently from the coseismic slip model of T10, in which case there is a likelihood that the LCS may be southwestward dipping (Fig. 2.3b). As all of the principal stress directions are orthogonal to each other, there are expected trade-offs

between them. For instance, the strike of the ICS is correlated with the strike of the MCS, and the dip of the LCS is correlated with the dip of the MCS. However, we find no correlation between the dip of the ICS and, either the strike or dip of the MCS direction (Fig. 2.5), nor is there a correlation between the strike of the ICS and dip of the LCS direction.

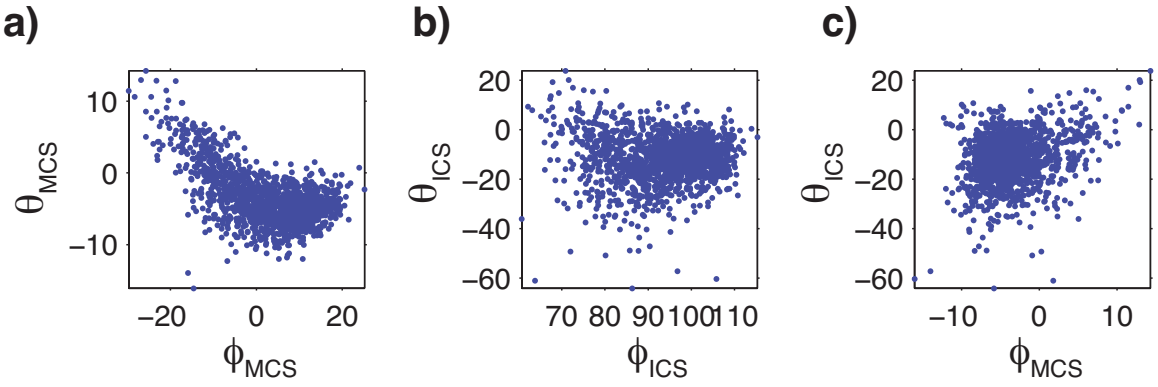

Figure 2.5: Strike, ϕ_X, and dip, θ_X of the most and intermediate compressive principal stress directions shown in Fig. 2.4.

Our motivation in this study is not to only find the most likely homogeneous stress tensors from the three coseismic slip models, but to determine whether these homogeneous stress tensors can adequately describe the inferred correlation between coseismic slip direction and fault geometry. In Fig. 2.6 we show histograms of the predicted slip rakes on each of the 13 planar fault segments in the coseismic slip models described in Section 2.3) along with the Gaussian PDFs that best describe the variation of inferred coseismic slip on each segment of the coseismic slip models (*i.e.*, using the weighted mean and standard deviation of coseismic slip in Table 2.1). On almost all of the segments, the most likely predicted rakes are consistent with the average modeled coseismic rake (Table 2.1). One exception is the fault segment approximating the Pengguan fault in the coseismic slip model of F10. F10 constrained the slip on their Pengguan fault segment to be pure thrust; however, most of the homogeneous stress tensors tend to predict a component of right-lateral

motion on the Pengguan (Fig. 2.6a). The prediction of some right-lateral motion on the Pengguan fault segment of F10 is also apparent when the coseismic slip model of F10 is considered independently, and thus this is not a result of considering the three models jointly. We note that the models of T10 and Z11 both contain some right-lateral motion on their fault segments approximating the Pengguan fault (Table 2.1), and although most of the mapped fault scarps on the Pengguan fault were thrust, there were a few right-lateral offsets (*Liu et al.*, 2009; *Lin et al.*, 2009; *Xu et al.*, 2009).

2.5.3 Joint estimation of stress orientation and relative magnitude

In the above sections, we estimate the directions of the principal stresses assuming fixed magnitudes of the principal stresses. Here we estimate the relative magnitudes of the principal stresses jointly from the three coseismic slip models and allow the relative magnitudes of the principal stresses to vary (see Section 2.4.2 for a description of the prior). When varying the stress magnitudes, the permissible orientations of the stresses that we find are quite similar to those found above, although with a slightly larger variation of the principal stress directions (Fig. 2.7c). The correlations between the principal stress directions, as well as the predicted coseismic slip rakes in these models, are likewise similar to those found when the stress magnitudes are assumed *a priori*.

We find that the relative magnitudes of the principal stresses are not well constrained using only the direction of coseismic slip on each of the fault segments in the coseismic models of F10, T10, and Z11. Of the stress magnitudes that we have tried, there is a slight preference for $\sigma_{\mathrm{ICS}}/\sigma_{\mathrm{MCS}} \approx 0.3$, and there is a weak trade-off with $\sigma_{\mathrm{LCS}}/\sigma_{\mathrm{ICS}}$ (Fig. 2.7b). There is also a weak correlation between θ_{MCS} and $\sigma_{\mathrm{ICS}}/\sigma_{\mathrm{MCS}}$ (Fig. 2.7d). The correlation is such that west dipping MCS directions tend to be associated with lower magnitudes of the ICS relative to the MCS, whereas east dip-

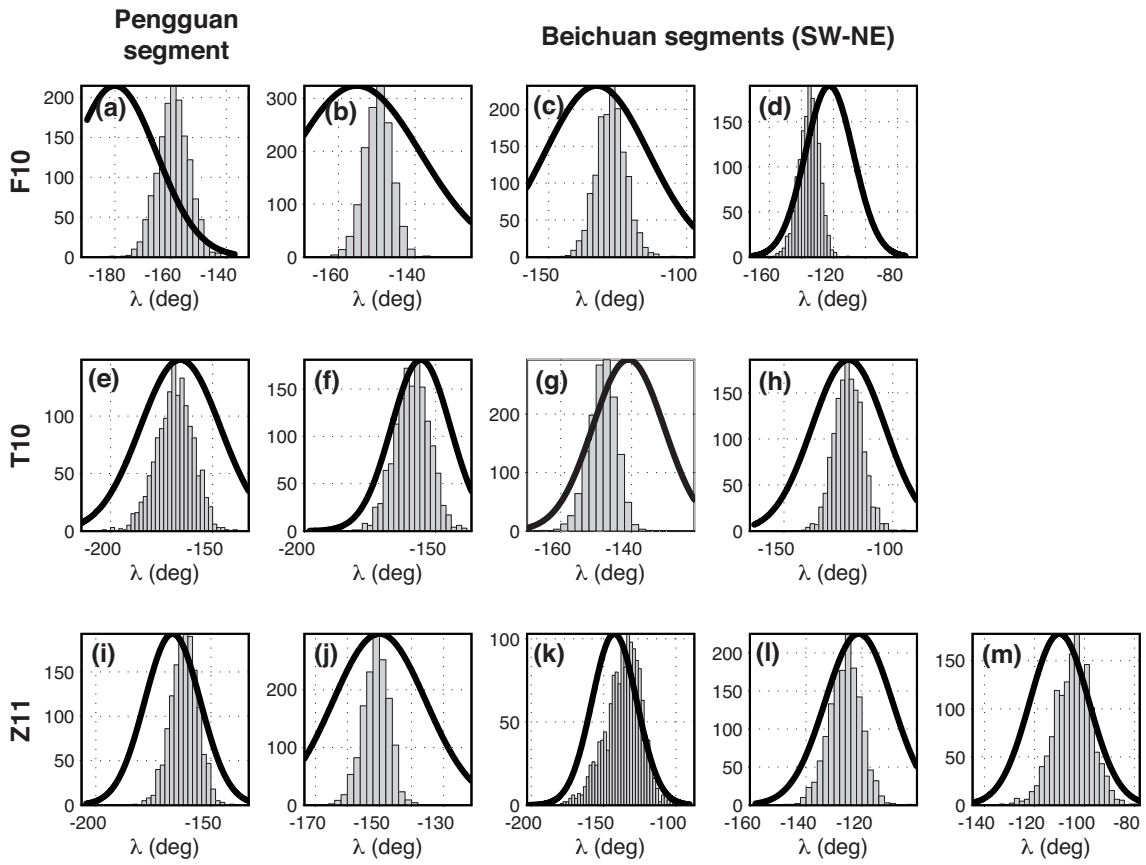

Figure 2.6: Histograms of the predicted slip rake, λ, on the fault segments in the coseismic models of *Feng et al.* (2010; F10), *Tong et al.* (2010; T10), and *Zhang et al.* (2011a; T11), predicted by the stresses shown in Fig. 2.4. Solid black lines indicate the slip directions inferred in the coseismic models by the Guassian probability density functions given by the mean and standard deviation of slip direction on each of the fault segments (Table 2.1; Gaussians are scaled so that they are on the same range as the histograms). (a), (e), and (i) correspond to segments approximating the Pengguan fault, and the rest of the panels correspond to segments approximating the Beichuan fault, segments from the SW to NE end of the Beichuan fault are arranged from left to right.

ping MCS directions tend to be favored when the magnitudes of the MCS and ICS are more similar. The correlation between dip and strike of the MCS direction is similar as in Fig. 2.5a, and thus east dipping MCS directions tend to be WNW-ESE trending, and west dipping directions tend to be WSW-ENE trending. Surprisingly, we find no obvious correlations between the directions of the ICS or LCS with the relative magnitudes of the principal stresses (Fig. 2.7a).

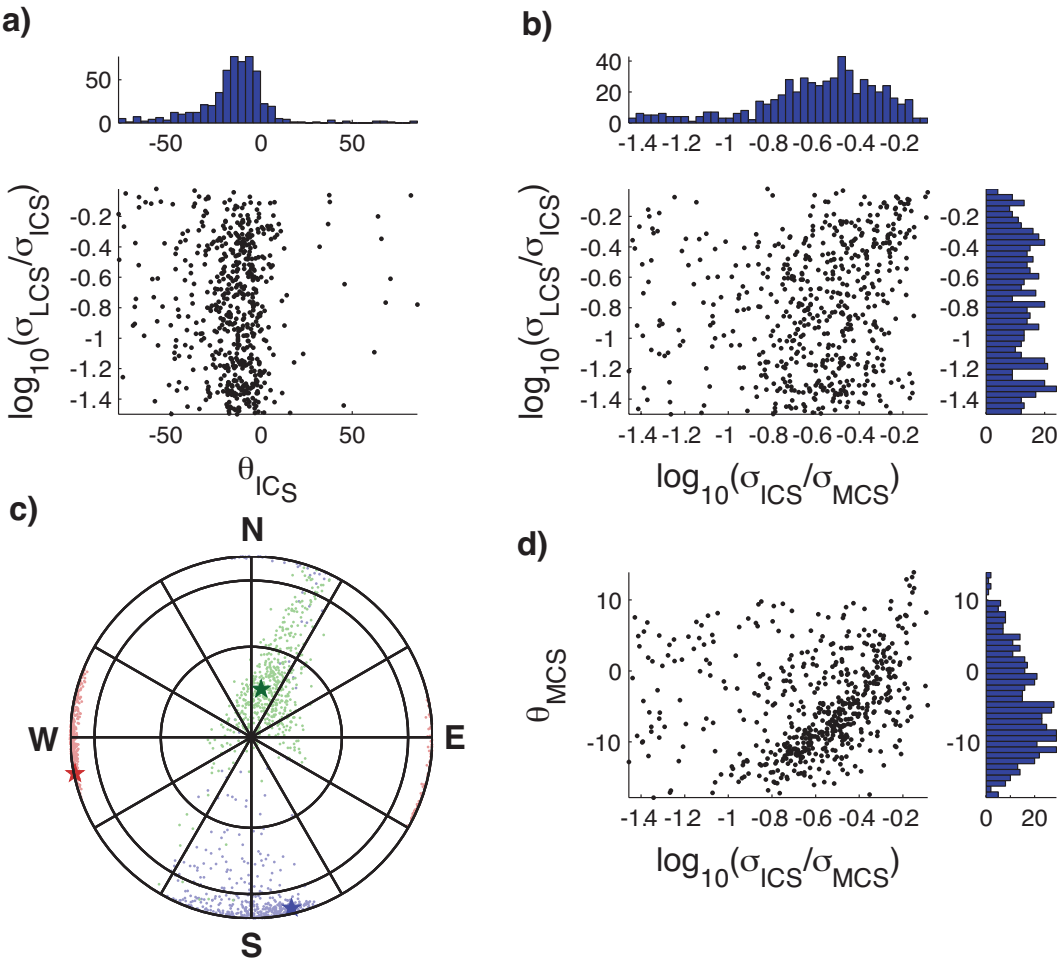

Figure 2.7: Principal stress orientations and relative magnitudes estimated from the coseismic models of *Feng et al.* (2010), *Tong et al.* (2010), and *Zhang et al.* (2011a). Panel (c) shows the lower hemisphere piercing points of the principal stresses (see Fig. 2.3 for description of symbols). (a), (b), and (d) show the dip of the MCS or ICS, θ_{MCS} or θ_{ICS}, versus the relative magnitudes of the most, intermediate, and least compressive stresses, σ_{MCS}, σ_{ICS}, and σ_{LCS}, respectively; $\theta_{\mathrm{MCS}} > 0$ (< 0) are east (west) dipping, and $\theta_{\mathrm{ICS}} > 0$ (< 0) are north (south) dipping. Histograms on the edges of (a), (b), and (d) are of the dips and relative magnitudes of the estimated stresses.

2.6 Discussion

The coseismic slip models of F10, T10, and Z11 simplify the fault geometry of the Wenchuan earthquake rupture with four or five planar fault segments, and resolve a variation of slip rake on each segment. The variation of inferred slip rake on each segment may indicate the actual variability in coseismic slip in the Wenchuan

earthquake, either due to local heterogeneities of pre-earthquake shear stresses on the fault, or due to the dynamics of the rupture process. Alternatively, the inferred variability on each planar segment may be due to uncertainties in the estimation of fault slip at depth from geodetic data, and/or biases in the inferred coseismic slip rake resulting from incomplete approximations of the actual fault geometry. In this paper, we have treated the variability in the coseismic slip rake essentially as an error in the coseismic models. It could also be that the variability of rake is physical, in which case our results are merely reflecting the average regional stress, and our analysis is insensitive to smaller scale stress heterogeneities on the individual fault segments.

When considered independently, the coseismic slip model of T10 shows a rather large variation in the ICS and LCS directions (Fig. 2.3b). As in the other models, the most likely LCS orientation is steeply dipping northward. However, in the posterior estimated from T10, LCS directions ranging from vertical to horizontal are all likely. Due to the orthogonality of the ICS and LCS direction, when the LCS is shallowly dipping, the ICS is more vertical. This lack of control on the dip of the LCS and ICS in the estimation using only the coseismic slip model of T10 might reflect that there is a heterogeneous stress field in the region of the rupture. For instance, with a vertically oriented LCS at the SW of the Beichuan fault, a more thrust-like Andersonian stress state, and with a horizontally oriented LCS at the NE, a more strike-slip-like Andersonian stress state. However, the posteriors estimated from the F10 and Z11 coseismic models do not show this large variability in the dips of the ICS and LCS. The posteriors estimated from the model of Z11 show a much lower likelihood of shallow dipping LCS directions. The posteriors estimated from F10 show low likelihood of the LCS direction being shallowly dipping to the south, but a relatively large likelihood of the LCS being shallowly dipping to the north (Fig. 2.3a). Estimating the likelihood of stress tensors from all three models jointly yields much tighter constraints on the dip of the LCS and ICS (Fig. 2.4). As the posteri-

ors from the joint estimation are equivalent to the product of the posteriors shown in Fig. 2.3, the directions of the ICS and LCS in Fig. 2.4a are the likely principal stress directions common to all three of the independent posteriors. Additionally, we see a much larger variation in the dips of the ICS and LCS when we estimate a single stress state from the models of F10 and Z11 using the entire inferred slip down do 30 km depth, or when we use the model-resolution-based fault discretization in Z11. This leads us to the conclusion that the solutions with shallow dipping LCS are affected by slip at depths below about 15 km in the coseismic slip models. The inferred slip at these depths is less well resolved (*e.g.*, *Tong et al.*, 2010; *Zhang et al.*, 2011a), and may be slip that is actually occurring on near-vertical detachment faults that are mapped onto the steeper fault segments at depth in the inversions of the geodetic data. In any case, without further constraints on coseismic slip, we posit that the pre-earthquake stress tensors with shallowly dipping LCS directions reflect uncertainties in the estimations of coseismic slip.

Principal stress directions are often estimated directly from the P, T, and N axes (*i.e.*, the principal axes) of earthquake focal mechanisms (*e.g.*, *McKenzie*, 1969; *Gephart and Forsyth*, 1984). The most compressive stress direction is in the focal mechanism quadrant containing the P axis, and the exact correspondence between the MCS and LCS directions and an earthquake focal mechanism requires consideration of Coulomb friction (*e.g.*, *McKenzie*, 1969). The directions of the principal stresses that we infer from the coseismic slip models are broadly consistent with the principal axes from the global CMT (GCMT) and USGS focal mechanisms, in that the P, N, and T axes are in the quadrants containing the most likely MCS, ICS, and LCS, respectively (Fig. 2.4a). Both the GCMT and USGS focal mechanisms contain some non-double-couple component, with the magnitudes of the N axis on the order of one tenth the absolute values of the magnitudes of the P and T axes. This non-double-couple component likely reflects the change in fault dip and slip rake from

the SW to the NE (*Nakamura et al.*, 2010). The principal axes of the focal mechanisms are about 30–50° from the most likely principal stress directions, which may be related to the Coulomb stability of the faults.

Based on aftershock focal mechanisms, both *Wang et al.* (2009) and *Cai et al.* (2011) infer that the most compressive stress direction rotates significantly along the LMSfz. This heterogeneous stress field is in contrast to the homogeneous pre-earthquake stress we infer. Aftershocks are not solely due to the stresses prior to the mainshock, but also the coseismic stress changes during the mainshock (*e.g.*, *King et al.*, 1994). Hence, the aftershocks following the Wenchuan earthquake do not necessarily reflect just the pre-earthquake stresses. The aftershock focal mechanisms might be used to further constrain the pre-earthquake stress field by including the coseismic stress changes predicted by the coseismic slip models. Relating aftershocks to a spatially-dependent pre-mainshock stress, $\sigma_{\rm pre}(\vec{x})$, requires consideration of the heterogenous coseismic stresses, $\sigma_{\rm co}(\vec{x})$, and any stresses due to time-dependent postseismic processes, $\sigma_{\rm post}(\vec{x},t)$. Postseismic stresses may be due to earlier aftershocks or to postseismic processes such as localized or distributed creep at depth. A given aftershock is then not necessarily only due to the pre-mainshock stress, but the stress at the location and time of a given aftershock given as

$$\sigma(\vec{x},t) = \sigma_{\rm pre}(\vec{x}) + \sigma_{\rm co}(\vec{x}) + \sigma_{\rm post}(\vec{x},t). \tag{2.2}$$

In the case of a homogeneous pre-earthquake stress, as we argue for here, $\sigma_{\rm pre}(\vec{x})$ would be a spatially-independent tensor.

The two end-member models explaining the deformation in the LMSfz are upper crustal shortening (*e.g.*, *Hubbard and Shaw*, 2009) and crustal uplift due to lower crustal flow (*e.g.*, *Royden et al.*, 2008). Predictions of stresses from geodynamic models can potentially be tested against the stress we infer in the LMSfz. However,

it is unknown if the pre-earthquake stress we find is more representative of long-term geodynamic processes or the mechanics of the earthquake cycle. From slickensides on faults in the LMSfz, *Chen and Wilson* (1996) inferred a roughly NW-SE shortening direction, which is approximately normal to the trace of the Beichuan fault. Such a shortening direction might be indicative of a compressive stress direction, although it does not necessarily reflect a principal stress direction. For instance, if the MCS and ICS are of comparable magnitude, the singular direction they surmised may be affected by both the MCS and ICS. As the MCS and ICS directions we infer are both near-horizontal, the roughly E-W trending MCS and N-S trending ICS directions may be equivalent to simple shear stress in the horizontal plane. The orientation of the equivalent simple shear will depend on the relative magnitudes of the most and intermediate compressive stresses. Here we find that the magnitude of the ICS is about 30% of the magnitude of the MCS (Fig. 2.4), so the trend of the simple shear may be similar to the strike of the LMSfz. The amount of compression on the LMSfz depends on the magnitude of the ICS relative to the MCS, which would cause the orientation of the equivalent simple shear to rotate. A component of simple shear on the LMSfz prior to the Wenchuan earthquake implies that the LMSfz is not a pure thrust system, but contains a large degree of strike-slip motion. Indeed, there is paleosesmic evidence for large strike-slip motion in the LMSfz (*Densmore et al.*, 2007), and several models of interseismic strain accumulation on the LMSfz infer a large amount of strike-slip accumulation relative to the thrust slip accumulation (*Meade*, 2007; *Shen et al.*, 2009; *Loveless and Meade*, 2011).

In this paper, we do not address the issue of frictional stability on the fault planes, instead we simply assume that the coseismic slip is in the direction of the maximum shear stress on the fault that has accumulated during the interseismic period. We also find that the direction of coseismic slip has little constraint on the relative magnitudes of the principal stresses. In Coulomb frictional stability with

a non-zero coefficient of friction, not all faults will fail in a given stress state (*e.g.*, *Sibson*, 1977; *Townend and Zoback*, 2004; *Rice*, 1992). Rather failure will occur only if the ratio of the magnitude of the fault shear stress to the fault normal stress is above the coefficient of friction. The magnitude of both the fault shear and normal stresses strongly depend on the magnitudes and orientations of the principal stresses. *Xu et al.* (2008) argued that the geometries of the faults that ruptured in the Wenchuan earthquake indicated that fault pore fluid pressure was greater than lithostatic prior to the Wenchuan earthquake. *Xu et al.* (2008) implicitly assumed that the MCS direction was horizontal and normal to the trend of the Beichuan fault in their 2D Coulomb frictional analysis. Our results demonstrate that the MCS direction is at a higher angle to the trend of the Beichuan fault, and a 3D Coulomb frictional stability analysis may not require fault pore fluid pressure to be above lithostatic pressure prior to the Wenchuan earthquake. Although static Coulomb friction theory provides a framework for evaluating the preference for a given stressed fault to fail (*e.g.*, *King et al.*, 1994; *Das and Henry*, 2003; *Parsons et al.*, 2008; *Ge et al.*, 2009), it is important to consider the dynamic stresses during an earthquake rupture when considering the variation of coseismic slip on faults with geometric variations (*e.g.*, *Poliakov et al.*, 2002; *Kame et al.*, 2003; *Fliss et al.*, 2005). Consideration of frictional stability has the potential to further constrain the relative magnitudes of the principal stresses, as well as the principal stress directions.

2.7 Conclusions

Models of the coseismic slip in the Wenchuan earthquake reveal a marked change in coseismic slip rake, from more thrust slip in the SW to more right-lateral strike slip in the NE (*Kobayashi et al.*, 2009; *Liu et al.*, 2009; *Lin et al.*, 2009; *Xu et al.*, 2009; *Shen et al.*, 2009; *Feng et al.*, 2010; *Hashimoto et al.*, 2010; *Tong et al.*, 2011; *Zhang et al.*, 2011a). Moreover, these models indicate that there is a correlation

between the coseismic slip rake and the fault dip. Our motivation is to test whether the change in coseismic slip rake is consistent with a homogeneous pre-earthquake stress, or whether a heterogeneous stress field is required. Assuming that the average coseismic slip is in the direction of the maximum pre-earthquake shear stress on each fault segment (*e.g.*, *Angelier*, 1979; *Gephart and Forsyth*, 1984), we find that a homogeneous pre-earthquake stress is consistent with the geodetically constrained coseismic models of *Feng et al.* (2010), *Tong et al.* (2010), and *Zhang et al.* (2011a). The most compressive stress is near horizontal and oriented roughly east-west, and the intermediate compressive stress is roughly north-south trending and also sub-horizontal. The inferred stress orientations we find here can be used to test dynamic and mechanical models of deformation of the LMSfz.

We find that the inferred slip rake in the coseismic models does not fully constrain the relative magnitudes of the principal stresses, but that there is a slight indication that the magnitude of the ICS is about 30% the MCS magnitude. Further analysis considering aftershock focal mechanisms and/or frictional stability has the potential to further constrain the magnitudes of the pre-earthquake principal stresses in the LMSfz. Knowledge of the pre-earthquake stress field may aid the estimation of future earthquake risk in the LMSfz, beyond that of just considering the static coseismic stress changes from the mainshock. Finally, the analysis we present can be applied to other large earthquakes in which coseismic models indicate changes in coseismic slip rake on varying fault geometries, such as the 2010 Haiti and 2010 Darfield, NZ earthquakes.

2.8 Acknowledgements

We are appreciative of comments from J. Ning and one anonymous reviewer. We thank the Rackham Graduate School, University of Michigan, for a Rackham Merit Fellowship to L. Medina Luna. Matlab (The Mathworks, Inc.) was used for all

calculations and to generate all figures presented in this paper.

2.9 References

Anderson, E. M., 1951. The Dynamics of faulting and dyke formations with applications to Britain, 2nd Edition. Edinburgh: Oliver and Boyd. Print.

Angelier, J., 1979. Determination of the mean principal directions of stresses for a given fault population. *Tectonophysics*, 56, T17T26, doi: 10.1016/0040-1951(79)90081-7.

Barbor, S., Fialko, Y., Bock, Y., 2009. Postseismic deformation due to the Mw 6.0 2004 Parkfield earthquake: Stress-driven creep on a fault with spatially variable rate-and-state friction parameters. *J. Geophys. Res.*, 114, B07405, doi:10.1029/2008JB005748.

Burchfiel, B., Royden, L., van der Hilst, R., Hager, B., Chen, Z., King, R., Li, C., Lü, J., Yao, H., Kirby, E., 2008. A geological and geophysical context for the Wenchuan earthquake of 12 May 2008, Sichuan, People's Republic of China. *GSA Today*, 18, no. 4-11, doi:10.1130/GSATG18A.1.

Cai, C., Yu, C., Tao, K., Hu, X., Tian, Y., Zhang, H., Cui, X., Ning, J., 2011. Spatial distribution and focal mechanism solutions of the Wenchuan earthquake series: results and implications. Earthquake *Science*, 24, 115125, doi: 10.1007/s11589-011-0775-5.

Chen, S., and Wilson, J., 1996. Emplacement of the Longmen shan thrust-nappe belt along the eastern margin of the Tibetan Plateau. *J. Struct. Geol.*, 18, 413-430.

Clark, M., Bush, J., Royden, L., 2005. Dynamic topography produced by lower crustal flow against rheological strength heterogeneities bordering the Tibetan Plateau. *Geophys. J. Int.*, 162, 575-590.

Clark, M., Royden, L., 2000. Topographic ooze: Building the eastern margin of Tibet by lower crustal flow. *Geology*, 28, 703-706.

Das, S., Henry, C., 2003. Spatial relation between main earthquake slip and its aftershock distribution. *Rev. Geophys.*, 41, 1013, doi:10.1029/202RG000119.

Densmore, A., Ellis, M., Li, Y., Zhou, R., Hancock, G., Richardson, N., 2007. Active tectonics of the Beichuan and Pengguan faults at the eastern margin of the Tibetan Plateau. *Tectonics*, 26, TC4005, doi:10.1029/2006TC001987.

Feng, G., 2011. Coseismic deformation and ionospheric variation associated with the Wenchuan earthquake estimated from InSAR. Ph.D. thesis. The Hong Kong Polytechnic University. Hong Kong, China.

Feng, G., Hetland, E., Ding, X., Li, Z., and Zhang, L., 2010. Coseismic fault slip of the 2008 Mw 7.9 Wenchuan earthquake estimated from InSAR and GPS measurements. *J. Geophys. Res.*, 37, L01302, doi:10.1029/2009GL041213.

Fialko, Y., Sandwell, D., Simons, M., Rosen, P., 2005. Three-dimensional deformation caused by the Bam, Iran, earthquake and the origin of shallow slip deficit. *Nature*, 435, 295-299.

Fisher, N., 1996. Statistical Analysis of Circular Data. Cambridge *University Press*, New York, NY, USA.

Fliss, S., Bhat, H., Dmowska, R., Rice, J., 2005. Fault branching and rupture directivity. *J. Geophys. Res.*, 110, B06312, doi:10.1029/2004JB003368.

Ge, S., Liu, M., Lu, N., Godt, J., Luo, G., 2009. Did the Zipingpu reservoir trigger the 2008 Wenchuan earthquake? *Geophys. Res. Let.*, 36, L20315, doi:10.1029/2009GL040349.

Gephart, J., and Forsyth, D., 1984. An improved method for determining the regional stress tensor using earthquake focal mechanism data: Application to the San Fernando earthquake sequence. *J. Geophys. Res.*, 89, 9305-9320, doi: 10.1029/JB089iB11p09305.

Hao, K.X., Si, H., Fujiwara, H. & Ozawa, T., 2009. Coseismic surface-ruptures and crustal deformations of the 2008 Wenchuan earthquake Mw7.9, China, *Geophys. Res. Let.*, 36, L11303, doi:10.1029/2009GL037971.

Hashimoto, M., Enomoto, M. & Fukushima, Y., 2010. Coseismic deformation from the 2008 Wenchuan, China, earthquake derived from ALOS/PALSAR images,

Tectonophysics, 491, 59–71, doi:10.1016/j.tecto.2009.08.034.

Hetland, E.A., Simons, M. & Dunham, E.M., 2010. Postseismic and interseismic deformation due to fault creep I: Model description, *Geophys. J. Int.*, 81, 81–98, doi:10.1111/j.1365-246X.2010.04522.x.

Huang, Y., Wu, J.P., Zhang, T.Z. & Zhang, D.N., 2008. Relocation of the M8.0 Wenchuan earthquake and its aftershock sequence (in Chinese), *Sci. China*, 51, 1703–1711.

Hubbard, J. & Shaw, J.H., 2009. Uplift of the Longmen Shan and Tibetan plateau, and the 2008 Wenchuan, *Nature*, 458, 194–197.

Kame, N., Rice, J.R. & Dmowska, R., 2003. Effects of prestress and rupture velocity on dynamic fault branching, *J. Geophys. Res.*, 108, 2265, doi:10.1029/2002JB002189.

King, G.C.P., Stein, R.S. & Lin, J., 1994. Static stress changes and the triggering of earthquakes, *Bull. Seismol. Soc. Am.*, 84, 935–953.

Kobayashi, T., Takada, Y., Furuya, M., Murakami, M., 2009. Locations and types of ruptures involved in the 2008 Sichuan earthquake inferred from SAR image matching, *Geophys. Res. Let.*, 36, L07302, doi:10.1029/2008GL036907.

Lin, A., Ren, Z., Jia, D. & Wu, X., 2009. Co-seismic thrusting rupture and slip distribution produced by the 2008 Mw 7.9 Wenchuan earthquake, China, *Tectonophysics*, 471, 203–215.

Liu, Z., Zhang, Z., Wen, L., Tapponnier, P., Sun, J., Xing, X., Hu, G., Xu, Q., Zeng, L., Ding, L., Ji, C., Hudnut, K.W. & van, J., 2009. Co-seismic ruptures of the 12 May 2008, Ms 8.0 Wenchuan earthquake, Sichuan: East-west crustal shortening on oblique, parallel thrusts along the eastern edge of Tibet, *Earth Planet Sci. Lett.*, 286, 355–370, doi:10.1016/j.epsl.2009.07.017.

Loveless, J.P. and Meade, B.J., 2011. Partitioning of localized and diffuse deformation in the Tibetan Plateau from joint inversions of geologic and geodetic observations, *Earth Planet Sci. Lett.*, 303, 11–24, doi:10.1016/j.epsl.2010.12.014.

McKenzie, D.P., 1969. The relation between fault plane solutions for earthquakes and the directions of the principal stresses, *Bull. Seismol. Soc. Am.*, 59, 591–601.

Meade, B.J., 2007. Present-day kinematics at the India-Asia collision zone, *Geology*, 35, 81–84.

Mosegaard, K. and Tarantola, A., 1995. Monte Carlo sampling solutions to inverse problems, *J. Geophys. Res.*, 100, 12,431–12,447.

Nakamura, T., Tsuboi, S., Keneda, Y., Yamanaka, Y., 2010. Rupture process of the 2008 Wenchuan, China earthquake inferred from teleseismic waveform inversion and forward modeling of broadband seismic waves, *Tectonophysics*, 491, 72–84, doi:10.1016/j.tecto.2009.09.020.

Parsons, T., Ji, C., and Kirby, E., 2008. Stress changes from the 2008 Wenchuan earthquake and increased hazard in the Sichuan basin, *Nature*, 454, 509–510.

Poliakov, A.N.B., Dmowska, R., Rice, J.R., 2002. Dynamics shear rupture interactions with fault bends and off-axis secondary faulting, *J. Geophys. Res.*, 107, 2295, doi:10.1029/2001JB000572.

Rice, J.R., 1992. Fault stress states, pore pressure distributions, and the weakness of the San Andreas fault, in *Fault Mechanics and Transport Properties of Rocks*, Academic Press Ltd, 475-503.

Royden, L.H., Burchfiel, B.C., van der Hilst, R., 2008. The geologic evolution of the Tibetan plateau, *Science*, 321, 1054–1058.

Sambridge, M. and Mosegaard, K., 2002. Monte Carlo methods in geophysical inverse problems, *Rev. Geophys.*, 40, 1009, doi:10.1029/2000RG000089.

Scales, J.A. and Tenorio, L., 2001. Prior information and uncertainty in inverse problems, *Geophysics*, 66, 389–397.

Sibson, R.H., 1977. Fault rocks and fault mechanics, *J. Geol. Soc. Lond.*, 133, 191–213.

Sibson, R.H., 1985. A note on fault reactivation, *J. Struct. Geol.*, 7, 751–754.

Shen, Z.K., Sun, J., Zhang, P.Z., Wan, Y.G., Wang, M., Bürgmann, R., Zeng, Y.H., Gan, W.J., Liao, H. and Wang, Q.L., 2009. Slip maxima at fault junctions and rupturing of barriers during the 2008 Wenchuan earthquake, *Nature Geoscience*, 2, 718–724, doi:10.1028/NGE0636.

Tapponnier, P., Xu, X.Q., Roger, F., Meyer, B., Arnaud, N., Wittlinger, G. and Yang, J.S., 2001. Oblique stepwise rise and growth of the Tibet Plateau, *Science*, 294, 1671–1677.

Tarantola, A., 2004. Inverse Problem Theory and Methods for Model Parameter Estimation, SIAM, Philadelphia.

Thatcher, W., 2007. Microplate model for the present-day deformation of Tibet, *J. Geophys. Res.*, 112, B01401, doi:10.1029/2005JB004244.

Tong, X., Sandwell, D.T., and Fialko, Y., 2010. Coseismic slip model of the 2008 Wenchuan earthquake derived from joint inversion of interferometric synthetic aperture radar, GPS, and field data, *J. Geophys. Res.*, 115, B04314, doi:10.1029/2009JB006625.

Townend, J. and Zoback, M.D., 2004. Regional tectonic stress near the San Andreas fault in central and southern California, *Geophys. Res. Let.*, 31, L15S11, doi:10.1029/2003GL018918.

Wang, Q., Chen, Z., and Zheng, S., 2009. Spatial segmentation characteristic of focal mechanism of aftershock sequence of Wenchuan earthquake, *Chinese Sci. Bull.*, 54, 2263–2270, doi:10.1007/s11434-009-036709.

Wang, W., Sun, W., and Jiang, Z., 2010. Comparisons of fault models of the 2008 Wenchuan earthquake (Ms8.0) and spatial distributions of co-seismic deformations, *Tectonophysics*, 491, 85–95, doi:10.1016/j.tecto.2009.08.035.

Xu, Z., Ji, S., Li, H., Hou, L., Fu, X., and Cai, Z., 2008. Uplift of the Longmen Shan range and the Wenchuan earthquake, *Episodes*, 31, 291–301.

Xu, X.W., Wen, X., Yu, G., Chen, G., Klinger, Y., Hubbard, J., and Shaw, J., 2009.

Co-seismic reverse-and oblique-slip surface faulting generated by the 2008 Mw7.9 Wenchuan earthquake, China, *Geology*, 37, 515–518, doi:10.1130/G25462A.1.

Yu, T., Mao, T., Wang, Y., and Wang, J., 2009. Study of the ionospheric anomaly before the Wenchuan earthquake, *J. Chinese Sci. Bull.*, 54, 1080–1086, doi: 10.1007/s11434-008-0587-8.

Zhang, P., Shen, Z., Wang, M., Gan, W., Bürgmann, R., Molnar, P., Wang, Q., Niu, Z., Sun, J., Wu, J., Sun, H., You, Z., 2004. Continuous deformation of the Tibetan Plateau from Global Positioning System data, *Geology*, 32, 809–812, doi:10.1130/G20554.1.

Zhang, Y., Feng, W., Xu, L., Zhou, C., and Chen, Y., 2008. Spatio-temporal rupture process of the 2008 great Wenchuan earthquake, *Sci. China.*, 52, 145–154.

Zhang, G., Qu, C., Shan, X., Song, X., Zhang, G., Wang, C., Hu, J.-C., and Wang, R., 2011a. Slip distribution of the 2008 Wenchuan Ms 7.9 earthquake by joint inversion from GPS and InSAR measurements: A resolution test study, *Geophys. J. Int.*, 186, 207–220, doi:10.1111/j,1365-246X.2011.05039.x.

Zhang, H.-P., Zhang, P.-Z., Kirby, E., Liu, C.-R., and Yu, G.-H., 2011b. Along-strike topographic variation of the Longmen Shan and its significance for landscape evolution along the eastern Tibetan Plateau, *J. Asian Earth Sci.*, 40, 855–864, doi:10.1016/j.jseaes.2010.05.015.

Zhou, Y., Wu, Y., Qiao, X., and Zhang, X., 2009. Ionospheric anomalies detected by ground-based GPS before the Mw7.9 Wenchuan earthquake of May 12, 2008, China, *J. Atmos. Solar-Terres. Phys.*, 71, 959–966.

CHAPTER 3

Potential ambiguities in the interpretation of stress inferred from focal mechanisms: An application to aftershocks of the 2008 Wenchuan earthquake

3.1 Abstract

We present a Bayesian Monte Carlo method to infer stress that led to a given earthquake from the focal mechanism solution of that earthquake, allowing for a mechanical constraint to ensure fault slip is consistent with Mohr-Coulomb failure. Using synthetic focal mechanisms consistent with known stresses and a Bayesian Monte Carlo estimation strategy, we show that the probability of correctly interpreting the inferred stress is relatively low. Furthermore, the principal stresses are mis-identified in the posterior estimated from focal mechanisms when the intermediate compressive stress is farther than about 20° from the focal mechanism N axis. Assumptions of fault friction can further constrain permissible stresses, and have the potential to resolve which nodal plane corresponds to the slip surface. We infer stress from focal

This chapter to be submitted to Bull. Seism. Soc. Am. as: L. Medina Luna and E. A. Hetland, Potential ambiguities in the interpretation of stress inferred from focal mechanisms: An application to aftershocks of the 2008 Wenchuan earthquake.

mechanisms of aftershocks of the 2008 Wenchuan, China earthquake, and suggest that heterogeneities in stress previously inferred from those aftershocks may simply be an artifact of the uncertainties and ambiguities inherent in inferring stress. When the least compressive stress is assumed *a priori* to be steeply dipping, we find that the most and intermediate compressive stresses are roughly E-W and N-S oriented, respectively, consistent with principal directions estimated from coseismic slip in the Wenchuan earthquake.

3.2 Introduction

Earthquake focal mechanisms have been widely used to place constraints on crustal stress (e.g., Gephart and Forsyth, 1984; Michael, 1984, 1987; Hardebeck and Michael, 2006), with the assumptions that one of the nodal planes corresponds to the earthquake slip surface, and that when a fault fails it will slip in the direction of the maximum shear stress resolved on that plane (Wallace, 1951; Bott, 1959; McKenzie, 1969; Angelier, 1979; Célérier, 1988). Abers and Gephart (2001) used P wave first motions to infer stress, in essence combining the inference of the focal mechanism and the stress into one problem; however, more commonly used approaches use predetermined focal mechanisms (e.g., Gephart and Forsyth, 1984; Michael, 1984, 1987; Arnold *et al.*, 2005; Arnold and Townend, 2007; Walsh *et al.*, 2009).

The P, T, and N axes of a focal mechanism represent the principal stress directions of the stress change during the earthquake (e.g., Aki and Richards, 2009). While the directions of the most and least compressive stress directions, MCS and LCS respectively, that led to the earthquake are within the P and T quadrants (McKenzie, 1969), the P, N, and T axes only correspond to the MCS, intermediate compressive stress (ICS), and LCS directions, respectively, of the stress that lead to the earthquake if the fault surface is the plane of maximum shear stress (Gephart and Forsyth, 1984; Shearer, 1999). However, earthquakes large enough for focal mechanisms to be

available are likely to have occurred on pre-existing faults, and thus a large variation of focal mechanisms may be consistent with a given stress (e.g., McKenzie, 1969; Michael, 1984).

The most commonly used algorithms to infer stress from earthquake focal mechanisms are based on least squares inversion techniques (e.g., Michael, 1984, 1987; Gephart and Forsyth, 1984). Stress inferences from multiple focal mechanisms assume either that a single state of stress led to a collection of earthquakes (Angelier, 1979; Michael, 2984), or that stress is constrained to vary smoothly throughout the crust (e.g., Hardebeck and Michael, 2006). It is important to note that in all inversions of stress from focal mechanisms, it is implicitly assumed that the stress is homogeneous in a region at least the size of the rupture dimension. While for a M_w5–6 earthquake this might be a region on order of 10 km^2 or less, for a M_w8 earthquake the fault plane can be several hundred kilometers long. Medina Luna and Hetland (2013) extended the concept of inferring stress from multiple focal mechanisms to finite slip models of large earthquakes, and inferred stress from geodetically constrained models of coseismic slip in the 2008 M_w7.9 Wenchuan, China, earthquake. Conceptually the use of coseismic slip models is similar to the use of slickensides to infer stress (Angelier, 1979).

When inferring stress from a focal mechanism, an ambiguity can arise such that the ICS can be mis-identified as either the MCS or LCS (Célérier, 1988; Arnold and Townend, 2007). Célérier (1988) noted that the ambiguity occurs when the magnitude of the MCS or LCS is similar to the ICS magnitude. Here we show that while the ambiguity is strongest under those conditions, it exists to some extent at all magnitudes of ICS relative to MCS and LCS. The most likely orientation of MCS determined from a single focal mechanism is roughly collinear to the P axis, as shown by McKenzie (1969), but there is a secondary high likelihood orientation of the MCS corresponding to the N axis of the focal mechanism (Célérier, 1988; Arnold

and Townend, 2007). This secondary high likelihood orientation results from the fact that when the MCS lies in the fault plane, fault slip is still possible, but is determined only by the ICS and LCS, and is not readily identified in a least squares solution.

Here we use synthetic pure double-couple focal mechanisms to investigate the extent to which a single earthquake can constrain stress, and the ambiguities that arise in the stress inversion when the fault plane is not optimally oriented in the stress. As the stress is not uniquely constrained by a single focal mechanism (e.g., McKenzie, 1969), we use a Bayesian probabilistic estimation technique, which results in a posterior probability density function (PDF) of the stress, including both principal stress directions and relative magnitudes. We use a Monte Carlo sampling methodology, in which samples of a prior distribution are accepted as samples of the posterior in proportion to the likelihood of the predicted slip rake (e.g., Mosegaard and Tarantola, 1995; Tarantola, 2004). We find that even for optimally oriented faults, the probability of correctly interpreting the posterior estimated from a given earthquake is relatively low, and decreases as the fault orientation becomes more non-optimal. Some researchers have suggested that an assumption of the coefficient of friction can place additional constraints on the stress inversion (e.g., Célérier,1988; Arnold and Townend, 2007). While this mechanical constraint does narrow the range of stress orientations consistent with a focal mechanism, we show that those constraints do not significantly increase the likelihood of the true principal stress orientations.

We then consider focal mechanisms of aftershocks of the 2008 Wenchuan earthquake. The coseismic slip in the Wenchuan earthquake was characterized by largely thrust slip on moderately dipping fault segments in the SW and predominantly right-lateral strike-slip on steeper dipping fault segments in the NE, with all of the segments striking roughly SW-NE (e.g., Nakamura *et al.*, 2010; Shen *et al.*, 2009; Feng *et al.*, 2010; Tong *et al.*, 2010; Qi *et al.*, 2011; Fielding *et al.*, 2013). Wang *et al.*, (2009) and Cai *et al.*, (2011) determined focal mechanisms of the largest aftershocks, finding a

distribution of thrust and strike-slip mechanisms along the entire rupture zone. There is in general spatial clustering of both thrust and strike-slip aftershocks, with clusters of both in the SW and NE of the mainshock rupture trace. When interpreting the stress inferred from aftershocks, it is important to note that the stress immediately after the mainshock, resulting in the aftershocks, may not be the same as the stress immediately before the mainshock (e.g., Bai *et al.*, 2013; Yang *et al.*, 2013).

Due to their disparate mechanisms, the focal mechanisms of aftershocks following the Wenchuan earthquake are a good case study to illustrate the ramifications of the ambiguities in the stress inferences. We postulate that any stress heterogeneity suggested by the aftershocks may be due in part to ambiguities in interpreting the principal stress orientations, as well as poorly constrained relative magnitudes of principal stresses. Although we cannot rule out that the aftershocks reveal localized heterogeneous stresses, we find that the aftershocks are largely consistent with a near homogeneous stress.

3.3 Bayesian Estimation of Stress from Focal Mechanisms

Following our work in Medina Luna and Hetland (2013), we use a Bayesian Monte Carlo (BMC) method to infer stress tensors that are consistent with a focal mechanism. We solve the same problem proposed by Angelier (1979) and Michael (1987) to constrain stress from slickensides on exposed fault surfaces and from earthquake focal mechanisms, respectively. Our Bayesian estimation methodology is similar to that proposed by R. Arnold and coworkers (Arnold *et al.*, 2005; Arnold and Townend, 2007; Walsh *et al.*, 2009), although we follow a Monte Carlo sampling strategy, as explained below. In our stress estimation procedure, we first consider stress inferred from a double couple focal mechanism, and the posterior of the stress consistent with multiple focal mechanisms is then the joint PDF of the posteriors estimated from the individual focal mechanisms. Our estimation methodology is in contrast to the

most common approaches to infer stress from focal mechanisms, which rely on least squares techniques (e.g., Gephart and Forsyth, 1984; Michael, 1984, 1987; Hardebeck and Hauksson, 2001). In Bayesian methods it is crucial to consider the uncertainties on the observables used to constrain the solution (e.g., Mosegaard and Tarantola, 1995; Tarantola, 2004), in our case these uncertainties are on the focal mechanism solutions. While it is well known that focal mechanisms do have uncertainties, they are not fully quantified (e.g., Gephart and Forsyth, 1984; Abers and Gephart, 2001; Arnold and Townend, 2007; Walsh *et al.*, 2009; Duputel *et al.*, 2012; Silwal and Tape, 2014).

We describe focal mechanisms through the nodal plane strike and dip, ϕ_j and θ_j respectively, as well as the fault rake, λ_j, where the subscript $j = 1$ or 2 corresponds to the two nodal planes (Figure 3.1), and we ascribe uncertainties in the focal mechanism through errors on ϕ_j, θ_j, and λ_j. Describing focal mechanisms through the angles of

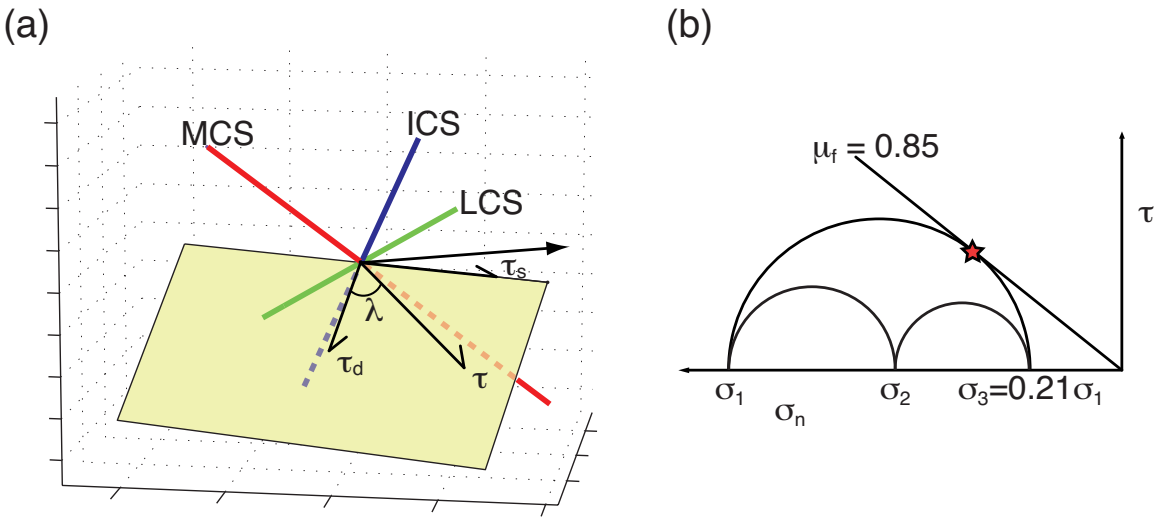

Figure 3.1: Illustration of a planar fault and principal stresses. (a) Shear stresses on a planar fault, shown as hanging-wall arrows, and the principal stress directions: τ_{d} and τ_{s} are shear stresses in the fault dip and strike directions, respectively, τ is the maximum shear stress, and λ is the rake of τ relative to the dip direction; MCS, ICS and LCS are the most, intermediate and least compressive stresses, respectively (modified from Medina Luna and Hetland, 2013). (b) Stress at which an optimally oriented fault will fail at $\mu_f = 0.85$, assuming no intrinsic strength.

the nodal planes ensures that our estimation strategy is directly applicable to other proxies for coseismic slip, including slickenside measurements, as done by Angelier (1979, 1984), and geodetically and/or seismically constrained coseismic slip models, as done by Medina Luna and Hetland (2013). We describe the orientation of the stress tensor through the Euler angles given by the trend and plunge of the MCS, ϕ_{MCS} and θ_{MCS}, respectively, and a rotation of the ICS and LCS about the MCS orientation, ρ_{MCS}. We take the magnitudes of the MCS, ICS, and LCS to be σ_1, σ_2, and σ_3, respectively ($\sigma_1 \leq \sigma_2 \leq \sigma_3 \leq 0$ for compressive stresses). Inversion of stress from focal mechanisms is insensitive to the absolute magnitude of the stress (e.g., Célérier, 1988), and thus all of our inferred stress tensors are relative to an unknown σ_1. We describe the relative magnitudes of the stress tensor through

$$\Delta = \frac{(\sigma_2 - \sigma_3)}{(\sigma_1 - \sigma_3)} \tag{3.1}$$

(e.g., Angelier, 1979; Etchecopar *et al.*, 1981), and

$$R_3 = \frac{\sigma_3}{\sigma_1}. \tag{3.2}$$

Bayesian estimation results in a posterior PDF of the model parameters, m, as a modification of a prior PDF, through the assimilation of constraints (e.g., Mosegaard and Tarantola, 1995; Tarantola, 2004). In our case, m is the tensorial stress that led to a given earthquake scaled by an unknown σ_1, which we describe by $(\phi_{\mathrm{MCS}}, \theta_{\mathrm{MCS}}, \rho_{\mathrm{MCS}}, \Delta, R_3)$, and the constraint is the focal mechanism. We estimate the posterior for each nodal plane independently using a Monte Carlo sampling strategy in which samples of the prior (*i.e.*, trial stresses) are accepted as samples of the posterior in proportion to the likelihood of that stress model (the likelihood function is described below). We then

take the total posterior for a given focal mechanism to be

$$P(m) = P_1(m) \bigcup P_2(m), \tag{3.3}$$

where $P_j(m)$ is the collection of samples of the posterior PDF of the stress on nodal plane j, and $\cup$ indicates the union of samples. Equation (3.3) is simply the union of PDFs of mutually exclusive events (*i.e.*, either of the nodal planes may be the slip surface, but not both). From Bayes theorem, $P_j(m)$ is related to the prior by

$$P_j(m) = k\, L(\hat{\lambda}_j|m)\, p(m), \tag{3.4}$$

where $p(m)$ is a prior PDF, $L(\hat{\lambda}_j|m)$ is the likelihood of the predicted slip rake, $\hat{\lambda}_j$, for a given stress, and k is a normalization constant (e.g., Mosegaard and Tarantola, 1995; Tarantola, 2004). In equation (3.4) we assume k is unknown, and thus $P_j(m)$ only represents the likelihoods of m relative to the most likely estimate (MLE; Tarantola, 2004). We assume that coseismic slip is collinear with the direction of maximum shear stress on the fault (e.g., Wallace, 1951; Bott, 1959; McKenzie, 1969), and we take $\hat{\lambda}_j$ to be the rake of the maximum shear stress on nodal plane j. We calculate the likelihood of $\hat{\lambda}_j$ in a Gaussian sense as

$$L(\hat{\lambda}_j|m) \propto \exp\left\{ -\frac{\angle(\lambda_j, \hat{\lambda}_j)^2}{2\sigma_\lambda^2} \right\}, \tag{3.5}$$

where $\angle(\lambda_j, \hat{\lambda}_j)$ is the angle difference between the predicted and focal mechanism rakes, and σ_λ is the uncertainty of the focal mechanism rake. While our method allows the uncertainty in coseismic slip rakes to differ for each nodal plane, in this paper we assume σ_λ is the same for both nodal planes. In general, it is not true that uncertainty in rake is the same for both nodal planes, for instance rake has been shown to be far less certain for shallowly dipping nodal planes than for steeply

dipping nodal planes (*e.g.*, Zhan *et al.*, 2012).

We consider the simple case where ϕ_j and θ_j are uncorrelated and have Gaussian errors, with standard deviations σ_ϕ and σ_θ. The uncertainty on ϕ is dependent on dip, and is given by $\sigma_\phi = \sigma_\phi^o / \sin(\theta)$, where σ_ϕ^o is the uncertainty of ϕ for a vertical nodal plane. As in the case of the rake uncertainty, the uncertainties on each of the nodal plane geometries could be defined separately, or could be correlated, using either an assumption of Gaussian errors or empirically derived uncertainties (*e.g.*, Zhan *et al.*, 2012). Because our BMC method is based on sampling, it is trivial to incorporate uncertainty of the nodal plane geometries by simply drawing random values of ϕ_j and θ_j from PDFs describing their uncertainties. For simplicity, we assume σ_ϕ and σ_θ for both of the nodal planes are the same.

In most of this study we assume a non-informative prior on the direction of the principal stresses, such that any stress orientation is equally likely. Specifically, we construct the prior on the orientation of the principal stresses assuming ϕ_{MCS} and θ_{MCS} are given by a uniform von Mises-Fisher distribution (Fisher, 1996), while ρ_{MCS} is uniform between $-\pi$ and π. The uniform von Mises-Fisher distribution is simply an even distribution of samples on the unit sphere, where each sample represents the piercing point of the MCS direction. By construction, the MCS, ICS and LCS directions are orthogonal, and thus forming the prior on $(\phi_{\mathrm{MCS}}, \theta_{\mathrm{MCS}}, \rho_{\mathrm{MCS}})$ in this manner is equivalent to assuming that the MCS, ICS, and LCS directions follow a uniform Matrix-Fisher distribution (e.g., Arnold and Townend, 2007).

For the relative magnitudes of the stress, we assume a uniform prior on Δ between 0 and 1, and a uniform prior on R_3 between 0.21 and 1. The end-member cases of $\Delta = 0$ or $\Delta = 1$ correspond to when $\sigma_2 = \sigma_3$ or $\sigma_1 = \sigma_2$, respectively. $R_3 = 1$ corresponds to an isotropic stress, which we discuss below. The lower bound of $R_3 = 0.21$ avoids stress tensors with unreasonably high deviatoric stresses, and corresponds to a stress in which a fault would fail at a coefficient of static friction, μ_f, of 0.85 along an

optimally oriented plane (Figure 3.1). Experiments show that most rocks fail when the fault shear stress, τ, and fault normal stress, σ_n, satisfy a Mohr-Coulomb failure criterion, given by

$$\tau = 0.6\sigma_n + 50 \text{ MPa}, \ |\sigma_n| > 200 \text{ MPa} \tag{3.6}$$

or

$$\tau = 0.85\sigma_n, \ |\sigma_n| < 200 \text{ MPa}, \tag{3.7}$$

(Byerlee, 1978). For simplicity, we assume the low fault normal stress case, which corresponds to $|\sigma_1| < 500$ MPa (Célérier, 1988). Below we show that R_3 is unconstrained by earthquake slip direction, while Δ is only conditionally constrained (the latter was observed by Chiba *et al.* [2012] but not discussed in detail). In our sampling strategy, we randomly select stress models from $p(m)$, and reject/accept these stress models in proportion to equation 3.5.

The upper bound of $R_3 = 1$ corresponds to a fully isotropic stress, which is assumed to be as likely as a non-isotropic stress in $p(m)$. Even if a predicted slip direction is consistent with the focal mechanism rake, a near isotropic stress tensor is only consistent with earthquake slip at vanishingly small μ_f. For a given stress tensor, we define

$$\hat{\mu}_j = \frac{\tau_j}{\sigma_j}, \tag{3.8}$$

where τ_j and σ_j are the maximum shear stress and the normal stress on the j^{th} nodal plane. Assuming that μ_f is the coefficient of static friction of a fault, a stress is consistent with failure in a Mohr-Coulomb sense if $\hat{\mu}_j = \mu_f$, while the stress on the fault will be below the failure envelope if $\hat{\mu}_j < \mu_f$. (If we assume that stress on a given fault can build up past the Mohr-Coulomb failure envelope prior to slipping, then $\hat{\mu}_j \geq \mu_f$.) In our construction of the prior, we guarantee that all model stresses are consistent with slip at $\hat{\mu} < 0.85$. In order to avoid stresses in $P(m)$ that may be inconsistent with Mohr-Coulomb stability, we further constrain the posterior of

stress by rejecting model stresses in which $\hat{\mu}$ is inconsistent with slip at a given Mohr-Coulomb failure criterion. We use $P_\mu(m)$ to indicate all samples that are consistent with both slip in the direction of the focal mechanism rake on one of the nodal planes, and with a given Mohr-Coulomb failure criterion. We accept samples of the posteriors determined from the rake constraint to be samples of $P_\mu(m)$ as long as $\hat{\mu}$ of those stress models is consistent with slip at a given μ_f. For example, if we assume that μ_f is between 0.4 and 0.6, all stresses in $P(m)$ associated with a $\hat{\mu}_j$ between 0.4 and 0.6 are retained as samples of $P_\mu(m)$.

While there are six parameters used as constraints, ϕ_j, θ_j, and λ_j for $j = 1$ and 2, only three of them are independent since we only require the stress to be consistent with slip on one of the nodal planes. Hence, we seek to constrain five model parameters from essentially three constraints, and thus it is an under-determined estimation. In the BMC sampling strategy that we use, the resulting posterior represents all stresses that are consistent with the focal mechanism, possibly with additional constraints on μ_f. Célérier (1988) demonstrated that to better constrain stress using a least squares inversion, at least four focal mechanisms should be used in the stress inversion. As will be shown, if all of the focal mechanisms that contribute to the joint posterior are similar, the joint will not simply be a mirror of each of the individual posteriors, as samples in common regions of high likelihood in the individual posteriors are accepted at a greater rate than samples in low likelihood regions.

If we assume that each focal mechanism is independent, the joint posterior of the stress can be constructed by taking the intersection of samples of the posteriors of each of the focal mechanisms. In other words, stress models that are found to be statistically consistent with slip in all of the focal mechanisms are samples of the joint PDF. In this BMC sampling strategy if the joint is constructed from the common samples in all the constituent posteriors, it is necessary to test the same samples of the prior against each of the focal mechanisms. A Markov Chain based sampling, such

as a Metropolis-Hasting algorithm, would be more computationally efficient (e.g., Mosegaard and Tarantola, 1995). However, using a more direct Monte Carlo uniform sampling allows a greater flexibility in exploration of joint posteriors formed from intersection of samples of individual posteriors. The joint posterior can also be found by accepting samples of the prior proportional to the product of likelihoods of the predicted rakes for each of the focal mechanisms. The two methods of constructing the joint posterior are equivalent.

3.4 Stress Inversion from a Single Focal Mechanism

To illustrate the steps in our BMC estimation strategy, as well as to explore the ability of a single focal mechanism to constrain stress, we consider several synthetic focal mechanisms. All of the synthetic focal mechanisms describe coseismic slip on a fault plane dipping 60° to the east and striking north-south, which we take to be nodal plane 1 (NP1). For a given stress tensor, we calculate the direction of the maximum shear stress on this fault plane, which we assume to be the coseismic slip rake on NP1. We calculate the geometry and slip rake of the auxiliary nodal plane (NP2) assuming that the earthquake is a pure double-couple (e.g., Aki and Richards, 2009). We then estimate the posterior PDF of the stress from that focal mechanism using the BMC strategy outlined above. We assume an uncertainty on slip rake of 5°, although for simplicity in this section we assume no uncertainty on the nodal plane strike or dip.

3.4.1 Synthetic stresses and focal mechanisms

We consider several states of stress, from the ICS trending along the strike of the fault plane, to the ICS out of the fault plane and with either the MCS or LCS trending along the strike of the fault plane (Figures 3.2 and A.1). In the latter cases, the ICS and LCS or MCS and ICS determine the shear stress on the fault

plane. In all cases, we assume that $\sigma_1 = -20$ MPa, $\sigma_2 = -12$ MPa, and $\sigma_3 = -6$ MPa, resulting in $\Delta = 0.43$ and $R_3 = 0.30$. These principal stress magnitudes are consistent with Mohr-Coulomb failure on the fault plane at μ_f between 0.35 and 0.64 for all stress orientations that we consider. In the first stress state, which we refer to as the "reference orientation", the MCS is oriented vertically (30° off of the fault normal), the LCS is horizontal and east-west trending, and the ICS is horizontal and north-south trending (Figure 3.2a). With this stress, the direction of maximum shear stress on the fault plane is consistent with pure-normal slip at $\mu_f = 0.64$. The other stresses result from the progressive rotation of the ICS about the LCS from the reference orientation (Figure 3.2) or MCS (Figure A.1). In the case where the stress is rotated 90° about the LCS (Figure 3.2e), the fault will fail in normal slip at $\mu_f = 0.35$. We then estimate the posteriors from all of these focal mechanisms by testing 5×10^5 samples of the prior, resulting on order 17,000 retained samples of the posteriors (an admittance rate of about 3%).

3.4.2 Principal stress directions

Figure 3.2 shows the marginal posteriors for the orientations of the MCS, ICS and LCS associated with the slip rake on NP1 for three example states of stress. In order to highlight features of the posteriors, we show the marginals of the principal stress directions by the density of samples in approximately equal area bins on the unit sphere. There is a wide range of principal stress orientations that are consistent with the slip rake on NP1 in the posteriors. Any given orientation requires a specific Δ and R_3 in order to have the maximum fault shear stress within the rake direction. We discuss Δ and R_3 in the next section, and for now focus on the principal stress directions. For brevity, we refer to the marginal of the MCS principal stress orientation in the posterior simply as the "MCS posterior", and similarly for ICS and LCS.

In the reference case, the most likely orientation of the MCS and LCS are about

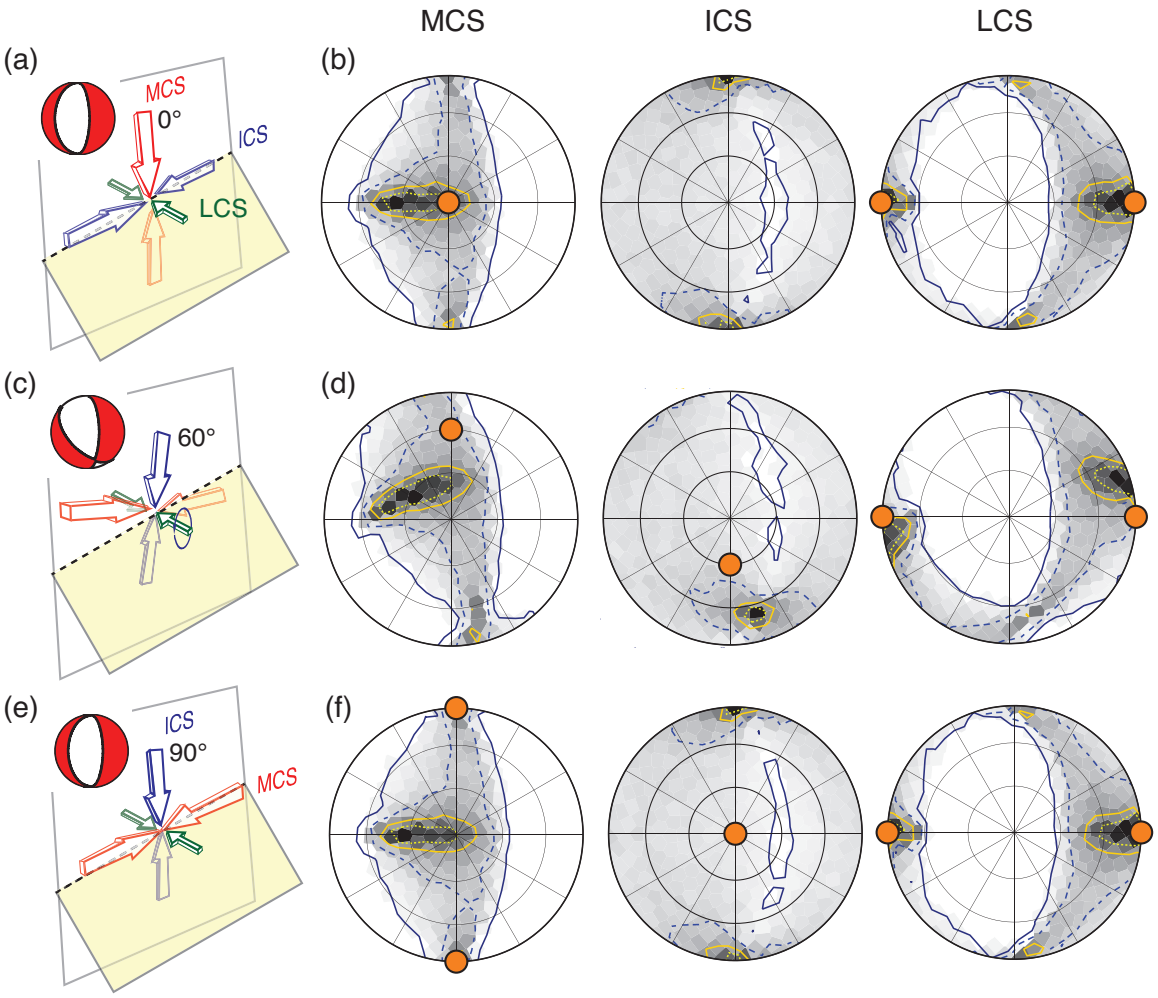

Figure 3.2: Synthetic focal mechanisms and illustrations of the fault plane (shaded plane) and principal stresses (arrows) that led to that synthetic earthquake: (a) is the reference orientation, (c) is the LCS_{60° case, and (e) is the LCS_{90° case. Orientations of the principal stresses (solid dots) associated with the synthetic focal mechanisms in the reference (b), LCS_{60° (d), and LCS_{90° (f) cases, along with the posteriors estimated from the nodal plane corresponding to the fault in the associated synthetic focal mechanisms. Posteriors are shown as probability mass functions in Lambert projections of the lower hemisphere: contours indicate the $0.01p_{\text{MLE}}$ (dark solid line), $0.2p_{\text{MLE}}$ (dark dashed line), $0.5p_{\text{MLE}}$ (solid light line), and $0.75p_{\text{MLE}}$ (light dashed line) levels, where p_{MLE} is the maximum density; shading indicates density of samples in the posterior, with black indicating highest density (*i.e.*, highest likelihood) and white indicating zero density (*i.e.*, no likelihood).

15° off of the true MCS and LCS, with the posteriors showing a broad range of stress orientations with high likelihood (Figure 3.2b). In the case where the ICS and MCS flipped orientation (*i.e.*, with the MCS trending along the strike of the fault

plane and the ICS vertical, which we refer to as the $LCS_{90°}$ case), the posterior of the MCS and LCS orientations are virtually identical to those in the reference case (Figure 3.2b and f). That the posteriors in the two cases are the same is entirely expected, since in both cases the stress is estimated from identical focal mechanisms, and we have not yet considered additional constraints due to an assumption of μ_f. Likewise, when the ICS and LCS flip orientation, the posterior is also the same as that obtained in the reference case (Figure A.1). The posteriors of the ICS have the highest likelihood around the N axis of the focal mechanisms, but have non-negligible likelihood over a large range of orientations. This similarity of the posteriors in the reference and $LCS_{90°}$ cases illustrates the potential ambiguity between either MCS and ICS or ICS and LCS that arises in the estimation of stress from a single focal mechanism. This ambiguity is reflected in the posteriors, where there is a second high likelihood orientation in both the MCS and LCS posteriors corresponding to the N axis of the focal mechanisms.

In the case where the MCS and ICS are rotated 60° about the LCS from the reference orientation (corresponding to oblique fault slip at $\mu = 0.48$, which we refer to as the $LCS_{60°}$ case), the posterior describing the orientation of MCS is rotated away from the reference orientation (Figure 3.2d). However, the highest likelihood region is not rotated to the same extent that the true MCS is rotated, and thus the true MCS lies in a relatively low likelihood region of the posterior (Figure 3.2d). As the MCS rotates, the high likelihood region of the LCS also rotates away from the reference case, even though the true LCS orientation remains the same in the two cases.

3.4.2.1 Probability of correct interpretation

Assuming that we know NP1 is the slip surface, we can estimate the probability of correctly interpreting the posterior PDFs. We do so by taking the fraction of all

of the samples in $P_1(m)$ that are associated with orientations of the principal stresses within 10° of the true orientations that led to the given focal mechanism. Specifically, we divide the number of samples in a spherical cap of arc-distance 10° centered on the true orientations of the principal stress by the total number of samples in the posterior. The probability of correctly interpreting the posterior associated with the reference orientation is only 8–10% for the three principal directions (Figure 3.3). The low probability results from the fact that determination of stress, including both orientation and relative magnitudes, from a single focal mechanism is non-unique. As a result, the marginal posteriors of the orientations are quite broad (Figure 3.2), although in the reference case the likelihood of the true principal stress is well within 75% of the highest likelihood orientation (Figure 3.2).

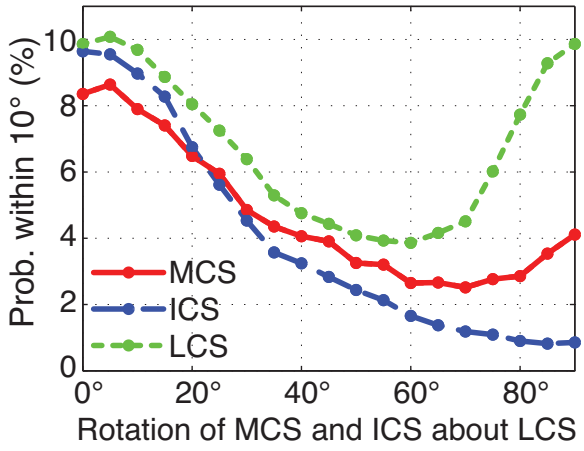

Figure 3.3: Probability of correct stress interpretation, $LCS_{60°}$ case. Posterior probability of MCS, ICS, or LCS orientations within 10° of the true orientations estimated from synthetic focal mechanisms generated by progressively rotating MCS and ICS about the LCS orientation in the reference orientation.

As the ICS rotates out of the fault plane, with either MCS or LCS rotating into the fault plane, the probability of correctly interpreting any of the marginal posteriors of the principal stress orientations decreases (Figures 3.3 and A.2). In the case where the LCS orientation stays fixed, as the MCS rotates into the fault plane, the probability of correctly interpreting the marginal for the LCS orientation increases

back to the same level as in the reference case (Figure 3.3). Likewise, the probability of correctly interpreting the marginal for the MCS increases as the MCS rotates into the fault plane, due to the second high likelihood region corresponding to the focal mechanism N axis in that marginal (Figure 3.3). On the other hand, the probability of correctly interpreting the marginal of the ICS orientation continues to decrease. This behavior is similar when the MCS remains in the original vertical orientation, with the probabilities of correctly interpreting the marginals of the MCS and LCS orientations increasing (Figure A.2).

We have only considered the posteriors associated with the nodal plane corresponding to the actual slip surface. If we were to consider the probabilities of correctly interpreting the total marginal posteriors for a given focal mechanism (*i.e.*, stress that is consistent with the rake on either of the two nodal planes; Figure 3.4), the probabilities would be slightly lower owing to the larger breadth of this total posterior, but the trends would be the same.

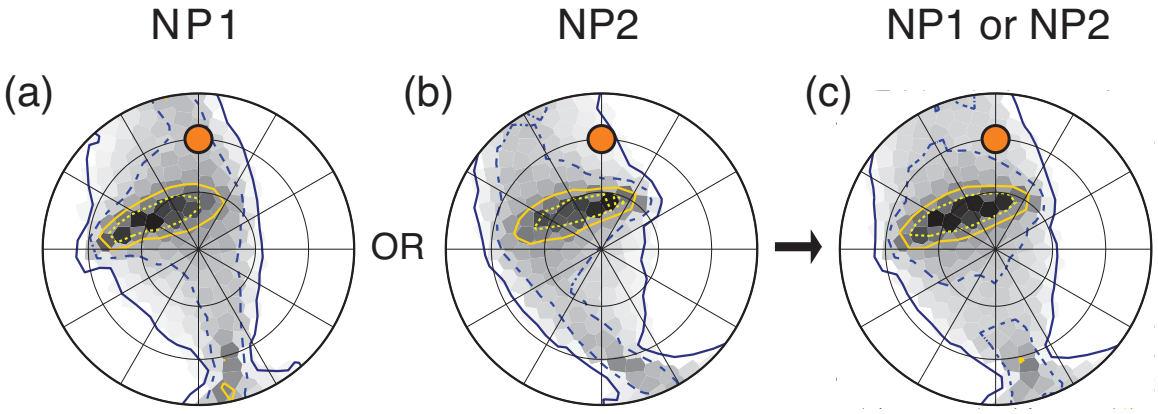

Figure 3.4: Posteriors of MCS orientation estimated from the $LCS_{60°}$ focal mechanism (Figure 3.2b) assuming that NP1 (a) or NP2 (b) corresponds to the fault plane, or that either correspond to the fault plane (c). Contours and shading are as in Figure 3.2, and solid dots are the true orientation of MCS.

3.4.3 Relative stress magnitudes

The marginal posteriors for either Δ or R_3 mirror the marginals in the prior, indicating that slip rake in an earthquake focal mechanism by itself does not constrain these parameters. There is, however, a significant trade-off between Δ and the orientation of principal stresses (e.g., Arnold and Townend, 2007; Chiba *et al.*, 2012). This trade-off is expected, in that if none of the principal stresses are within the fault plane, changing the magnitude of the ICS magnitude relative to the MCS and LCS magnitudes results in a change in the direction of the maximum shear stress on the fault plane. Specifically, for low Δ, the marginal posterior of the MCS orientation becomes more compact, as the less likely orientations in the original posterior become unlikely (Figure 3.5a). The second high likelihood orientation corresponding to the N axis also disappears at low Δ. As Δ increases, the marginal posterior of MCS orientation becomes more diffuse, as the more likely orientations in the original posterior become less likely (Figure 3.5). As Δ increases, the likelihood that the MCS is oriented along the N axis of the focal mechanism also increases relative to the likelihood of any other orientation (Figure 3.5d). The opposite behavior is seen in the marginal posterior of the LCS orientation, with the posterior becoming more compact as Δ increases (Figure A.3). Constraints on Δ have negligible effect on the marginal posterior of ICS orientation (Figure A.4). As the prior assumption of Δ is narrowed closer to the true value, the probability of correctly interpreting the posterior increases. For instance, in the LCS_{60° case when Δ is constrained *a priori* to be between 0.25 and 0.50 (containing the true $\Delta = 0.43$), the probability of correctly interpreting the MCS marginals is about 4.8% compared to less than 1.5% when Δ is assumed to be either < 0.25 or > 0.75.

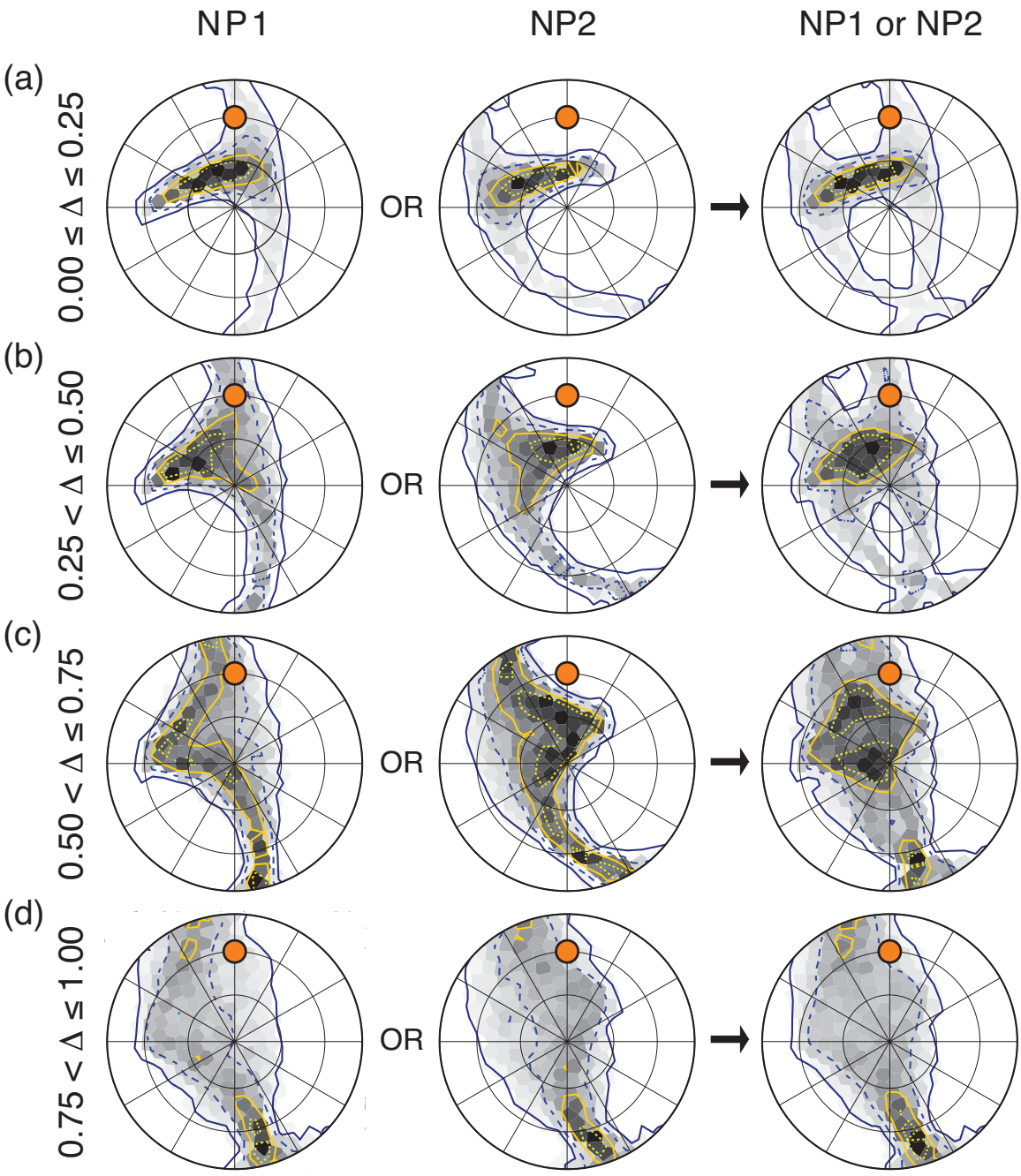

Figure 3.5: Posteriors of MCS orientation estimated from the LCS_{60° case, assuming restricted priors on Δ (rows) and that NP1 (left panels), NP2 (center panels), or either (right panels) corresponds to the fault plane. Priors on Δ are that Δ is equally likely within the ranges $[0.00, 0.25]$ (a), $[0.25, 0.50]$ (b), $[0.50, 0.75]$ (c), or $[0.75, 1.00]$ (d). Contours and shading are as in Figure 3.2, and solid dots are the true orientation of MCS. Figures A.3 and A.4 show the associated posteriors of the ICS and LCS orientations, respectively.

3.4.4 Application of the mechanical constraint

While all stress models in the posteriors produce a maximum shear stress direction that is statistically consistent with the focal mechanism slip rake, many of the models are mechanically inconsistent with fault slip in a Mohr-Coulomb frictional sense. As discussed above, we allow stresses that are near isotropic in $p(m)$, in which the shear stress on the fault is vanishingly small. A prior assumption on μ_f can further narrow the posteriors by rejecting stresses that are inconsistent with Mohr-Coulomb failure. That μ_f can further constrain the stress consistent with focal mechanisms has previously been suggested (e.g., Reches, 1987; Célérier, 1988), with results from Reches (1987) arguing the importance of incorporating a fault friction condition for realistic fault failure examples; however, such a mechanical constraint is not routinely applied.

In a Mohr-Coulomb frictional sense, a given stress will be at failure when $\hat{\mu}_j = \mu_f$ on either NP1 ($j = 1$) or NP2 ($j = 2$). We limit the posterior to those stresses that are mechanically consistent with prior assumptions on μ_f, by rejecting model stresses with $\hat{\mu}_j$ outside of an assumed range of μ_f, as described above. Narrowing prior assumptions on μ_f results in narrowing the range of stresses that are consistent with slip on each nodal plane. We show the marginal posteriors of MCS orientation for $P_\mu(m)$ for the LCS_{60° case in Figure 3.6. In the stress that generated this synthetic focal mechanism, slip on NP1 is consistent with Mohr-Coulomb failure as $\mu_f = 0.48$. We consider two ranges of μ_f, either between 0.2 and 0.4 or between 0.4 and 0.6. In the mechanically constrained marginals associated with NP1, the true MCS orientation does not correspond to the highest likelihood orientation (Figure 3.6). On the other hand, the true MCS orientation is unlikely in the mechanically constrained posterior associated with NP2 (Figure 3.6b). Hence, if μ_f was *a priori* known, it might be possible to resolve which nodal plane corresponds to the slip surface. However, the probability of correctly identifying the true stress orientation would still be relatively

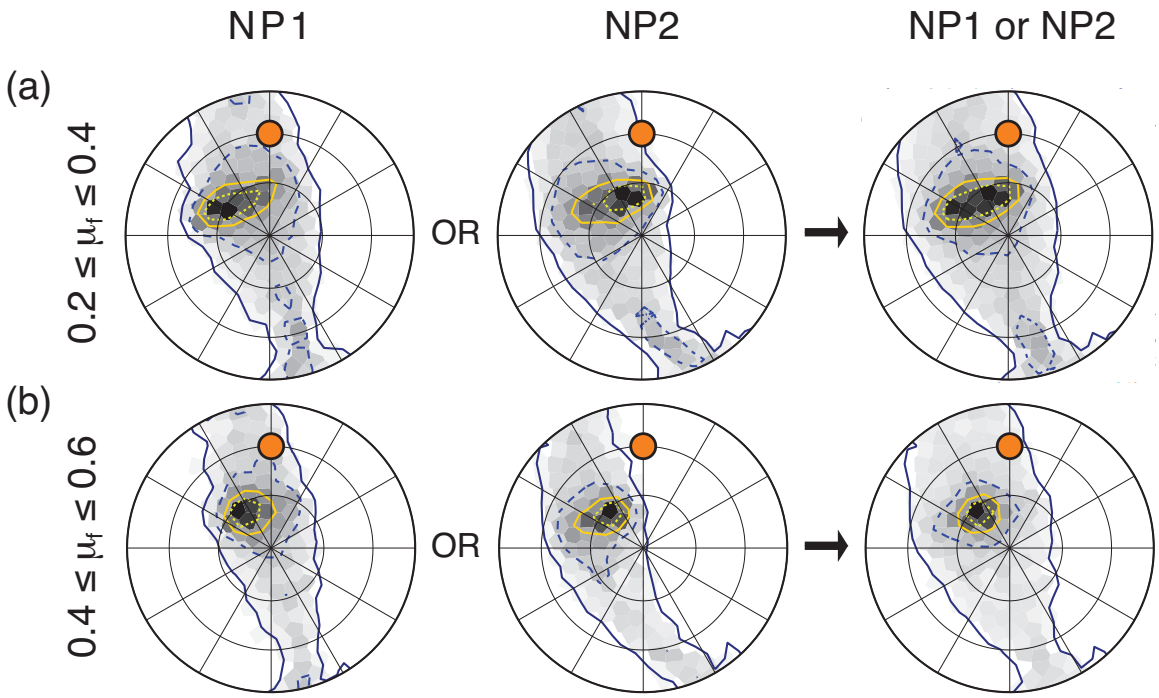

Figure 3.6: Posteriors of MCS orientation estimated from the LCS_{60° case, assuming priors on μ_f (rows) and that NP1 (left panels), NP2 (center panels), or either (right panels) correspond to the fault plane. Priors on μ_f are such that μ_f is equally likely with the ranges $[0.2, 0.4]$ (a) or $[0.4, 0.6]$ (b). Contours and shading is as in Figure 3.2, and solid dots are the true orientation of MCS.

low for the case when the fault was not optimally oriented in a given stress.

As briefly discussed previously, a focal mechanism by itself does not constrain R_3 (Figure 3.7a), and there are no trade-offs between R_3 and any other parameters describing the stress tensor. However, when a mechanical constraint on μ_f is incorporated, the permissible R_3 is narrowed substantially (Figure 3.7b and c). For instance, in the LCS_{60° case, when the prior of μ_f is narrowed and encompasses the actual $\mu_f = 0.48$, the highest likelihood of R_3 in $P_\mu(m)$ corresponds to the true value (Figure 3.7c). Constraining μ_f also results in narrowing Δ in the posterior (Figure 3.7e), which follows from the trade-off between Δ and the stress orientations. However, the most likely Δ in $P_\mu(m)$ in the LCS_{60° case does not correspond to the true $\Delta = 0.43$ (Figure 3.7f), which is due to the fact that the most likely orientation of

principal stresses are not the true orientations even after the mechanical constraint is considered (Figure 3.6b).

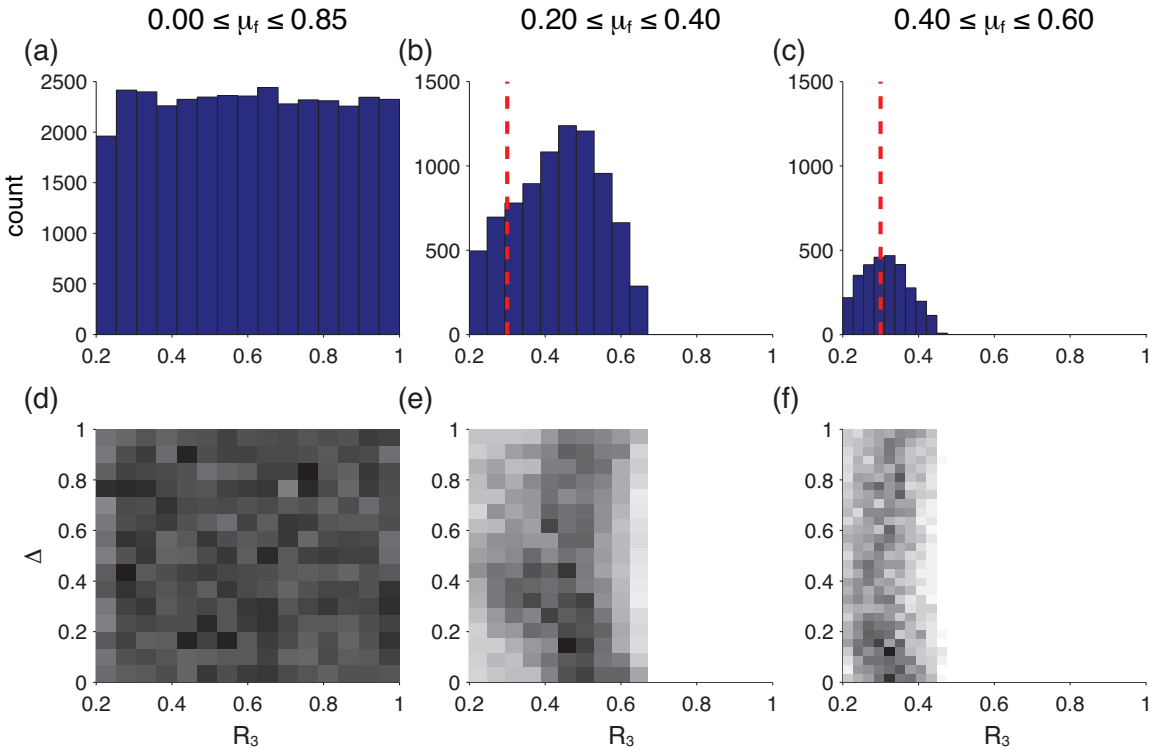

Figure 3.7: (a)–(c) Marginals of R_3 and Δ of the posterior estimated from the LCS_{60° case, assuming different priors on μ_f. Dashed lines indicate the true value of R_3 and grey shading in (d)–(f) indicates relative density of posterior samples.

3.4.5 Estimated stress from multiple focal mechanisms

We have thus far only considered the extent to which stress can be inferred from a single focal mechanism. It is commonly accepted that using a diverse collection of focal mechanisms results in a more robust stress inference (e.g., Célérier, 1988; Abers and Gephart, 2001; Hardebeck and Hauksson, 2001; Arnold and Townend, 2007). Within our BMC estimation, samples of the joint posterior of stress consistent with multiple focal mechanisms are found by taking the intersection of all samples in each of the posteriors from the individual focal mechanisms. We test the same samples of the prior against each of the focal mechanisms, so the intersection of the individual

posteriors reflects the collection of model stresses that are statistically likely for all of the focal mechanisms.

Based on our consideration of a posterior estimated from a single focal mechanism, we can make three observations that are pertinent to applying this technique to multiple focal mechanisms. The first is that as more focal mechanisms contribute to the joint posterior, a larger number of samples of the prior should be tested using this BMC strategy. This results from the fact that as more constraints are imposed, the admittance rate of the prior samples will decrease. The second is that if all of the focal mechanisms are similar, the joint posterior is not simply a mirror of the individual posteriors, as overlapping regions of high likelihood in the individual posteriors result in higher likelihood in the joint posterior relative to overlapping regions of lower likelihood in the individual posteriors. The third is that a single focal mechanism that is quite different from the rest of the focal mechanisms will result in a significant narrowing of the likely stresses in the joint posterior (Arnold and Townend, 2007). In the extreme case, if the posterior of one focal mechanism is disjoint from the rest, then it will yield the solution of a single stress tensor jointly consistent with all of the focal mechanisms. While the single stress model, which is the least squares solution as we assume Gaussian likelihood functions, is the solution to the BMC estimation, it may not be a geophysically reasonable stress.

3.5 Application to Wenchuan aftershocks

We estimate stress from focal mechanisms of 82 aftershocks of the 2008 Wenchuan earthquake with M_w greater than 4.0 determined by Cai *et al.* (2011; Figure 3.8). An uncertainty of 15° is assumed on the focal mechanism slip rake, and strikes and dips of all of the nodal planes. We group most of the aftershocks into five groups, each containing at least nine focal mechanisms. The groups are chosen based on epicentral proximity, as well as on the similarity of the MCS and LCS posteriors of

the individual focal mechanisms. There were ten aftershocks that did not fit into one of these groups, which we address in the Discussion section. Grouping based on the similarity of MCS and LCS posteriors is roughly equivalent to grouping based on the overlap of the compressional and tensional quadrants of focal mechanisms, although comparing the posteriors is more robust as not all regions of the focal quadrants are associated with a high likelihood of stress.

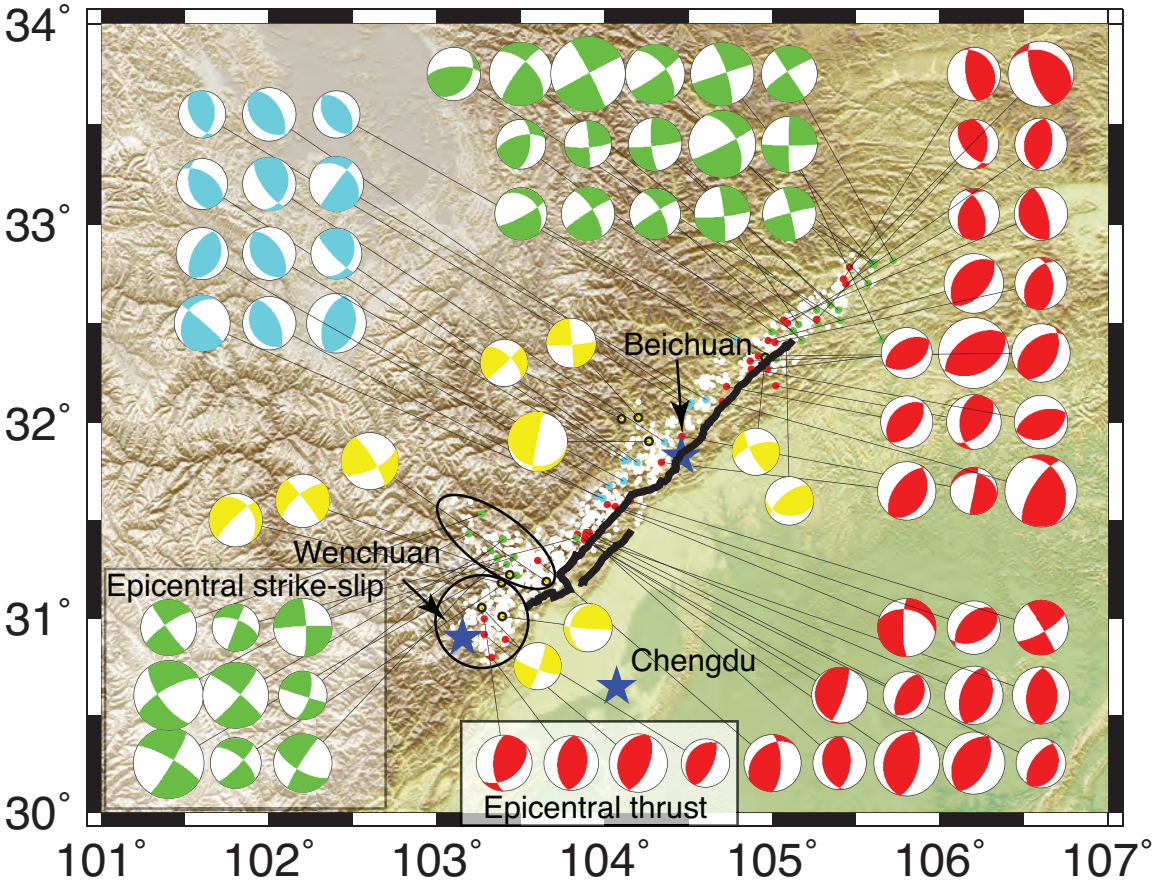

Figure 3.8: Map of Wenchuan earthquake rupture and aftershock focal mechanisms. Surface trace of the Wenchuan earthquake (black lines; Feng *et al.*, 2010), focal mechanisms of 82 relocated aftershocks (Cai *et al.*, 2011), and aftershocks (white dots; Huang *et al.*, 2008; Xu *et al.*, 2009). Stars indicate the locations of Chengdu, Wenchuan, and Beichuan cities. Focal mechanisms in which estimated posteriors are consistent with each other are presented in this chapter and are colored red (SW and NE reverse groups), green (SW and NE strike-slip groups), and cyan (transitional group). Other focal mechanisms are colored yellow. Topography from Jarvis *et al.*, (2006).

In the following subsections, we first estimate stress from 13 thrust aftershocks in the epicentral region (we use "epicentral region" to broadly refer to the south-western section of the fault trace). Second, we estimate stress from nine strike-slip aftershocks also in the epicentral region (Figure 3.8). Third, we use a restricted prior to illustrate how ambiguities in the interpretation of the posteriors estimated from different mechanisms of aftershocks may result in interpretation of a highly heterogeneous stress field. Fourth, we determine stress from all five groups of aftershocks using the restricted prior. Fifth, we explore the similarities and differences of the joint posteriors estimated from the five groups.

3.5.1 Epicentral thrust aftershocks

Stress estimated from the thrust aftershocks in the epicentral region is relatively well constrained, with a high likelihood of a WNW-ESE trending sub-horizontal MCS, a largely NNE-SSW trending, sub-horizontal ICS and a near-vertical LCS (Figure 3.9a). As discussed above, even though the focal mechanisms contributing to the joint posterior are all similar, the joint posterior is not simply a mirror of the individual posteriors determined from each focal mechanism independently (Figure A.5). When the posterior is constrained by limiting Δ to be greater than 0.5, the permissible trends of the MCS and ICS orientations broaden, while their plunge remains sub-horizontal (Figure 3.9c). However, the joint posterior includes a more E-W trending MCS when $\Delta \geq 0.5$ (Figure 3.9c). We also note that the mainshock may have changed the stress field near the fault. Therefore, the stresses that led to the mainshock and these aftershocks need not be the same. For $\Delta < 0.5$, there is a slight likelihood that LCS could be off of vertical (Figure 3.9b), although with $\Delta > 0.5$ these LCS orientations are impossible and the posterior favors a near-vertical LCS orientation. Regardless of Δ, this group of thrust aftershocks tends to favor orientations of MCS and ICS that are rotated clockwise from the results of Medina Luna and Hetland

(2013; Figure 3.10) and Styron and Hetland (in review).

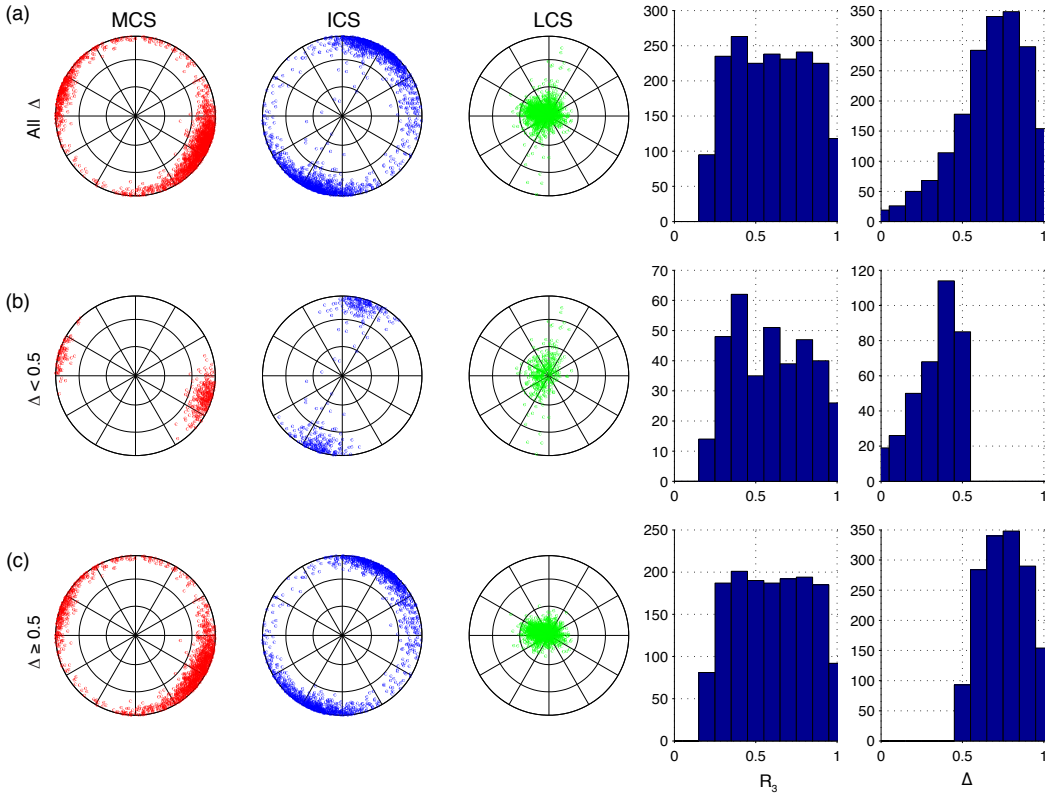

Figure 3.9: Principal stress orientations estimated from thrust aftershocks in the epicentral region (Figure 3.8), assuming that either nodal plane corresponds to the slip surface. Posteriors plotted as points on the lower hemisphere with high density of points indicating high likelihood. Histograms indicate the corresponding R_3 and Δ.

3.5.2 Epicentral strike-slip aftershocks

Several aftershocks in the epicentral region were almost pure strike-slip (Wang *et al.*, 2009; Cai *et al.*, 2011). These aftershocks are located along a lineament of the NW-SE striking Xiaoyudong fracture zone (Wang *et al.*, 2009; Cai *et al.*, 2011; Deng *et al.*, 2011), extending to the NW and trending roughly perpendicular to the main-shock epicentral region (Figure 3.8). The majority of these strike-slip aftershocks are

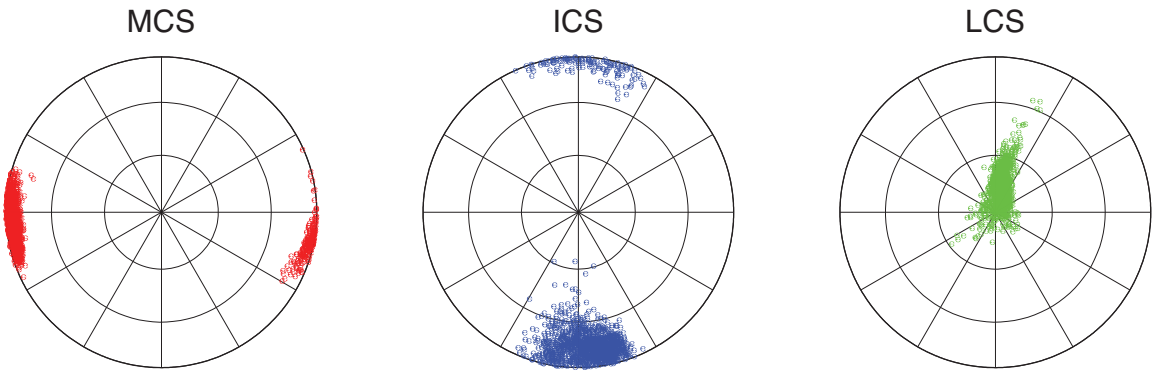

Figure 3.10: MCS, ICS, and LCS orientations consistent with coseismic slip models of the Wenchuan earthquake (modified from Medina Luna and Hetland, 2013).

farther from the mainshock than the epicentral thrust earthquakes discussed above. At these farther distances, the stress changes due to the mainshock coseismic slip are expected to be smaller, and thus the stress posterior inferred from these aftershocks is more likely to represent the pre-mainshock stress than the posterior of the thrust aftershocks closer to the mainshock. The likely MCS orientations inferred from these aftershocks tends to be more SW-NE trending than the MCS orientation inferred from the nearby thrust earthquakes (Figures 3.9 and 3.11a). The likely ICS and LCS orientations from these strike-slip aftershocks are inconsistent with those inferred from the nearby thrust aftershocks (Figure 3.9), as well as those inferred from coseismic slip in the mainshock (Figure 3.10; Medina Luna and Hetland, 2013; Styron and Hetland, in review). The highest concentration of ICS orientations in the samples of the joint posterior of the strike-slip aftershocks roughly correspond to the LCS orientations inferred from the thrust aftershocks, while the LCS orientations from the strike-slip events fall within the uncertainty of the ICS orientations from the thrust events (*cf.*, Figures 3.9c and 3.11a). The ambiguity in interpretation of the principal stresses from these strike-slip aftershocks is most apparent in MCS and ICS directions, where there is a significant likelihood that MCS is vertical.

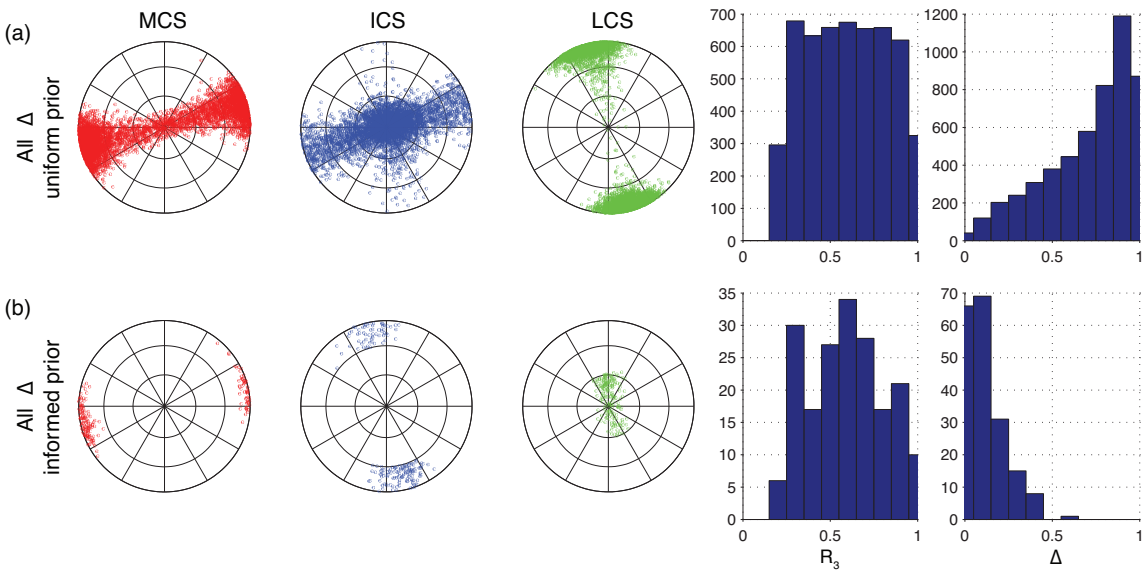

Figure 3.11: (a) Principal stress orientations estimated from the strike-slip aftershocks in the epicentral region (Figure 3.8), assuming that either nodal plane corresponds to the slip surface and the non-informative prior. (b) Posteriors estimated assuming the restricted prior in which the LCS orientation is steeply dipping (Figure A.6) and $\Delta \geq 0.5$. Posteriors plotted as points on the lower hemisphere with high density of points indicating high likelihood. Histograms indicate the corresponding R_3 and Δ.

3.5.3 Restricted prior

To explore the effect of the ambiguity in uniquely resolving principal stresses from these posteriors, we propose an informed prior, which we refer to as the "restricted prior" in which the LCS is steeply dipping to vertical. We assume that dip of the MCS is within $\pm 45°$ of horizontal and that $-30° \leq \rho_{\text{MCS}} \leq +30°$, which together ensures that the LCS is at most about 50° from vertical (Figure A.6). We note that the near-vertical LCS orientations inferred from the thrust aftershocks is roughly along the nodal planes of the strike-slip aftershocks. As demonstrated with the synthetic focal mechanisms, when the true LCS direction is along the fault plane, an ambiguity arises in the interpretation of principal directions as either the LCS or ICS. In the restricted prior, we keep Δ and R_3 the same as in the non-informative prior. Even though the MCS and ICS orientations were least constrained with epicentral strike-

slip aftershocks using a prior with no constraint on orientations, using the restricted prior there are a range of solutions in which both MCS and ICS are subhorizontal (Figure 3.11b).

3.5.4 Estimated stress from the Wenchuan aftershocks

We estimate stress posteriors from the five groups of aftershocks using the restricted prior in which LCS is constrained to be near-vertical (Figure 3.12). The epicentral groups considered in sections 3.5.1 and 3.5.2 are extended to incorporate a broader region, which we refer to as the southwest strike slip and southwest reverse groups. We refer to the groups as strike slip and reverse since they consist predominantly of those types of focal mechanisms, but also incorporate a few oblique focal mechanisms (Figure 3.8). We similarly construct northeast strike slip and reverse groups (Figures 3.8 and 3.12). The fifth group we consider is a transitional group, composed of several oblique to reverse focal mechanisms distributed along the central region of the mainshock, NE of the surface trace (Figures 3.8 and 3.12).

The MCS orientations in the joint posteriors using the restricted prior are all similar, albeit more broadly distributed, to the MCS orientation in the joint posterior using the original non-informative prior. The ICS and LCS orientations in the joint posteriors for the groups dominated by thrust mechanism aftershocks are similar to the non-informative and restricted priors. However, the ICS and LCS orientations are flipped in the joint posteriors for the strike-slip group using either the non-informative or restricted priors. The MCS and ICS orientations in three of the five groups (SW strike-slip, transitional, and NE reverse) are within the uncertainty of those inferred from coseismic slip in the mainshock (Figure 3.10; Medina Luna and Hetland, 2013; Styron and Hetland, in review). In contrast, the SW reverse and the NE strike slip group of aftershocks tend to favor a slightly more NW-SE trending MCS compared to the more WSW-ENE trending MCS favored by aftershocks to the NW (Figure 3.12).

The mean MCS and ICS stress orientations estimated from the SW reverse and NE strike-slip groups are rotated about 38° from the mean orientations estimated from the other groups (Table 3.1). Similarly, the SW reverse and NE strike-slip aftershocks tend to favor ICS orientations trending NE-SW, while the other groups tend to favor ICS orientations trending more N-S to NNW-SSE (Figure 3.12).

		MCS	ICS
SW reverse	$\phi(^\circ)$	296.1 ± 12.4	26.2 ± 12.6
NE strike slip	$\phi(^\circ)$	304.2 ± 8.4	36.3 ± 9.1
SW strike slip	$\phi(^\circ)$	258.2 ± 10.8	347.6 ± 11.5
Transitional	$\phi(^\circ)$	262.6 ± 16.5	352.5 ± 16.5
NE reverse	$\phi(^\circ)$	260.9 ± 17.7	351.0 ± 17.6

Table 3.1: Orientation of mean and standard deviation of the principal stresses in the joint posteriors estimated from five groups of Wenchuan aftershocks (Figure 3.12). Trend (ϕ) of the MCS are in the Aki and Richards (2009) convention, with 0° due north.

The principal stress orientations in the joint posteriors of the SW reverse and NE strike slip groups are quite similar, although Δ in the joint posteriors is not entirely overlapping (Figure 3.12). As a result of the relatively complimentary Δ in the stress models in the two joint posteriors, we find only one stress sample is jointly consistent with all of the focal mechanisms in the SW reverse and NE strike slip groups. We note that when forming these joints, we tested 8 million prior stress samples, in which LCS is constrained to be near vertical (Figure A.6), against all of the aftershocks. Due to the large density of prior samples, we do not feel that the fact that only one stress model was found to be consistent with these aftershocks is a result of being under sampled, but rather that the joint posterior does indeed have negligible to no variances (*i.e.*, the joint posterior is close to, or is a delta function). The trend of the MCS in this joint posterior is similar to the mean MCS trends in the joint posteriors of the SW reverse and NW strike slip groups, and likewise for the ICS (Tables 3.1 and 3.2). $\Delta = 0.26$ in the stress model found as the singular sample of the joint posterior.

		MCS	ICS	Δ
SW reverse & NE strike-slip	$\phi(^\circ)$	297.7	29.4	0.3
SW strike-slip & NE reverse & Transitional	$\phi(^\circ)$	62.7	331.1	0.5
All Groups	$\phi(^\circ)$	280.7	11.4	0.2

Table 3.2: Orientation of mean and standard deviation of the principal stresses in the joint posterior estimated by combining groups of aftershocks of Wenchuan aftershocks (Figure 3.12). Trend (ϕ) of the MCS and ICS are in the Aki and Richards (2009) convention, with 0° due north.

The principal stress orientations in the joint posteriors of the SW strike slip, transitional, and NE reverse aftershock groups are all broadly consistent, although the inferred Δ is not (Figure 3.12). In general, the aftershock groups dominated by reverse mechanisms are most consistent with Δ above 0.5, while the aftershock groups dominated by strike slip mechanisms are most consistent with Δ below 0.5. Similar to above, the joint posterior of the aftershocks in the SW strike slip, transitional, and NE reverse groups is composed of a single stress model. The orientations of the principal stresses of this stress model are consistent with the mean principal stress orientations in the joint posteriors of the constituent groups (Tables 3.1 and 3.2). $\Delta = 0.49$ in the sample of the joint posterior of the aftershocks in these three groups. We likewise find one stress model that is consistent with all of the aftershock focal mechanisms (excluding the 10 focal mechanisms that we do not include in the initial five groups, which are discussed below). The principal stress orientations of this stress model are roughly the average of the principal stress orientations of the stress models found to be consistent with the two larger groups of aftershocks (Table 3.2), while $\Delta = 0.19$.

3.6 Discussion

3.6.1 BMC inference of stress from focal mechanisms

Using a single focal mechanism, estimation of the stress that led to that earthquake is non-unique. We account for this non-uniqueness by casting the estimation in a Bayesian framework, wherein the posterior includes all stresses that are consistent with the slip rake on one of the nodal planes. The highest likelihood stress in the posterior estimated from one focal mechanism is such that the MCS, ICS, and LCS are collinear with the P, N, and T axes of the focal mechanism. In essence, the posterior states that in absence of any information other than the coseismic slip rake, the most likely solution is the simplest solution, which is a near optimal stress for a given fault plane. Also included in the posterior are what we refer to as perfectly non-optimal stresses, where either the MCS or LCS are collinear with the N axis, while the ICS is collinear with the P or T axes. With a non-informative prior on Δ (*i.e.*, $0 \leq \Delta \leq 1$ are all equally likely *a priori*), these perfectly non-optimal stresses have relatively high likelihood, although they are not as likely as optimal stresses. The posterior additionally encompasses a range of non-optimal stresses, in which none of the principal stresses corresponding to the principal axes of the focal mechanism.

In the non-optimal stresses, a specific Δ is required to produce the direction of maximum shear stress consistent with the slip rake (Figure 3.5), whereas when one of the principal stresses is in the fault plane, a much wider range of Δ are all consistent with the same rake. For example, if the MCS is in the fault plane, and faulting was determined purely by ICS and LCS, as in the LCS_{90° example (Figure 3.2e), variation in Δ will not result in a different predicted rake, but rather would only affect τ or σ_n. When none of the principal stresses are in the fault plane, variations in Δ result in changes to the predicted rake, as well as changes in τ and σ_n.

Several studies that seek to infer stress from focal mechanisms assume at least

one of the principal stresses is vertical (e.g., Zoback and Zoback, 1980; Michael, 1984; Hauksson, 1994; Hardebeck and Michael, 2006; Célérier, 2012). In the case of the Wenchuan aftershocks, we assumed *a priori* that LCS was near vertical, although our prior also includes steeply dipping LCS orientations. Several studies also fix the relative magnitudes *a priori* (e.g., Hauksson, 1994; Hardebeck and Hauksson, 2006; Medina Luna and Hetland, 2013). Fixing one of the principal stress directions removes potential ambiguities in the stress inversion. Even though relative magnitudes of stress are only weakly constrained by focal mechanisms alone, there are strong trade-offs between Δ and the orientations of principal stresses. Hence assuming Δ *a priori*, or an equivalent description of the ICS magnitude relative to the MCS and LCS magnitudes, can introduce biases in the inferred stress.

Even with multiple focal mechanisms, the estimation of stress may not be strictly unique. If all of the focal mechanisms are similar, then the joint posterior will be more compact than the individual posteriors. This is because mutually high likelihood stresses become more likely relative to mutually low likelihood stresses. If the focal mechanisms vary, then the joint posterior are the stresses that are common to all of the individual posteriors. Regardless of how large the variation in focal mechanisms is, least squares based techniques to estimate stress from focal mechanisms by design yield the most likely estimate of stress without quantifying the statistical likelihood of that stress. For multiple focal mechanisms, the least squares solution is the average of the optimal stresses of the constituent focal mechanisms. In our BMC estimation strategy, when only a single stress model is found to be consistent with multiple focal mechanisms, that stress model is the least squares solution.

Reches (1987) emphasized the importance of considering fault friction when inferring stress from focal mechanisms, and argued that stress inversion techniques can implicitly assume near zero friction when friction is ignored. Placing a mechanical constraint for fault failure on either of the two nodal planes narrows the posterior

PDF of stress. If the true μ_f on the fault was known *a priori*, it might be possible to resolve which of the two nodal planes is the slip surface, since a prior on μ_f narrows $P_j(m)$ for each of the nodal planes distinctly. Priors on μ_f also strongly affect permissible R_3, and if μ_f was known in a probabilistic sense, the relative magnitudes of stress could be further constrained. In our non-optimal LCS_{60° case, assuming a prior on μ_f which encompassed the actual value of the synthetic slip surface, R_3 was narrowed appreciably with the highest likelihood R_3 in $P_\mu(m)$ corresponding to the true R_3 in the synthetic stress. However, the highest likelihood of Δ in $P_\mu(m)$ did not correspond with the true Δ, largely due to the fact that the highest likelihood principal stress orientations in $P_\mu(m)$ do not correspond to the true orientations.

Abers and Gephart (2001) proposed a method to infer stress directly from P-wave first arrivals, thereby including the estimation of the focal mechanism as a part of the inference of stress. This approach to estimation of stress is attractive, as the uncertainties of the primary observations, the P-wave first arrivals, are used directly to estimate the uncertainty on the inferred stress. Many techniques for determining focal mechanisms use more of the seismic wave-field than the first arrivals, yielding a better constrained focal mechanism (e.g., Dziewonski et al., 1981; Sipkin, 1982; Hayes et al., 2009). In these instances, it is easier to infer stress directly from the focal mechanisms. When inferring stress directly from pre-determined focal mechanisms, it is necessary to quantify the uncertainty on those focal mechanisms in order to quantify the uncertainty in the inferred stress; however, the error on a focal mechanism is not well quantified (e.g., Abers and Gephart, 2001; Walsh et al., 2009; Duputel et al., 2012; Valentine and Trampert, 2012; Zhan et al., 2012). It is important to note that the uncertainties on focal mechanisms parameters are not equal and the uncertainties on many of the parameters are correlated (e.g., Zhan et al., 2012). In their Bayesian estimation strategy, Arnold and Townend (2007) incorporated a precision parameter in a Matrix-Fisher PDF of Euler angles to represent the error

of the focal mechanism. Arnold and Townend (2007) justify the use of a precision parameter since focal mechanism uncertainty is often represented as a scalar quantity. By using a scalar to encompass the focal mechanism error, the associated error on ϕ_j, θ_j, and λ_j are equal and uncorrelated, although using their methodology correlations could be accounted for. In our BMC estimation we include the focal mechanism uncertainties to the nodal plane strike, dip, and rake. As in Arnold and Townend (2007), we also did not account for any correlation between ϕ_j and θ_j, although it would be trivial to include that in the scheme we propose. Accounting for correlations between λ_j and the nodal plane geometry is also possible in the BMC scheme we propose, as would using empirically derived uncertainties and correlations on the focal mechanism solution.

3.6.2 Stress inferred from Wenchuan aftershocks

Aftershock focal mechanisms following the Wenchuan earthquake have previously been used to infer the stress along the trace of the Wenchuan earthquake, both qualitatively (Cai *et al.*, 2011) and quantitatively (Wang *et al.*, 2009). The qualitative interpretation of Cai *et al.*, (2011) was simply based on the diversity of orientations of the P axes of the aftershock focal mechanisms, which the authors concluded suggested a heterogeneous stress orientation along the Wenchuan earthquake trace. Using the FMSI method of Gephart and Forsyth (1984), Wang *et al.* (2009) also favored an interpretation that the aftershocks suggested a heterogeneous stress. In both of the studies, the preferred heterogeneous stress orientations do not vary smoothly along the fault trace. Wang *et al.* (2009) argued that the stress in the SW, near the epicenter, was dominantly in a strike-slip sense, with near east-west oriented MCS, similar to our conclusions from these aftershocks. Wang *et al.* (2009) also argued the stress in the NE was dominated by MCS oriented roughly normal to the fault trace, although the mainshock rupture was predominantly strike-slip in that region. As earthquakes

can occur on pre-existing planes of weakness, the apparent heterogeneity based on the aftershock focal mechanisms may reflect a transition of the slip onto various fractures within a region consistent with a homogeneous state of stress (Gephart and Forsyth, 1984). Additionally, Wang *et al.* (2009) remarked that all of the aftershocks were consistent with a homogeneous state of stress within the uncertainties of the P-wave first arrival picks.

In a previous study we found that several geodetically constrained coseismic slip models of the Wenchuan earthquake were consistent with a uniform orientation of stress (Medina Luna and Hetland, 2013). In that study, we used a Bayesian Monte Carlo estimation very similar to that proposed here, and found that the most likely orientations of the MCS were sub-horizontal, and trending roughly E-W, with orientations up to about $\pm 20^{\circ}$ from E-W permissible in the 95% credible interval (Figure 3.10). We also found permissible in ICS orientations were sub-horizontal and trending roughly NNE-SSW, and LCS orientations near-vertical (Figure 3.10). In that study we concluded that the magnitude of the ICS was most likely about 30% of the magnitude of the MCS, although it should be noted that there may have been some biases in the posterior introduced in the manner in which we constructed the prior in that previous study. That prior was constructed based on σ_2/σ_1 and σ_3/σ_2, and not Δ and R_3, as done here. We have found that priors based on Δ and R_3 yield more robust posteriors, and the majority of least squares based stress inversion methods also parameterize the relative stress magnitudes with Δ (e.g., Angelier, 1979; Etchecopar *et al.*, 1981; Michael, 1984, 1987).

Aftershocks result from both the pre-mainshock stress and the stress changes during the mainshock (e.g., King *et al.*, 1994; Hardebeck and Hauksson, 2001; Hasegawa *et al.*, 2011; Bai *et al.*, 2013; Yang *et al.*, 2013). For the most part, the coseismic stress changes predicted from geodetically constrained slip models of the Wenchuan earthquake are negligible (much less than 1 MPa) except very close to large gradients

in coseismic slip on the faults, where predicted stress changes can be several MPa to nearly 15 MPa. Although all of the coseismic slip models broadly agree, they all have appreciable differences in the details (*e.g.*, Nakamura *et al.*, 2009; Feng *et al.*, 2010; Qi *et al.*, 2011). These differences arise from differences in the data considered, as well as the regularization applied in the inversion and possibly assumed geometry of the fault model. Differences in the gradients of slip in the inferred coseismic slip models will result in differences in the near-field coseismic stress changes. Additionally, knowing precise locations of the near-field aftershocks relative to the mainshock coseismic slip distribution is crucial for accurately calculating the coseismic stress changes due to the mainshock (Bai *et al.*, 2013).

The MCS orientations inferred from all but ten of the aftershock focal mechanisms are broadly consistent with that inferred from geodetically constrained models of coseismic slip during the mainshock (Medina Luna and Hetland, 2013; Styron and Hetland, in review) when the LCS is constrained as vertical (Figure 3.12). The joint posterior of the SW strike slip, the transitional, and NE reverse aftershock groups are most similar to the stresses inferred from the mainshock (Figures 3.10 and 3.12).

At the southwest and northeast extent of the Wenchuan rupture, most likely principal stress orientations are rotated nearly 40° clockwise from the principal stress orientations inferred from the other three aftershock groups (Figure 3.12, Table 3.1). Note that these aftershock groups spatially overlap and thus we do not believe the rotation in principal stresses indicates along-strike stress heterogeneity. The inferred orientations of the MCS in the five joint posteriors overlap at the 95% credible interval (Table 3.1). However, Δ does not overlap between the five joint posteriors (Figure 3.12). We favor the simpler interpretation of a near homogeneous stress along the strike of the Wenchuan earthquake with MCS subhorizontal and trending WNW-ESE (about 10° off of E-W), well within the 95% credible interval of MCS inferred from the mainshock (Figure 3.10; Medina Luna and Hetland, 2013).

Ten aftershocks were not included in the joint stress posteriors (Figure 3.8). Many of these aftershocks are located fairly close to the main fault rupture, and might be strongly influenced by the stress changes during the mainshock. For instance, the coseismic slip model of Feng *et al.*, (2010) predicts a most compressive stress change of nearly -15 MPa, comparable to inferred earthquake stress drops (e.g., Kanamori and Anderson, 1975; Shearer *et al.*, 2006), at a strike-slip aftershock located near the Wenchuan epicenter and at 15 km depth. This strike-slip aftershock is at a depth where the resolution of the coseismic slip in geodetically constrained models is poor. Interestingly, the individual posteriors of the 10 aftershocks are largely consistent with each other. A joint posterior of these ten aftershocks, distributed along the trace of the Wenchuan earthquake, is characterized by a roughly N-S trending MCS and E-W trending ICS, with near vertical LCS. However, we can not see any compelling reason why there may be an ambiguity in inferred stress orientations estimated from these aftershocks, as was appealed to for the other strike-slip aftershocks. In order to quantify the relationship of these aftershocks to the regional stress field, consideration of the mainshock stress changes is required. For a complete assessment including all aftershock focal mechanisms, a probabilistic model of the coseismic stress changes at the hypocentral locations of the aftershocks from a variety of coseismic slip models is required, and is beyond the scope of this paper. For a such an assessment, knowing precise hypo central location of the aftershocks, or quantification of the uncertainty in hypocenter, is required (e.g. *Bai et al.*, 2014). Furthermore, consideration of other local factors that might likely cause a localized re-orientation of stress may also be required, for instance topographically induced stresses (e.g., Styron and Hetland, 2014).

3.7 Conclusions

We present a Bayesian Monte Carlo (BMC) method for inferring the stress that led to a given earthquake from the focal mechanism solution of that earthquake, resulting in samples of a posterior PDF of stress consistent with the focal mechanism. Our methodology relies on the assumption that one of the nodal planes corresponds to the slip surface and that fault slip is collinear with the direction of maximum shear stress accumulated on that fault. A further constraint is placed on the posterior by selecting stresses consistent with Mohr-Coulomb failure under an assumed fault friction, μ_f. Using synthetic focal mechanisms consistent with known stresses, we show that the probability of correctly interpreting a posterior is relatively low, and decreases significantly when none of the principal stresses are within the fault plane. Additionally, there is a potential for the principal stresses to be mis-identified in the posteriors estimated from focal mechanisms when intermediate compressive stress is farther than about 20° from the focal mechanism N axis. A mechanical constraint through an assumption of μ_f narrows the stress posterior, but does not uniquely resolve the stress. Assumptions of μ_f have the potential to resolve which of the two nodal planes corresponds to the slip surface.

Using this BMC estimation strategy, we infer stress from a diverse set of focal mechanisms of aftershocks of the 2008 Wenchuan, China earthquake. The Wenchuan aftershocks varied from strike-slip to reverse along the faults that slipped in the Wenchuan mainshock, and have been used to argue that the stress in the region is heterogeneous (Wang *et al.*, 2009; Cai *et al.*, 2011). We suggest that these apparent heterogeneities are simply an artifact of the inability to correctly interpret the principal stresses inferred from focal mechanisms. We find that the MCS direction inferred from the majority of the aftershock focal mechanisms are consistent when the LCS is assumed to be steeply dipping. These principal stress orientations are also consistent with the stress inferred from coseismic slip models of the Wenchuan mainshock (*e.g.*,

Medina Luna and Hetland, 2013; Styron and Hetland, 2014). From these aftershocks, it is most likely that the MCS is near horizontal, and trending WNW-ESE (rotated about 10° from E-W), with ∼N-S trending ICS and near vertical LCS. Aftershocks that are not consistent with the stresses inferred from the mainshock favor ∼N-S trending MCS and ∼E-W trending ICS, with near vertical LCS. A full stress inversion that includes the coseismic slip, and associated stress changes, in the mainshock and the aftershocks will provide further insights into the evolution of stress during the Wenchuan earthquake and its aftershock sequence. However, such an analysis should account for uncertainties in the Wenchuan earthquake coseismic slip models, as well as in the aftershock focal mechanisms and hypocentral locations.

3.8 Data and Resources

Aftershock focal mechanism data used for this study were received through personal communication with the authors of the published article from Cai et al., (2011), listed in the references.

3.9 Acknowledgments

We thank the Rackham Graduate School, University of Michigan, for a Rackham Merit Fellowship to L. Medina Luna. Matlab (The Mathworks, Inc.) was used for all calculations and to generate all figures presented in this paper.

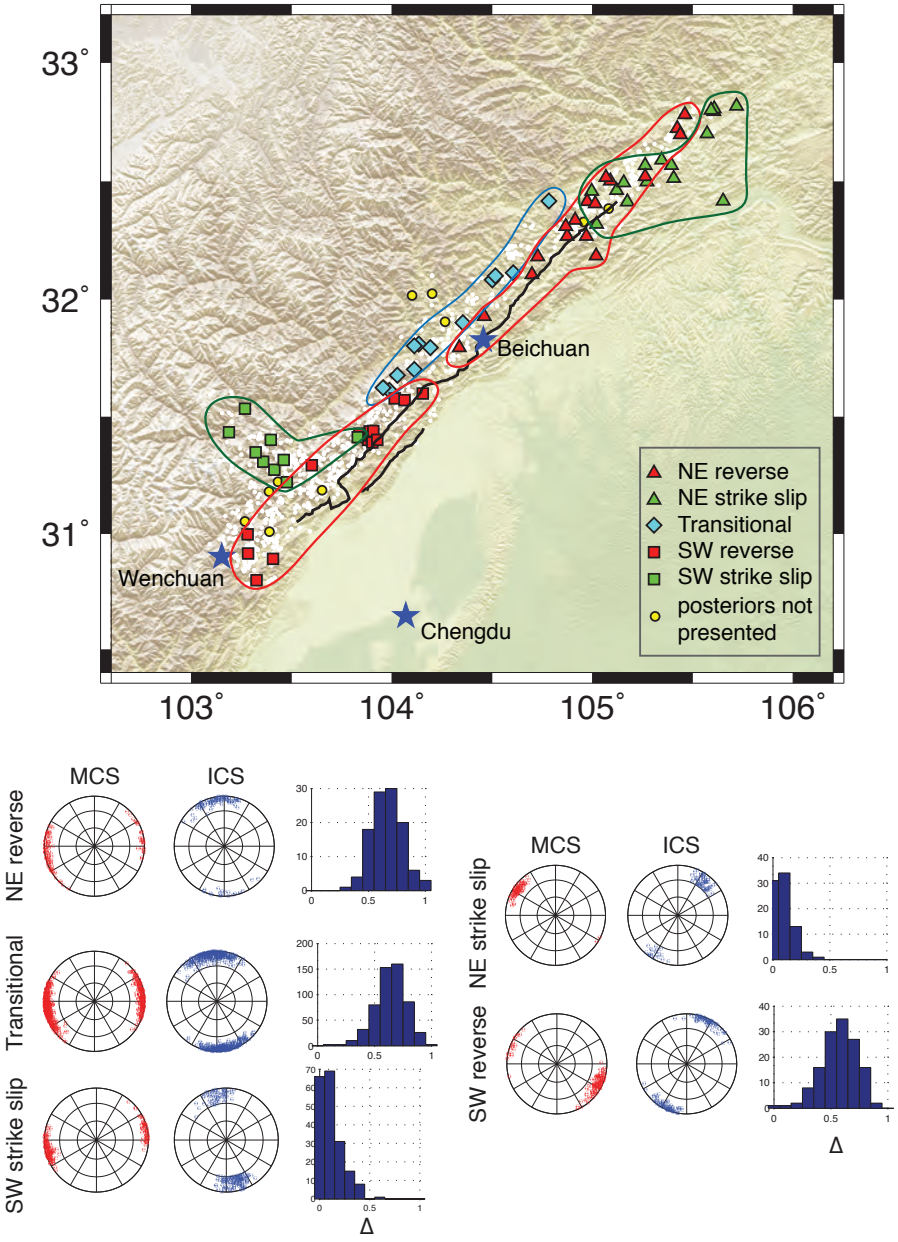

Figure 3.12: MCS and ICS orientations and Δ estimated from groups of aftershocks assuming the restricted prior in Figure A.6. Epicenters of the Wenchuan aftershocks in each group are outlined, and the trace of the Wenchuan earthquakes from Feng *et al.* (2010; black solid lines). Mean and standard deviations in Tables 3.1 and 3.2. Topography from Jarvis *et al.*, (2006).

3.10 References

Abers, G. A., and Gephart, J. W., (2001). Direct inversion of earthquake first motions for both the stress tensor and focal mechanisms and application to southern California. J. Geophys. Res., **106**, no. B11, 26,523-26,540, doi: 10.1029/2001JB000437.

Aki, K., and Richards., P. G. Quantitative Seismology, 2nd Edition. Sausalito: University Science Books, 2009. Print.

Angelier, J., (1979). Determination of the mean principal directions of stresses for a given fault population. Tectonophysics **56**, T17T26, doi: 10.1016/0040-1951(79)90081-7.

Angelier, J., (1984). Tectonic analysis of fault slip data sets. J. Geophys. Res., V. 89, B7, 5835-5848. doi: 10.1029/JB089iB07p05835

Angelier, J., (1989). From orientation to magnitudes in paleostress determinations using fault slip data. J. Struct. Geol., **11**, No. 1-2, 37-50, doi: 10.1016/0191-8141(89)90034-5.

Angelier, J., Tarantola, A., Valette, B., Manoussis, S., (1982). Inversion of field data in fault tectonics to obtain the regional stress- I. Single phase fault populations: a new method of computing the stress tensor. Geophys. J. R. ast. Soc., **69**, 607-621. doi:: 10.1111/j.1365-246X.1982.tb02766.x.

Arnold, R., Townend, J., and Vignaux, T., (2005). Mapping tectonic stress using earthquakes. AIP Conf. Proc. 803, 475; doi: 10.1063/1.2149828.

Arnold, R., and J. Townend, (2007). A Bayesian approach to estimating tectonic stress from seismological data. Geophys J. Int., **170**, 1336-1356. doi: 10.1111/j.1365-246X.2007.03485.x.

Bai, L., Medina Luna, L., Hetland, E. A., Ritsema, J. R., (2014). Focal mechanisms of Tohoku-Oki aftershocks from tele seismic P wave modeling. Earthq. Sci., **27**, 1-13, doi: 10.1007/s11589-013-0036-x.

Bott, M. H. P., (1959). The mechanics of oblique slip faulting. Geological Magazine, **96**, Issue 2, 109-117. doi: 10.1017/S0016756800059987.

Byerlee, J., (1978). Friction of rocks. Pure. Appl. Geophys., **116**, Issue 4-5, 615-626.

Cai, C., Yu, C., Tao, K., Hu, X., Tian, Y., Zhang, H., Cui, X., Ning, J., (2011). Spatial distribution and focal mechanism solutions of the Wenchuan earthquake series: results and implications. Earthquake Science, **24**, 115125, doi: 10.1007/s11589-011-0775-5.

Célérier, B., (1988). How much does slip on a reactivated fault plane constrain the stress tensor? Tectonics, **7**, no. 6, 1257-1278.

Chiba, K., Iio, Y., and Fukahata, Y., (2012). Detailed stress fields in the focal region of the 2011 off the Pacific coast of Tohoku EarthquakeImplication for the distribution of moment release. Earth Planets Space, **64**, no. 12, 1157-1165, doi: 10.5047/eps.2012.07.008.

Deng, Q., Chen, G., and Zhu, A., (2011). Discussion of rupture mechanisms on the seismogenic fault of the 2008 Ms8.0 Wenchuan earthquake, Earth Sciences, **54**, no. 9, 1360-1377, doi: 10.1007/s11430-011-4230-1.

Duputel, Z., Rivera, L., Fukahata, Y., Kanamori, H., (2012). Uncertainty estimations for seismic source inversions. Geophys. J. Int., **190**(2), 1243-1256, doi: 10.1111/j.1365-246X.2012.05554.x.

Dziewonski, A., Chou, T., and Woodhouse, J., (1981), Determination of Earthquake Source Parameters From Waveform Data for Studies of Global and Regional Seismicity: J. Geophys. Res., **86**, 2825-2852.

Etchecopar, A., Vasseur, G., and Daignieres, M., (1981). An inverse problem in micro tectonics for the determination of stress tensors from fault striation analysis. J. Structural Geology, **3**, no. 1, 51-65.

Feng, G., Hetland, E., Ding, X., Li, Z., Zhang, L., (2010). Coseismic fault slip of the 2008 Mw 7.9 Wenchuan earthquake estimated from InSAR and GPS measure-

ments. J. Geophys. Res., **37**, L01302. doi:10.1029/2009GL041213.

Fielding., E.J., Sladen, A., Li, Z., Avouac, J.P., Brgmann, R., Ryder, I., (2013). Kinematic fault slip evolution source models of the 2008 M7.9 Wenchuan earthquake in China from SAR interferometry, GPS and teleseismic analysis and implications for Longmen Shan tectonics. Geophys. J. Int., **194**(2), 1138-1166. doi: 10.1093/gji/ggt155.

Fisher, N., (1996). Statistical Analysis of Circular Data. Cambridge University Press, New York, NY, USA.

Gephart, J., and Forsyth, D., (1984). An improved method for determining the regional stress tensor using earthquake focal mechanism data: Application to the San Fernando earthquake sequence. J. Geophys. Res., **89**, 9305-9320, doi: 10.1029/JB089iB11p09305.

Hardebeck, J. L., and Hauksson, E., (2001). Crustal stress field in southern California and its implications for fault mechanics. J. Geophys. Res., **106**, No. B10, 21,859-21,882, doi: 10.1029/2001JB000292.

Hardebeck, J., and Hauksson, E., (2002). A new method for determining first-motion focal mechanisms. Bull. Seism. Soc. Am., **92**, No. 6, 2264-2276, doi: 10.1785/0120010200.

Hardebeck, J. L., and Michael, A. J., (2006). Damped regional-scale stress inversions: Methodology and examples for southern California and the Coalinga aftershock sequence. J. Geophys. Res., **111**, B11310, doi:10.1029/2005JB004144.

Hasegawa, A., Yoshida, K., and Okada, T., (2011). Nearly complete stress drop in the 2011 Mw 9.0 off the Pacific coast of Tohoku Earthquake. Earth Planets Space, **63**, 703-707, doi: 10.5047/eps.2011.06.007.

Hauksson, E., (1994). State of stress from focal mechanisms before and after the 1992 Landers earthquake sequence. Bull. Seism. Soc. Am., **84**, No. 3, 917-734.

Hayes, G., Rivera, L., Kanamori, H., (2009). Source Inversion of the W-Phase: Real-

time Implementation and Extension to Low Magnitudes, Seismol. Res. Lett., **80**, 817-822, doi: 10.1785/gssrl.80.5.817.

Huang, Y., Wu, J., Zhang, T., Zhang, D., (2008). Relocation of the M8.0 Wenchuan earthquake and its aftershock sequence. Sci. China Ser D-Earth Sci., **51**, p. 17031711.

Jarvis A., H.I. Reuter, A. Nelson, E. Guevara, (2006). Hole-filled seamless SRTM data V3, International Centre for Tropical Agriculture (CIAT), available from http://srtm.csi.cgiar.org.

Kanamori, H., and Anderson D.L., 1975. Theoretical basis of some empirical relations in seismology. Bull. Seism. Soc. Am., **65**, No. 5, 1073-1095.

King, G. C. P., Stein, R. S., and Lin, J., (1994). Static stress changes and the triggering of earthquakes. Bull. Seism. Soc. Am., **84**, No. 3, 935-953.

McKenzie, D. P., (1969). The relation between fault plane solutions for earthquakes and the directions of the principal stresses. Bull. Seism. Soc. Am., **59**, No. 2, 591-601.

Medina Luna, L., and Hetland, E. A., (2013). Regional stresses inferred from co-seismic slip models of the 2008 Mw 7.9 Wenchuan, China, earthquake. Tectonophysics, **584**, 43-53, doi: 10.1016/j.tecto.2012.03.027.

Michael, A. J., (1984). Determination of stress from slip data: faults and folds. J. Geophys. Res., **89**, B13, 11,517-11,526, doi: 10.1029/JB089iB13p11517.

Michael, A. J., (1987). Use of focal mechanisms to determine stress: a control study. J. Geophys. Res., **92**, B1, 357-368. doi: 10.1029/JB092iB01p00357.

Mosegaard, K., Tarantola, A., (1995). Monte Carlo sampling solutions to inverse problems. J. Geophys. Res., **100**, 12,43112, 447.

Nakamura, T., Tsuboi, S., Kaneda, Y., Yamanaka, Y., (2010). Rupture process of the 2008 Wenchuan, China earthquake inferred from teleseismic waveform inversion and forward modeling of broadband seismic waves. Tectonophysics, **491**, 72-84,

doi: 10.1016/j.tecto.2009.09.020.

Qi, W., Xuejun, Q., Qigui, L., Freymueller, J., Shaomin, Y., Cijun, X., Yonglin, Y., Xinzhao, Y., Kai, T., Gang, C., (2011). Rupture of deep faults in the 208 Wenchuan earthquake and uplift of the Longmen Shan. Nat. Geosci., **4**, 634-640. doi: 10.1038/NGEO1210.

Reches, Z., (1987). Determination of the tectonic stress tensor from slip along faults that obey the Coulomb yield condition. Tectonics, **6**, No. 6, 849-861. doi: 10.1029/TC006i006p00849.

Shearer, P. M., (1999) Introduction to Seismology. New York: Cambridge University Press. Print.

Shearer, P. M., Prieto, G. A., and Hauksson, E., (2006). Comprehensive analysis of earthquake source spectra in southern California, J. Geophys. Res., **111**, BO6303, doi:10.1029/2005JB003979.

Shen, Z. K., Sun, J., Zhang, P., Wan, Y., Wang, M., Brgmann, R., Zeng, Y., Gan, W., Liao, H., Wang, Q., (2009). Slip maxima at fault junctions and rupturing of barriers during the 2008 Wenchuan earthquake. Nat. Geosci., **2**, 718-724, doi: 10.1038/ngeo636.

Silwal, V., and Tape, C., (2014). Seismic moment tensors in southern Alaska derived from body waves and surface waves. In Seismological Society of America Meeting Abstracts.

Sipkin, S., (1982), Estimation of earthquake source parameters by the inversion of waveform data: synthetic waveforms. Phys. Earth Planet. In., **30**, 242-259.

Styron, R., and Hetland, E. A., (in review). The weight of the mountains: Constraints on tectonic stress, friction, and fluid pressure in the 2008 Wenchuan earthquake from estimates of topographic loading. Submitted to J. Geophy. Res.

Tarantola, A., (2004). Inverse Problem Theory and Methods for Model Parameter Estimation. SIAM, Philadelphia.

Tong, X., D. Sandwell, and Y. Fialko, (2010). Coseismic slip model of the 2008 Wenchuan earthquake derived from joint inversion of interferometric synthetic aperture radar, GPS, and field data, J. Geophys. Res., **115**, B04314, doi: 10.1029/2009JB006625, 2010.

Valentine, A. and Trampert, J., (2012). Assessing the uncertainties on seismic source parameters: Towards realistic error estimates for centroid-moment-tensor determinations. Phys. Earth Planet. In., **210-211**, 36-49, dpi: 10.1016/j.pepi.2012.08.003.

Wallace, R., (1951). Geometry of shearing stress and relation to faulting. J. Geol., **59**, No. 2, 118-130.

Walsh, D., (2008). Directional statistics, Bayesian methods of earthquake focal mechanism estimation, and their application to New Zealand seismicity data. Masters thesis, Victoria University of Wellington, New Zealand.

Walsh, D., Arnold, R., and Townend, J., (2009). A Bayesian approach to determining and parametrizing earthquake focal mechanisms. Geophys. J. Int., **176**, 235-255. doi:10.1111/j.1365-246X.2008.03979.x

Wang., Q. C., Chen, Z. L., and Zheng, S. H., (2009). Spatial segmentation characteristic of focal mechanism of aftershock sequence of Wenchuan Earthquake. Chinese Sci. Bull., **54**, 2263-2270, doi: 10.1007/s11434-009-0367-0.

Xu, X., Wen, X., Yu, G., Chen, G., Klinger, Y., Hubbard, J., Shaw, J., (2009). Coseismic reverse-and oblique-slip surface faulting generated by the 2008 Mw7.9 Wenchuan earthquake, China. Geology **37**, p. 515518, doi:10.1130/G25462A.1.

Yang, Y. R., Johnson, K. M., and Chuang, R. Y., (2013). Inversion for absolute deviatoric crustal stress using focal mechanisms and coseismic stress changes: The 2011 M9 Tohoku-oki, Japan, earthquake. J. Geophys. Res.: Solid Earth, **118**(10), 5516-5529.

Zhan, Z., Helmberger, D., Simons, M., Kanamori, H., Wu, W., Cubas, N., Duputel, Z., Chu, R., Tsai, V. C., Avouac, J. P., Hudnut, K. W., Ni, S., Hetland, E.,

Culaciati, F. H. O., (2012). Anomalously steep dips of earthquakes in the 2011 Tohoku-Oki source region and possible explanations. Earth Planet Sci. Lett., **353-354**, 121-133.

Zoback, M. L., and Zoback, M., (1980). State of stress in the conterminous United States. J. Geophys. Res., **85**, No. B11, 6113-6156.

CHAPTER 4

State of stress along the westernmost North Anatolian fault inferred from coseismic slip models and focal mechanisms

4.1 Abstract

The westernmost North Anatolian fault (NAF) within the Sea of Marmara has not ruptured in recent history, and poses an ongoing hazard for the city of Istanbul, Turkey. To investigate the state of stress along the NAF near Istanbul, we estimate stress from earthquake slip data using a Bayesian Monte Carlo probabilistic estimation technique. We consider coseismic slip models of the 1999 İzmit and Düzce earthquakes and focal mechanisms of earthquakes along the Main Marmara Fault (MMF) in the Sea of Marmara. We find that the stress that led to the İzmit-Düzce earthquake sequence is largely homogeneous, with a NW-SE trending subhorizontal MCS, vertical ICS, and subhorizontal LCS trending NE-SW. We find a variation of stress along the MMF, with subhorizontal MCS trending near N-S on the Çinarcik segment and trending MCS closer to E-W along the western segment.

This chapter is in preparation for submission.

4.2 Introduction

In 1999, two earthquakes with M_w >7.0 occurred within a 90 day time period on the North Anatolian Fault (NAF) in eastern Turkey, and east of the Sea of Marmara: the August 17, 1999 M_w 7.4 İzmit, Turkey earthquake, and the November 12, 1999 M_w 7.2 Düzce, Turkey earthquake. Coseismic slip in the İzmit earthquake was predominantly strike slip on fault segments with near vertical dip (Reilinger *et al.*, 2000; King *et al.*, 2001; Barka *et al.*, 2002; Delouis *et al.*, 2002). The earthquake propagated under the Sea of Marmara, and thus its western extent is not well determined (Bulut *et al.*, 2009; Pinar *et al.*, 2001, 2010). The slip in the Düzce earthquake consisted of predominantly dextral slip with a component of normal slip on north-dipping fault segments (Ayhan *et al.*, 2001; Bürgmann *et al.*, 2002; Cakir *et al.*, 2003; Konca *et al.*, 2010). These earthquakes were the latest in a sequence of earthquakes along the NAF, starting with the 1939 M_w 7.8 Erzincan earthquake (*e.g.*, Barka, 1996; Stein *et al.*, 1997; Ayhan *et al.*, 2001; Şengör *et al.*, 2005). Models of stress changes from the mainshock indicate stress loading on fault segments to the east and west of the rupture (Parsons, *et al.* 2000; King *et al.* 2001). Stress loading on fault segments to the west of the İzmit rupture into the Sea of Marmara may indicate potential for future rupture along a seismic gap of the NAF that poses a seismic hazard to the city of İstanbul (e.g., Stein *et al.*, 1997; Parsons *et al.*, 2000; Hubert-Ferrari *et al.*, 2000; King *et al.*, 2001; Le Pichon *et al.*, 2003; Şengör *et al.*, 2005).

In this study, we use both geodetically constrained coseismic slip models of the İzmit and Düzce earthquakes and focal mechanisms of small earthquakes in the Sea of Marmara to investigate the stress along the NAF, including the region of the İzmit and Düzce earthquakes and into the Sea of Marmara. Previous studies inferred stress from aftershocks of the İzmit-Düzce earthquake sequence (Bohnhoff *et al.*, 2006; Görgün et al, 2010; Pinar *et al.*, 2010, Örgülü, 2011; Ickrath et al, 2014), using the methods of Gephart and Forsyth (1984) and Michael (1984, 1987). It is

not our goal to reproduce these studies, rather we focus on the stress that led to the İzmit-Düzce earthquake sequence using geodetically constrained coseismic slip models. Additionally, we re-examine the stress in the Sea of Marmara region. We consider three geodetically constrained coseismic slip models of the İzmit earthquake (Reilinger *et al.*, 2000; Delouis *et al.*, 2002; Çakir, 2004) and two coseismic slip models of the Düzce earthquake (Çakir *et al.*, 2003a; Delouis *et al.*, 2004). We consider focal mechanisms determined for earthquakes in the Sea of Marmara both prior to and following the İzmit earthquake, determined by Ergin *et al.*, (1997), Kiratzi (2002), Pinar *et al.*, (2003), Bulut *et al.*, (2009), and Örgülü (2011) (Figure 4.1). We use the Bayesian Monte Carlo probabilistic estimation technique, which we developed in Medina Luna and Hetland (2013, in prep; Chapters 2 and 3). This technique is similar to the methods developed by R. Arnold and coworkers (Arnold *et al.*, 2005; Arnold and Townend, 2007; Walsh *et al.*, 2009).

4.3 Methods

We use a Bayesian Monte Carlo (BMC) probabilistic estimation technique to infer stress from coseismic slip models and focal mechanisms, discussed in Chapters 2 and 3. Unlike least squares methods, (Gephart and Forsyth, 1984; Michael, 1984, 1987; Hardebeck and Hauksson, 2001), our BMC estimation results in a posterior probability density function (PDF) of stresses consistent with slip in the coseismic slip models and focal mechanism nodal planes. We assume that coseismic slip is coincident with the maximum shear stress on a slip surface (Wallace, 1951; Bott, 1959; McKenzie, 1969; Angelier, 1979), and allow for uncertainty in slip rake as described below.

We seek to determine a model of stress, denoted by m, from inferred earthquake slip in coseismic slip models and focal mechanisms. The orientations of the principal stresses are defined through the trend and plunge of the most compressive stress

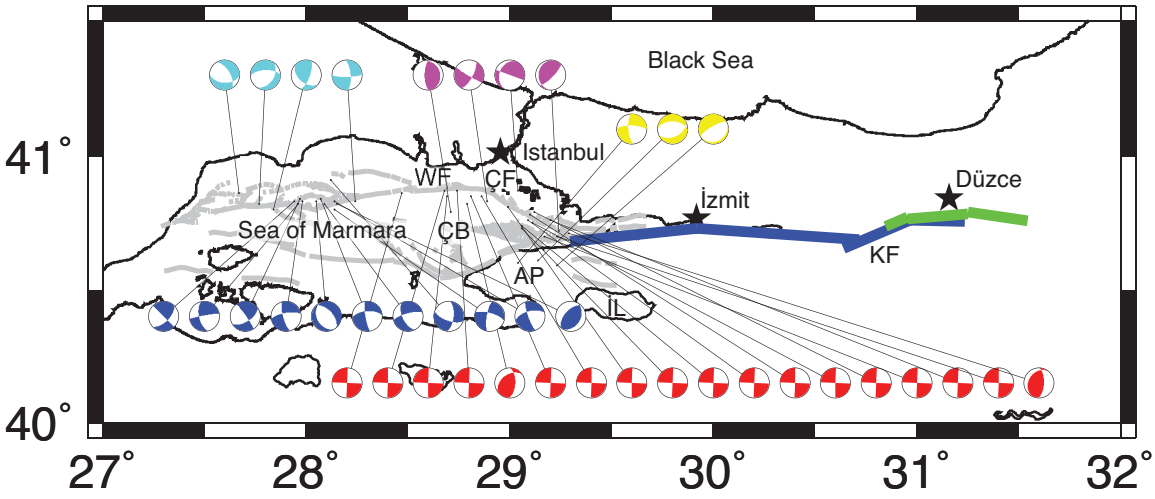

Figure 4.1: Surface trace of İzmit and Düzce earthquakes and focal mechanisms of earthquakes in the Sea of Marmara, Turkey. İzmit trace (blue line) is from Delouis *et al.* (2002) and Düzce trace (green line) if from Delouis *et al.* (2004). Grey lines are mapped faults in the Sea of Marmara from Armijo *et al.* (2005). Focal mechanisms are not scaled to the magnitude of the earthquake, and are from Örgülü (2011; blue), Ergin *et al.* (1997), Kiratzi (2002), and Pinar *et al.* (2003; cyan, magenta, and yellow), and Bulut *et al.* (2009; red). Cyan and blue focal mechanisms are on the Western fault (WF) segment of the Main Marmara fault, and magenta and red are on the Çinarcik fault (ÇF) segment. Yellow focal mechanisms are in the Armutlu Peninsula (AP). Stars indicate prominent cities. KF = Karadere fault, İL = İzmit Lake.

(MCS) as ϕ_{MCS} and θ_{MCS}, respectively, and by the rotation of the intermediate and least compressive stresses (ICS and LCS, respectively) around the MCS, defined as ρ_{MCS}. Magnitudes of MCS, ICS and LCS are denoted by σ_1, σ_2, and σ_3, respectively, with compressive stresses defined to be negative ($\sigma_1 \leq \sigma_2 \leq \sigma_3 \leq 0$). Estimation of stress from earthquake data is insensitive to the absolute magnitude of stress (Célérier, 1988). We define relative stress ratios of the stress tensor as

$$\Delta = \frac{(\sigma_2 - \sigma_3)}{(\sigma_1 - \sigma_3)} \tag{4.1}$$

(e.g., Angelier, 1979; Etchecopar *et al.*, 1981) and

$$R_3 = \frac{\sigma_3}{\sigma_1}. \tag{4.2}$$

We follow a Monte Carlo sampling strategy, such that stress models (*i.e.*, samples of a prior) are accepted in proportion to the likelihood of the predicted slip rake compared to the slip rake in either a coseismic slip model or a focal mechanism. The accepted stress models are then samples of a posterior PDF, which we denote as $P_j(m)$, where for a coseismic slip model j is a fault segment and for a focal mechanism j is one of the two nodal planes. We denote the samples of the prior as $p(m)$, and $P_j(m)$ is related to the prior through Bayes' theorem as

$$P_j(m) = k\, L(\hat{\lambda}_j|m)\, p(m), \tag{4.3}$$

where $L(\hat{\lambda}_j|m)$ is the likelihood of the predicted slip rake, $\hat{\lambda}_j$, on each slip surface for a given stress model, and k is an unknown normalization constant (e.g., Mosegaard and Tarantola, 1995; Tarantola, 2004). $\hat{\lambda}_j$ is taken to be the direction of maximum shear stress resolved on slip surface j. We calculate the likelihood of $\hat{\lambda}_j$ in a Gaussian sense as

$$L(\hat{\lambda}_j|m) \propto \exp\left\{-\frac{\angle(\lambda_j, \hat{\lambda}_j)^2}{2\sigma_\lambda^2}\right\}, \tag{4.4}$$

where $\angle(\lambda_j, \hat{\lambda}_j)$ is the angle difference between the predicted slip rake and the slip rake from either the coseismic slip models or focal mechanisms. The uncertainty of the slip rake, σ_λ, is discussed below.

We initially assume priors in which all principal stress orientations are equally likely. We assume R_3 is uniform within the range 0.21–1, and Δ is uniform in the range 0–1. The lower bound of R_3 avoids unreasonably high deviatoric stresses, and corresponds to a state of stress in which an optimally oriented fault will fail at a

static coefficient of fault friction, μ_f of 0.85. The upper bound of R3 corresponds to an isotropic state of stress. We avoid these isotropic stresses by adding a further constraint based on Mohr-Coulomb failure criterion, as described below. We select eight million random samples of this prior, which we test against all of the coseismic slip models and focal mechanisms. Using common prior samples allows us to form joint posteriors by taking the intersection of individual posteriors (*i.e.*, selecting model stresses that are consistent with all of the individual constraints).

4.3.1 Coseismic Slip Model Constraints

The coseismic slip models we consider here approximate fault geometries using several planar fault segments, with each segment discretized by a number of subfaults. Fault segment j is defined by a constant fault segment strike, ϕ_f^j, and dip, θ_f^j, while the slip rake on subfault i of fault segment j is λ_i^j. We assume an uncertainty of λ_i^j, given by

$$\sigma_{\lambda_i}^j = \min\left(180^\circ, 15^\circ \frac{s_i^j}{s_{\max}}\right), \tag{4.5}$$

where s_i^j is the coseismic slip on subfault i of segment j, and $s_{\max}$ is the maximum coseismic slip inferred in the coseismic slip model. Weighting the uncertainty by the relative magnitude of slip inferred in that subfault ensures that subfaults with low slip minimally contribute to the likelihood of a given stress model. Uncertainties in the fault geometry can be included, but for simplicity we consider ϕ_f^j and θ_f^j to be known. We test each stress model against slip in all of the subfaults, accepting those stresses consistent with all subfaults as samples of the posterior.

4.3.2 Focal Mechanism Uncertainty

Here we use focal mechanisms determined for M_w 1.5 to 4.5 earthquakes in the Sea of Marmara from Ergin *et al.* (1997), Kiratzi (2002), Pinar *et al.* (2003), Bulut *et al.* (2009), and Örgülü (2011). We additionally consider a focal mechanisms from the

1939 M_w 7.8 Erzincan earthquake on the eastern region of the NAF from Şengör *et al.* (2005). We use the focal mechanisms as reported by Ickrath *et al.* (2014), which are compiled from these sources. Since it is unknown which nodal plane corresponds to the slip surfaces, we estimate the stress posteriors for each nodal plane individually by accepting each of the prior samples in proportion to the likelihood of the computed rake on that nodal plane, $\hat{\lambda}_j$, where $j = 1$ or 2 for nodal plane 1 (NP1) or 2 (NP2), respectively. The stress posterior from each focal mechanism is then the union of all samples consistent with either of the two nodal planes.

We assume an uncertainty of 20° for the nodal plane strike (σ_ϕ), dip (σ_θ), and slip rake (σ_λ). While this uncertainty is rather large, we note that the majority of the focal mechanisms we consider are small. The uncertainty in the fault geometry is incorporated in our calculations by choosing ϕ_j and θ_j randomly from Gaussian PDFs with mean given by the strike and dip, respectively, in the focal mechamisms and variances $\sigma_\phi^2/\sin^2\theta_f$ and σ_θ^2.

Samples of a joint posterior of stress inferred from multiple focal mechanisms are found as the intersection of samples of each of the constituent posteriors from the individual focal mechanisms (*i.e.*, the samples of the joint posterior are those stress models the are consistent with all of the focal mechanisms). (We note that we test the same samples of the prior against all of the focal mechanisms.)

4.3.3 Mechanical Constraint

The prior includes stress models that are near isotropic, and therefore the posteriors found above also include these near isotropic stress models. While these stress models are consistent with the direction of maximum shear stress resolved on a fault plane, they are not mechanically consistent with coseismic slip. Specifically, maximum fault shear stress in near isotropic stress models will be vanishingly small; therefore the fault would only cosesimically fail at a corresponding vanishingly small friction.

To avoid these isotropic stress models, we impose a mechanical constraint based on a Mohr-Coulomb failure criterion.

We define the Coulomb stress ratio, $\hat{\mu}_j$ on each slip surface as

$$\hat{\mu}_j = \frac{\tau_j}{\sigma_j}, \tag{4.6}$$

where τ_j and σ_j are the maximum shear stress and the normal stress calculated on the slip surface j. The fault will then fail at the given stresses provided $\hat{\mu}_j \geq \mu_f$ on either the geodetically inferred slip surface or one of the nodal planes. Applying this mechanical constraint, we denote the modified posterior as

$$P_\mu(m) = k \sum_{j=1}^{N} L(\hat{\mu}_j|m)\, P_j(m), \tag{4.7}$$

where N is the number of slip surfaces considered, $L(\hat{\mu}_j|m)$ is the likelihood that $\hat{\mu}_j$ is consistent with Mohr-Coulomb failure for a prior assumption of μ_f, and k is a constant. In our BMC sampling strategy, the constraint k does not need to be determined.

While the prior assumption of μ_f can be any PDF, in this study we assume that μ_f is uniform in the range $[0.1, 0.7]$. In our Monte Carlo sampling strategy, samples of the prior $P_j(m)$ are retained as samples of $P_\mu(m)$ as long as

$$0.1 \leq \hat{\mu}_j \leq 0.7 \tag{4.8}$$

on the fault segments of the coseismic slip models and/or one of the nodal planes in the focal mechanisms. In the below analysis, only 0.3–1.5% of the stress models in $P_j(m)$ were rejected based on having a $\hat{\mu}_j > 0.7$. While somewhat arbitrary, our choice of the lower bound includes in situ measurements of friction from recent fault samples, (e.g. Carpenter *et al.*, 2009; Schleicher *et al.*, 2010; Kuo *et al*, 2014; Warr

et al., 2014).

4.4 Stress inferred from İzmit Coseismic Slip Models

We consider three coseismic slip models of the İzmit earthquake, those of Reilinger *et al.* (2000), Delouis *et al.* (2002) and Çakir *et al.* (2003b). All three coseismic slip models include the Karadere fault segment of the NAF which deviates by about 30° from the rest of the predominantly E-W trending NAF. Our main focus is on the Delouis *et al.*, (2002) İzmit coseismic slip model, which we refer to as the DI model, because it is derived from the largest number of data constraints, including GPS, InSAR, teleseismic waves, and near-field strong motion data.

Stress inferred from each coseismic slip model indicates a homogenous stress consistent with all fault segments (Figures 4.2 and B.1). The highest likelihood stresses consistent with all İzmit coseismic slip models have subhorizontal MCS, trending NW-SE, vertical ICS, and subhorizontal LCS trending NE-SW. Although less likely, stress models with either MCS or LCS near vertical and ICS horizontal are also possible (Figures 4.2 and B.1). The large range of permissible orientations is due to the inherent ambiguity in identification of the principal stresses when inverting coseismic slip models with relatively uniform slip rake on constant geometry slip surface, similar to the ambiguity in stress inferences from single focal mechanisms (e.g. Chapter 4; Célérier, 1988; Arnold and Townend, 2007). R_3 in the posterior mirrors the distribution in the prior with no correlations between R_3 and any other parameter in the posterior. The posterior favors stress models with low Δ (Figures 4.2 and B.1), indicating that the magnitude of ICS is closer to the magnitude of LCS than to the magnitude of MCS.

The above posterior did not include any mechanical constraint, leading to two potential issues: (1) that the posterior includes near isotropic stress models, and (2) that μ_f on each of the four segments may vary for a given stress model. We

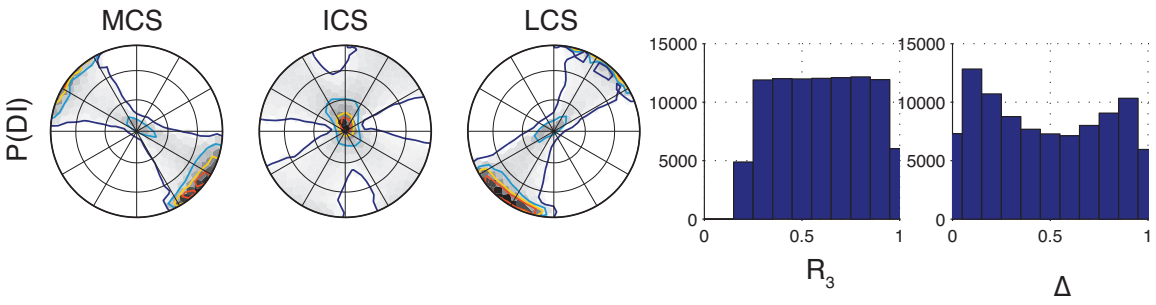

Figure 4.2: Orientations of principal stresses, $R3$ and Δ of stress models consistent with the DI model. Densities of orientations of posterior samples are shown in Lambert projections of the lower hemisphere: contours indicate the $0.01p_{\mathrm{MLE}}$ (dark blue), $0.2p_{\mathrm{MLE}}$ (light blue), $0.5p_{\mathrm{MLE}}$ (yellow), and $0.75p_{\mathrm{MLE}}$ (red) levels, where p_{MLE} is the maximum density; shading indicates density of samples in the posterior, with black indicating highest density (*i.e.*, highest likelihood) and white indicating zero density (*i.e.*, no likelihood).

address the second point, focusing on the DI model. The implications of a particular stress model having different μ_f in each of the fault segments, is that since all of the segments are inferred to have slipped during the İzmit earthquake, friction on each segment would have to vary if a single homogeneous stress caused the slip on those segments. In particular, the strike of the Karadere segment might only be consistent with slip if friction on that segment were lower than on the other three segments. Indeed, we find that slip on all fault segments is consistent with approximately the same friction and homogeneous stress if $\mu_f \lessapprox 0.225$ (Fig. 4.3). For larger friction, a single stress model is only consistent with slip on all four of the segments in the DI model if the Karadere segment has a lower friction than that of the other more E-W striking segments (Fig. 4.3). If $\mu_f \gtrapprox 0.4$ on the three E-W striking segments, μ_f can be about 0.2 lower on the Karadere segment.

For the mechanical constraint on the DI coseismic slip model, we set the range of μ_f to be between 0.1 and 0.7, ensuring that the posterior encompasses models that are consistent with slip on all fault segments of this model. In setting a constraint on μ_f, we find that high R_3 values are correlated with low μ_f values, while low R_3

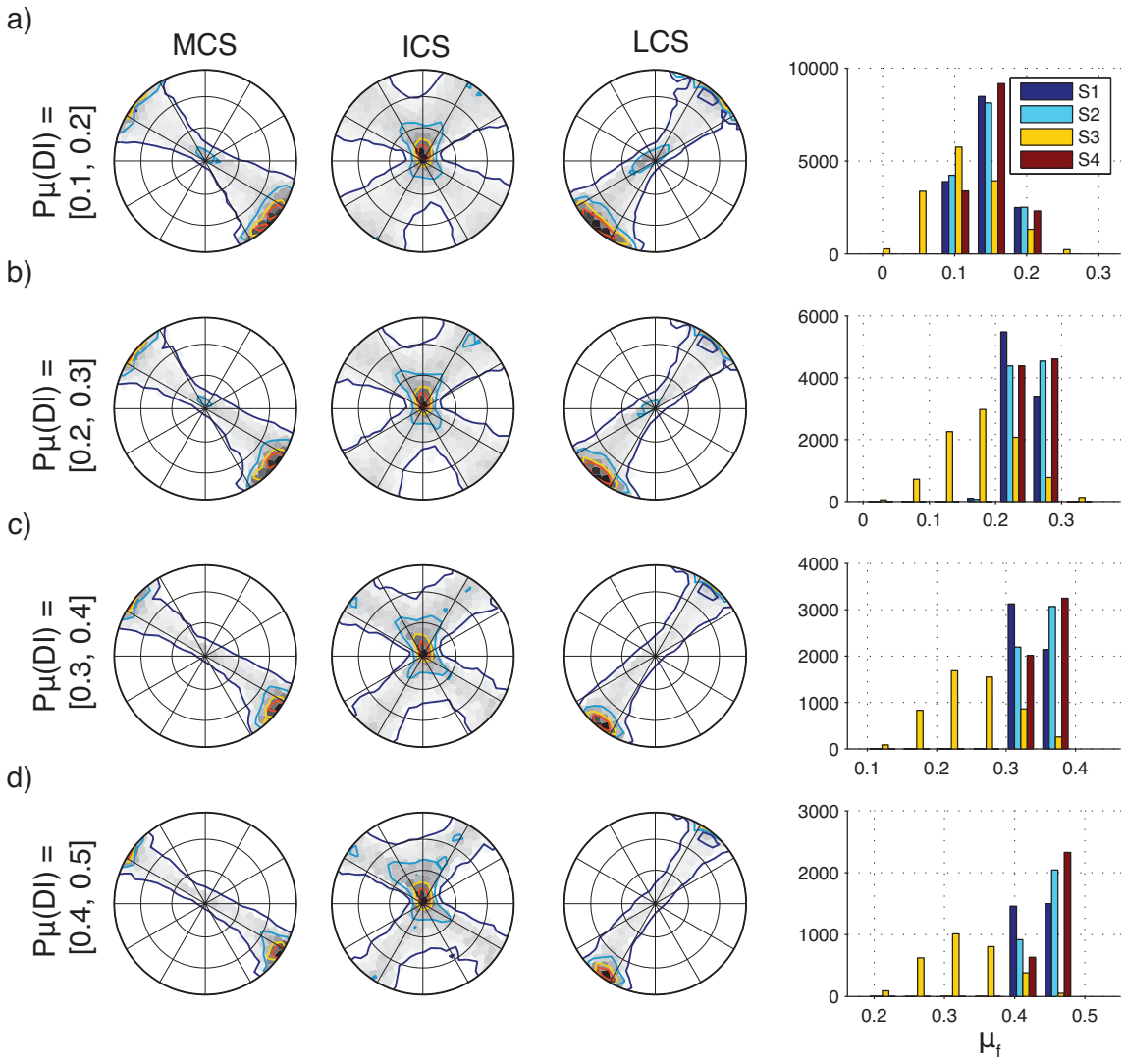

Figure 4.3: Stress orientations of stress models consistent with the DI model under different conditions of static fault friction, μ_f (a-d). Histograms indicate the number of models of the posterior consistent with slip for each fault segment (S1-S4, colors) under each μ_f range. The Karadere fault segment, S3, consistently requires low μ_f to meet failure.

values are correlated with high μ_f values. Such a correlation between Δ and μ_f is not observed; however, Δ and principal stress orientations are correlated (Arnold and Townend, 2007; Chiba *et al.* 2012), as described in Chapter 3. Orientations of MCS near vertical become more likely at high Δ, whereas LCS near vertical becomes more likely at low Δ. The ambiguity between MCS and LCS is evident for high and low

Δ ranges, respectively. There is a higher likelihood that ICS is more vertical than horizontal, for all Δ.

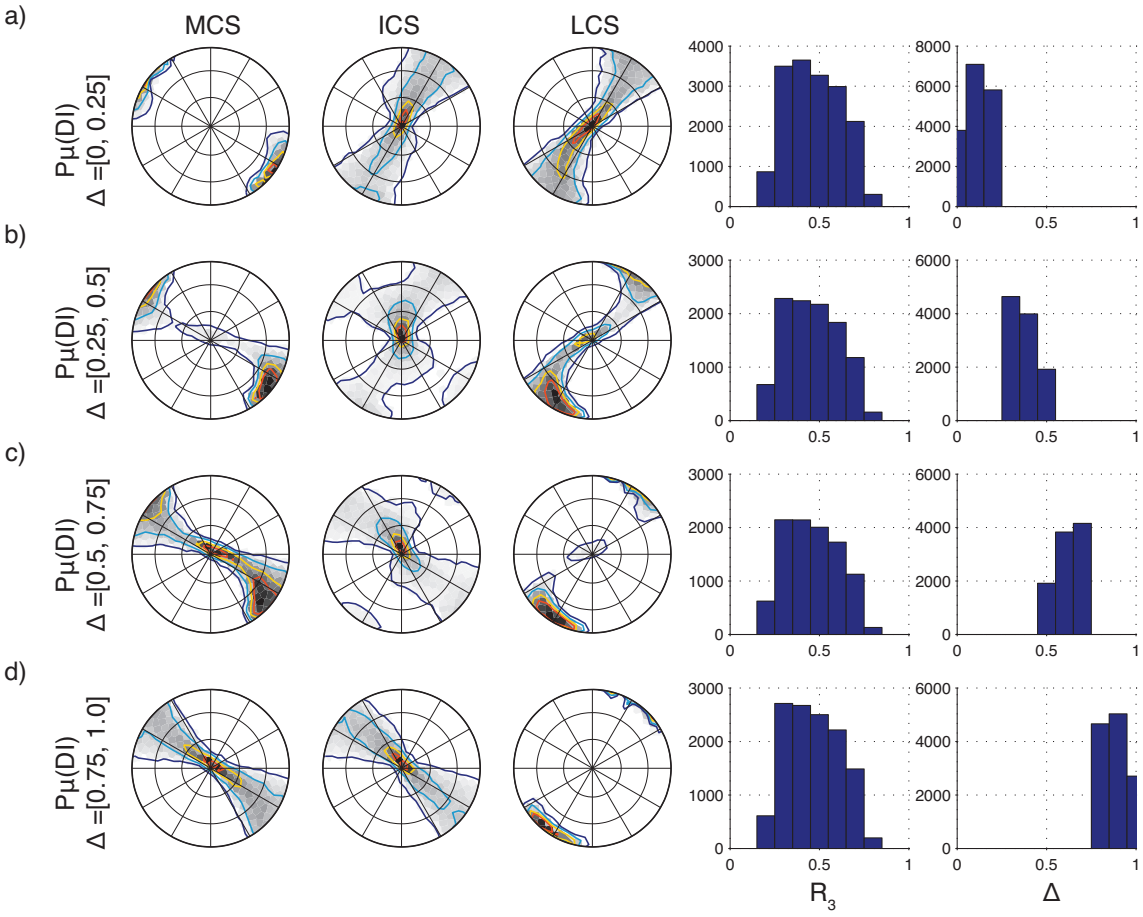

Figure 4.4: Orientations of principal stresses, R_3, and Δ of stress models consistent with the DI model for different ranges of Δ. For low Δ, an ambiguity between ICS and LCS is observed, while for high Δ, the ambiguity is between MCS and ICS. At low Δ MCS is oriented subhorizontal and NW-SE trending and becomes vertical at high Δ values. R3 remains unaffected.

We estimate joint posteriors of the DI, CI, and RI models to quantify the consistency of stress inferred from all three coseismic slip models. We construct these joint posteriors by testing the samples of the mechanically constrained DI posterior against the CI and RI coseismic slip models. Stress models are only accepted as samples of the joint posteriors if $\hat{\mu}$ on the fault segments of the CI or RI models is also between 0.1 and 0.7. Not surprisingly, the joint posteriors are nearly indistinguishable from

those estimated from only the DI coseismic slip model (cf. Figures B.2 and 4.2). One difference, however, is that the joint posteriors encompass more stress models with low Δ, with correspondingly higher likelihood of a subhorizontal MCS. However, we note that the CI and RI models are less constrained than the DI model, and thus we only present these joint posteriors to demonstrate the consistency of the independent solutions.

4.5 Stress inferred from Düzce Coseismic Slip Models

We consider two coseismic slip models of the Düzce earthquake, those of Çakir *et al.* (2003a) and Delouis *et al.* (2004), referred to as CD and DD, respectively. The DD model includes the Karadere fault segment, while the CD model does not. Results from the inferred posterior of stress from the CD and DD model indicate a homogeneous stress consistent with slip on all fault segments (Figures B.3a and 4.5a, respectively). In both posteriors, the highest likelihood MCS and LCS orientations are plunging about 15°–30° SE and SW, respectively, while the ICS is about 30° off of vertical. R_3 is nearly uniform in the posterior, essentially mirroring the distribution of R_3 in the prior, and is not correlated with stress orientations. Posteriors from both models indicate a slight preference of models with Δ near 1, indicating models with ICS magnitude near MCS magnitude.

4.5.1 Joint İzmit and Düzce coseismic slip models

We determine the stress models that are jointly consistent with the DI and DD coseismic slip models. Stress models which are samples of the mechanically constrained DI posterior are used as prior samples that are tested against the DD model. As in the joint İzmit analysis above, we only accept samples of stress models of the joint DI-DD posterior if μ_f on all segments is between 0.1 and 0.7.

The resulting joint posterior indicates a state of stress consistent with the stress

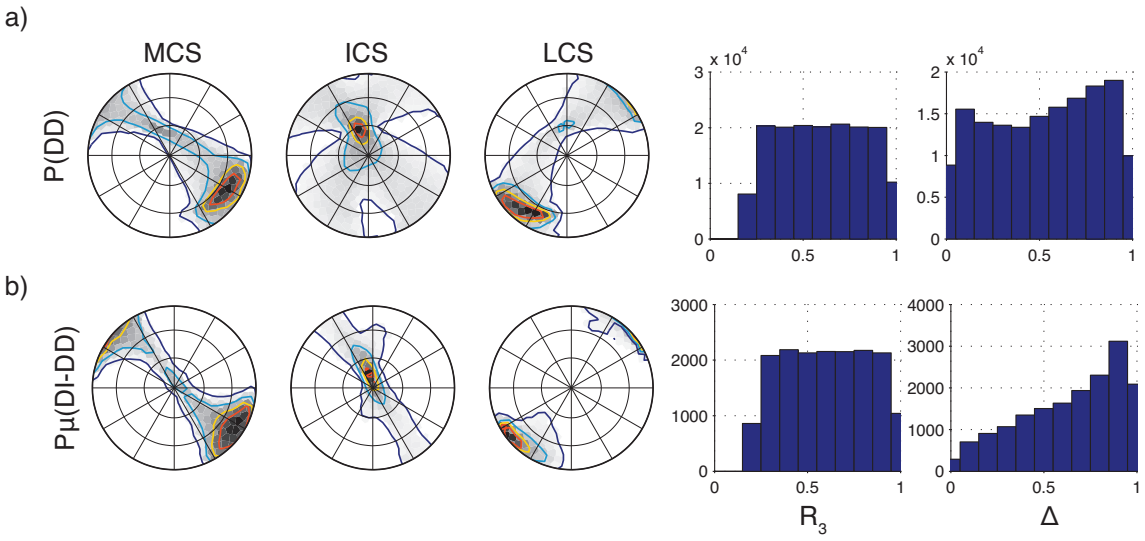

Figure 4.5: (a)Orientations of principal stresses, R_3, and Δ of stress models consistent with the DD coseismic slip model. (b) Orientations and relative magnitudes of stress models jointly consistent with the DI and DD models with a prior constraint of μ_f.

that led to the İzmit earthquake (Figures 4.5b and B.3b). Stress models that are consistent with both the DI and DD models are characterized by a subhorizontal, NW-SE trending MCS, with the likelihood of near vertical MCS diminished compared to the constituent posteriors. Similarly, near vertical LCS directions are completely absent in the joint posterior of DI and CD (cf. Figures 4.5b and B.3b).

As in the case for the segments composing the DI coseismic slip model, slip on all fault segments of the DD model are only consistent with Mohr-Coulomb failure for $\mu_f \lessapprox 0.2$ (Figure 4.6). Additionally, for larger friction values, the Karadere segment consistently exhibits lower $\hat{\mu}$ values than on the other nearly E-W trending segments. These results may argue for either a consistently low friction, a lower friction on the Karadere segment than on the other fault segments, or a different stress on the Karadere segment.

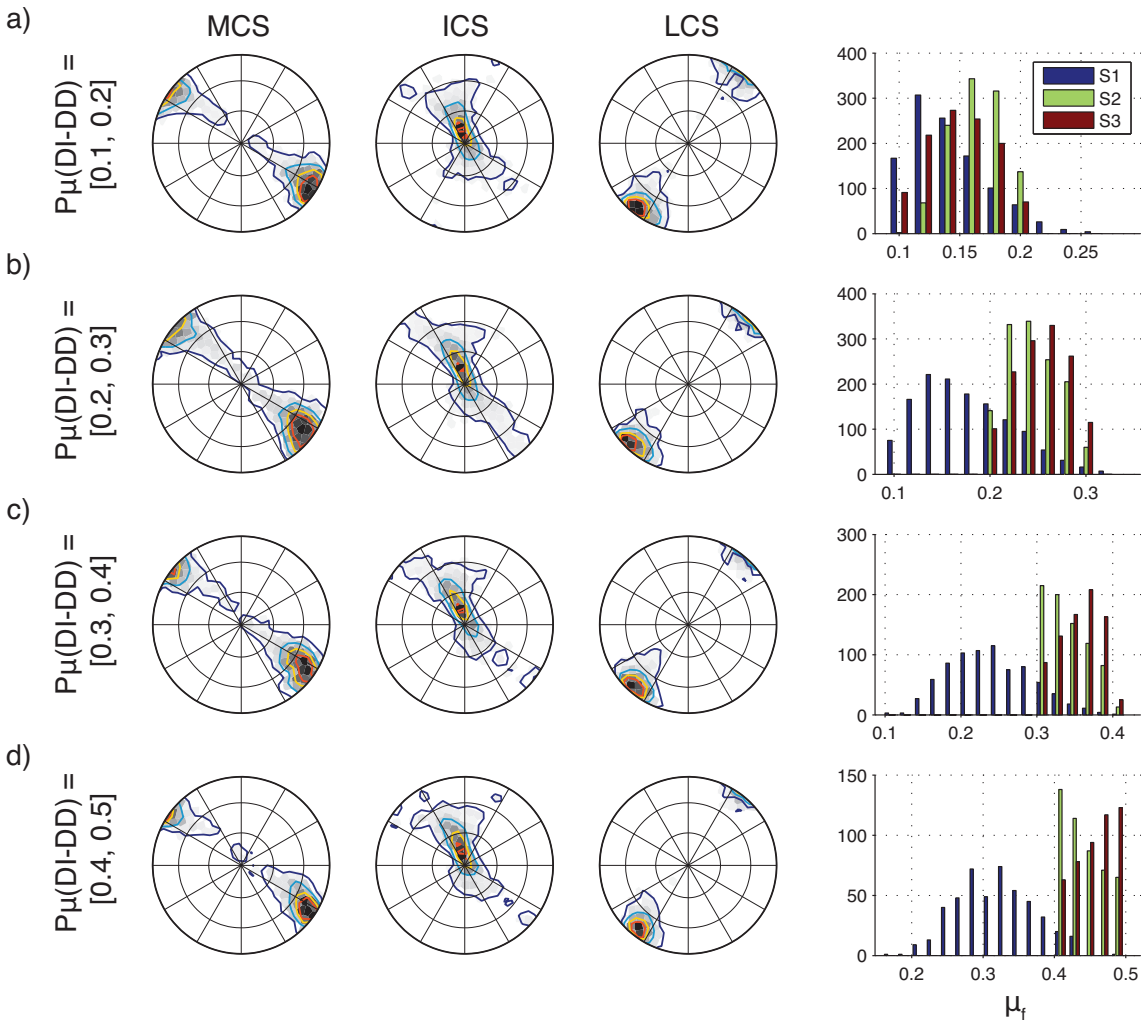

Figure 4.6: Orientations of principal stresses jointly consistent with the DI and DD models under different conditions of static fault friction, μ_f (a-d). Histograms indicate the number of models of the joint posterior consistent with slip for each fault segment (S1-S3, colors) under each μ_f range. The Karadere fault segment (S1) consistently requires low μ_f to meet failure.

4.6 Stress inversion of 1939 M_w 7.8 event

An inversion of stress from a single focal mechanism provides a very low level of constraint on the state of stress that generated that earthquake. However, to assess whether the inferred stress that led to the İzmit and Düzce earthquakes is consistent with the stress at the eastern end of the NAF, we consider the focal mechanisms of the 1939 Erzincan M_w 7.8 earthquake taken from Ickrath *et al.* (2014). We

assume that the nodal plane corresponding to the NAF represents the slip surface. Likely stress orientations consistent with slip on this fault plane indicate MCS and LCS are oriented about 15° off of subhorizontal and plunging to the SE and NE, respectively, with the ICS 30° off of near vertical and plunging towards the west. Posteriors indicate R_3 and Δ are uniform. The joint posterior of the DI model with the 1939 event, assuming $0.1 \leq \hat{\mu}_j \leq 0.7$, indicates a similarly oriented MCS to that of mechanically constrained posterior of the DI model, P_μ(DI): MCS is subhorizontal and trending NW-SE. The joint posterior indicates low Δ, with an ambiguity between ICS and LCS clearly observed in the lower hemisphere projection, similarly observed in the joint posterior of P_μ(DI-CI) and P_μ(DI-RI) (Fig. B.2).

4.7 Seismicity in the Sea of Marmara

We consider focal mechanisms of several earthquakes within the Sea of Marmara. Epicenters of focal mechanisms lie along the northern Main Marmara fault (MMF; Pinar *et al.*, 2001), which is segmented into the NW-SE trending Çinarcik fault segment (also known as Princes' Islands fault; Pinar *et al.*, 2001; Ucarkus *et al.*, 2011), and an E-W trending Western fault (WF) segment (which connects to the NE-SW Ganos fault to the west; Figure 4.1). The Çinarcik fault segment delineates the northern boundary of the Çinarcik Basin (ÇB) and is the western extent of the NAF, where little to no coseismic slip from the İzmit earthquake was observed (Pinar *et al.*, 2010). Focal mechanisms were determined for aftershocks at the western extent of the İzmit rupture (e.g., Bohnhoff *et al.*, 2006; Pinar *et al.*, 2010, Ickrath *et al.*, 2014); however, we only focus on earthquakes prior to 1999, after 2003, and farther from the İzmit rupture. We assume a uniform prior for all focal mechanisms, and the joint posteriors are further mechanically constrained with μ_f between 0.1 and 0.7. We consider focal mechanisms of pre- and post-İzmit earthquakes along the WF segment, the Çinarcik fault segment (ÇF), and in the Armutlu Peninsula, (AP) separatly.

4.7.1 Stress inversion estimated from pre-İzmit earthquakes

Joint posteriors of stress determined from pre-İzmit focal mechanisms suggest a heterogenous stress along the MMF. In particular, the stress along the WF segment indicates a predominantly near E-W trending, subhorizontal MCS, a near vertical ICS, and near N-S trending, subhorizontal LCS (Figure 4.7, Table 4.1). In contrast, stress inverted from focal mechanisms along the ÇF segment indicate posteriors with MCS rotated $\approx 65°$, trending NW-SE and subhorizontal. ICS and LCS orientations along the ÇF are within the highest likelihood of LCS plunging steeply to the NE (Figure 4.7). Stress from the focal mechanisms within the AP yields a near vertical MCS, WNW-ESE trending and subhorizontal ICS, and a NE-SW trending, subhorizontal LCS. In all three regions, R_3 and Δ result in similar distributions of relative stress magnitudes. The variability of stress from the ÇF to the WF segments and in the AP is further discussed below.

4.7.2 Stress inversion estimated from post-İzmit earthquakes

Similar to the stress inversion from pre-İzmit focal mechanisms, a heterogeneous stress is determined from post-İzmit focal mechanisms from the WF to the ÇF segments. There are no focal mechanisms determined for earthquakes in the AP after 2003. Along the WF segment, MCS trends WNW-ESE and subhorizontal, ICS is vertical, and LCS trends NNE-SSW and is subhorizontal (Figure 4.7, Table 4.1). Posteriors of stress from focal mechanisms along the ÇF segment indicate a near N-S trending, subhorizontal MCS, and variability in the ICS and LCS from near horizontal to near vertical, each trending along E-W. Histograms of Δ in each joint posterior indicates preference for near 0.5 Δ along the WF segment, whereas a preference for low Δ near zero is observed along the ÇF segment. The similarities and differences between stress estimated from pre- and post-İzmit focal mechanisms is discussed below.

Events		Western Segment (E-W)		
		MCS	ICS	LCS
pre-İzmit	ϕ (°)	276.76 ± 27.59	113.10 ± 39.89	11.99 ± 23.23
	θ (°)	17.76 ± 35.13	24.03 ± 40.63	13.39 ± 20.39
post-İzmit	ϕ (°)	119.41 ± 10.72	2.71.73 ± 48.11	29.25 ± 9.48
	θ (°)	2.58 ± 18.18	49.17 ± 53.52	8.79 ± 13.35

		Çinarcik segment (NW-SE)		
		MCS	ICS	LCS
pre-İzmit	ϕ (°)	161.50 ± 29.12	257.28 ± 38.43	64.23 ± 32.78
	θ (°)	9.34 ± 19.85	19.27 ± 34.83	29.52 ± 40.56
post-İzmit	ϕ (°)	349.20 ± 7.05	255.18 ± 15.09	77.48 ± 10.22
	θ (°)	0.62 ± 6.00	44.2 ± 19.03	44.85 ± 19.93

		Armutlu Peninsula		
		MCS	ICS	LCS
pre-İzmit	ϕ (°)	145.20 ± 41.20	287.62 ± 38.18	22.19 ± 35.67
	θ (°)	37.16 ± 42.87	8.59 ± 30.57	11.44 ± 19.56

Table 4.1: Table of mean and standard deviation of principal stress orientations of posterior stress models estimated from focal mechanisms in the Sea of Marmara. Given standard deviation is that of the orientations of principal stresses of all posterior stress models, and roughly represents the 68% credible interval. ϕ and θ are the trend and plunge, respectively, of the principal stresses.

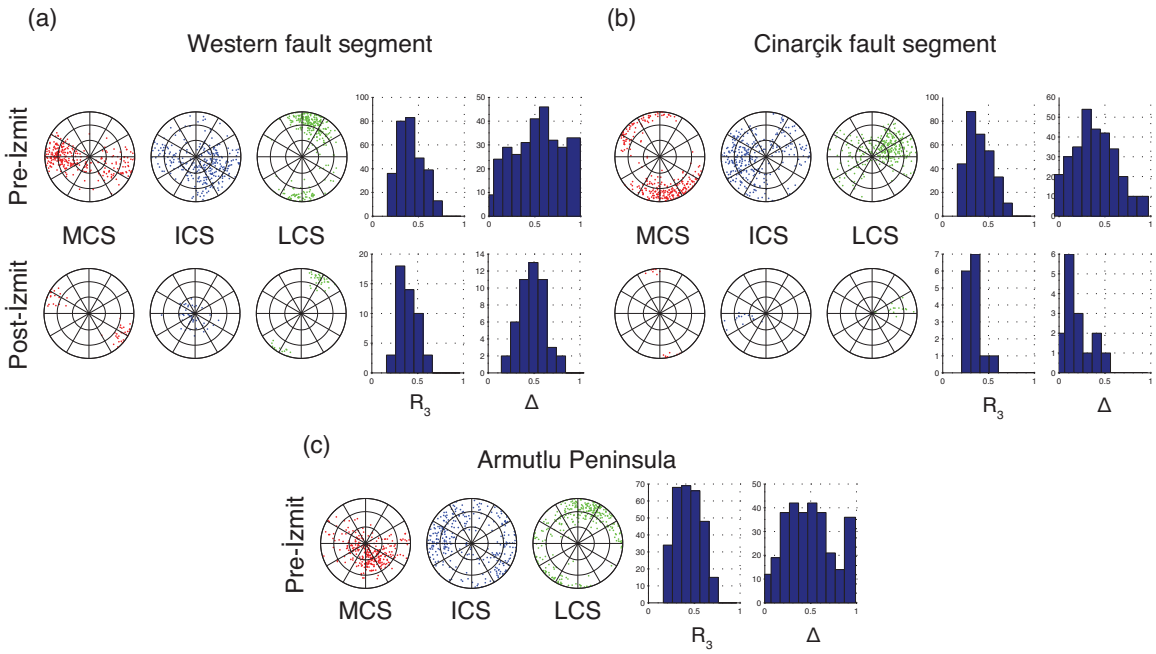

Figure 4.7: Orientations of principal stresses, R_3, and Δ of posterior stress models inferred from focal mechanisms in the Sea of Marmara (a) along the Western fault segment (WF), (b) along the Çinarcik fault segment (ÇF), and (c) within the Armutlu Peninsula (AP). Orientations of principal stresses are depicted as points projected on a Lambert projection in the lower hemisphere, with high density of points indicating high likelihood regions. A subsample of 300 models for the pre-İzmit joint posteriors are shown, and are representative of the 7,338 posterior samples along the WF, 5,622 posterior samples along ÇF, and 56,542 posterior samples in the AP

4.8 Discussion

These results indicate that a homogenous state of stress is capable of having caused both the İzmit and Düzce earthquakes, as long as either $\mu_f \lessapprox 0.22$ on all segments or μ_f on the Karadere segment is lower than on the adjacent segments. Alternatively, μ_f may be uniformly higher on all segments in which case stress would have to differ on the Karadere segment, although we do not quantify this possibility here. The stress that caused the 1939 M_w 7.8 earthquake on the eastern extent of the NAF is consistent with that inferred from the İzmit and Düzce coseismic slip models. Specifically, the inferred homogeneous stress is characterized by a NW-SE trending, subhorizontal MCS, near vertical ICS, and a subhorizontal, NE-SW trending LCS

(Figures 4.2 and 4.5), with a broad distribution of Δ around 0.5.

The northern boundary of the Çinarcik Basin delineates the right-lateral strike slip extent of the western NAF (e.g. Le Pichon *et al.*, 2003; Şengör *et al.*, 2005; Bulut *et al.*, 2009). Fault segments within the Sea of Marmara represent an ∼100 km gap in seismicity (Bulut *et al.*, 2009), and thus pose an ongoing seismic hazard for the ∼15 million inhabitants in the Istanbul region (e.g., Parsons *et al.*, 2000; King *et al.*, 2001; Atakan *et al.*, 2002; Meade *et al.*, 2002; Le Pichon *et al.*, 2003; Şengör *et al.*, 2005). Faulting in the Sea of Marmara is complex, including transform, extensional, and compressional features (e.g., Şengör *et al.*, 2005; Armijo *et al.*, 2005). Extensional components are predominantly defined within the ÇB, whilst transform slip is localized along segments of the MMF (Şengör *et al.*, 2005; Pinar *et al.*, 2010).

Within the Sea of Marmara, we focus on the few focal mechanisms available along the MMF, which suggest a heterogeneous stress along this fault. The results show a NNW-SSE trending, sub-horizontal MCS along the ÇF segment of the MMF, aligned near the trend of the ÇF segment. The ICS and LCS along this segment are inferred to be most likely dipping, with highest likelihood dipping to the SW and NE, respectively (Figure 4.7). The results along the more E-W trending WF segment to the west indicate MCS is sub-horizontal and trending close to the fault strike, with LCS sub-horizontal and N-S trending, and ICS steeply plunging (Figure 4.7). The change in stress from the on-shore NAF to the ÇF segment may have played a role in the termination of fault slip during the İzmit earthquake west of the Sea of Marmara.

Interestingly, the earthquakes after 2003 require a more NW-SE trending MCS, vertical ICS, and SW-NE trending LCS, suggesting that the stress along the WF segment may have rotated clockwise ($\sim 10-20^{\circ}$) to a more transform state of stress. However, the posteriors are relatively under-sampled, and we explore this hypothesis in a future study. In contrast, stress inferred along the ÇF prior to and following the İzmit earthquake does not suggest that the İzmit rupture changed the stress field.

Since the İzmit earthquake did not result in a noticeable change in stress on the ÇF segment, we do not feel that the possible change in stress along the WF is due to stress changes from the İzmit earthquake. If the suggested rotation of stress to a more optimal stress for strike-slip faulting on the WF holds with further analysis, this may have profound implications on time-dependent earthquake hazards in the region.

GPS measurements of strain accumulation, focal mechanisms from aftershocks of the İzmit earthquake, and focal mechanisms of earthquakes prior to and following the İzmit earthquake all indicate right lateral displacement along the northern ÇB, on the ÇF (e.g., Meade *et al.*, 2002; Flerit *et al.*, 2004; Bulut *et al.*, 2009). Strain accumulation measurements and the time since the last earthquake in the Sea of Marmara indicates a slip deficit of 4-5 m, and the propensity for a large ($M_w \geq 7.4$) strike-slip earthquake (Hubert-Ferrari *et al.*, 2000; Bulut *et al.*, 2009), or possibly many normal slip events with smaller magnitudes (Armijo *et al.*, 2002; Bulut *et al.*, 2009). However, Meade *et al.* (2002) argued that the potential magnitude of an earthquake in the Sea of Marmara was likely less, and that the most active strand of the NAF in the Sea of Marmara was to the south of the MMF. Nevertheless it is clear that there is strain partitioning along the MMF (Le Pichon *et al.*, 2001; Şengör *et al.*, 2005).

Our interpretation of stress within the Sea of Marmara near Istanbul is similar to the interpretation of the pre-Izmit stress by Ickrath *et al.* (2014). Their stress inferences were based on a larger set of focal mechanisms in the İzmit rupture, including earthquakes both before and after the İzmit earthquake. They favored a single state of stress along the İzmit earthquake rupture, although any complexities in the local stress field may be obscured by including earthquakes in the broader region.

4.9 Conclusions

We use coseismic slip models and focal mechanisms to estimate stress along the NAF east of and within the Sea of Marmara. Coseismic slip models of both the İzmit and Düzce earthquakes are examined independently and jointly. We find that both İzmit and Düzce earthquakes are consistent with a NW-SE subhorizontal MCS, near vertical ICS, and a subhorizontal LCS trending NE-SW. However, this homogeneous stress is only consistent with coseismic slip on all fault segments if either $\mu_f \lessapprox 0.22$ on all segments or μ_f is lower on the Karadere segment (up to about 0.2 lower). We find that stress varies along the MMF in the Sea of Marmara. Specifically, inferred stress rotates about $50° - 60°$ from the ÇF to the WF segments of the MMF. Highest likelihood MCS orientations trend NNW-SSE with a slight plunge to the SSE along the ÇF, and trend WNW-ESE with a slight plunge to the west along the WF. LCS trends WSW-ENE and plunges to the ENE on the ÇF, and trends NNE-SSW and near horizontal along the WF. There is a suggestion that stress along the WF has rotated to a more transform-favorable stress state after about 1999. Focal mechanisms in the Armutlu Peninsula suggest a steeply dipping MCS, with a sub-horizontal ICS and LCS weakly constrained.

4.10 Data and Resources

Coseismic slip models of the İzmit and Düzce, Turkey, earthquakes were acquired through the Finite Source Rupture model database (http://equake-rc.info/SRCMOD/) and personal communication with authors of the slip models cited in the references. Focal mechanisms of seismicity in the Sea of Marmara were acquired through personal communication of authors cited in the text and in the references.

4.11 Acknowledgments

We would like to thank authors of the İzmit and Düzce coseismic slip models for helping us understand the parameters in their models. We would also like to thank Michele Ickrath and those authors who recorded seismic activity in the Sea of Marmara, for providing us with the full focal mechanism data sets. Matlab (The Mathworks, Inc.) was used fro all calculations and to generate figures presented in this chapter.

4.12 References

Aki, K., and Richards., P. G. Quantitative Seismology, 2nd Edition. Sausalito: University Science Books, (2009). Print.

Angelier, J., (1979). Determination of the mean principal directions of stresses for a given fault population. Tectonophysics **56**, T17T26, doi: 10.1016/0040-1951(79)90081-7.

Angelier, J., (1984). Tectonic analysis of fault slip data sets. J. Geophys. Res., V. 89, B7, 5835-5848. doi: 10.1029/JB089iB07p05835

Angelier, J., (1989). From orientation to magnitudes in paleostress determinations using fault slip data. J. Struct. Geol., **11**, No. 1-2, 37-50, doi: 10.1016/0191-8141(89)90034-5.

Arnold, R., and J. Townend, (2007). A Bayesian approach to estimating tectonic stress from seismological data. Geophys J. Int., **170**, 1336-1356. doi: 10.1111/j.1365-246X.2007.03485.x.

Armijo, R., Meyer, B., Navarro, S., King, G., and Barka, A., (2002). Asymmetric slip partitioning in the Sea of Marmara pull-apart: a clue to propagation processes of the North Anatolian fault? Terra Nova, **14**, no. 2, ps. 80-86.

Armijo, R., Pondard, N., Meyer, B., Uçarkus, G., de Lé, B. M., Malavieille, J., Dominguez, S., Gustcher, M. A., Schmidt, S., Beck, C., Çagatay, N., Çakir, Z., Imren, C., Eris, K., Natalin, B., Özalaybey, S., Tolun, L., Lefèvre, I., Seeber, L., Gasperini, L., Rangin, C., Emre, O., and Sarikavak, K., (2005). Submarine fault scarps in the Sea of Marmara pull-apart (North Anatolian Fault): Implications for seismic hazard in Istanbul, Geochem. Geophys. Geosyst., **6**, no. 6, Q06009, doi:10.1029/2004GC000896.

Ayhan, M. E., Bürgmann, R., McClusky, S., Lenk, O., Aktug, B., Herrece, E., and Reilinger, R. E., (2001). Kinematics of the Mw = 7.2, 12 November 1999, Düzce, Turkey Earthquake. Geophys. Res. Let., **28**, no. 2, p. 367-370.

Barka, A., (1996). Slip distribution along the North Anatolian fault associated with large earthquakes of the period 1939 to 1967. Bull. Seis. Soc. Am., **86**, no. 5, p. 1238-1254.

Barka, A., Akyuz, H. S., Altunel. E., Sunal, G., Çakir, Z., Dikbas, A., Yerli, B., Armijo, R., Meyer, B., de Chabalier, J. B., Rockwell, T., Dolan, J. R., Hartleb, R., Dawson, T., Christofferson, S., Tucker, A., Fumal, T., Langridge, R., Stenner, H., Lettix, W., Bachhuber, J., and Page, W., (2002). The surface rupture and slip distribution of the 17 August 1999 Izmit Earthquake (M 7.4), North Anatolian Fault. Bull. Seism. Soc. Am., **92**, no. 1, 43-60.

Bohnhoff, M., Grosser, H., and Dresen, G., (2006). Strain partitioning and stress rotation at the North Anatolian fault zone from aftershock focal mechanisms of the 1999 Izmit $M_w = 7.4$ earthquake. Geophys. J. Int., **166**, p. 373-385, doi: 10.1111/j.1365-246X.2006.03027.x.

Bott, M. H. P., (1959). The mechanics of oblique slip faulting. Geological Magazine, **96**, Issue 2, 109-117. doi: 10.1017/S0016756800059987.

Bulut, F., Bohnhoff, M., Ellsworth, W. L., Aktar, M., and Dresen, G., (2009). Microseismicity at the North Anatolian Fault in the Sea of Marmara offshore Istanbul, NW Turkey. J. Geophys. Res., **114** B09302, doi: 10.1029/2008JB006244.

Bürgmann, R., Ayhan, M. E., Fielding, E. J., Wright, T. J., McClusky, S., Aktug, B., Demir, C., Lenk, O., and Türkezer, A., (2002). Deformation during the 12 November 1999 Düzce, Turkey, Earthquake from GPS and InSAR Data. Bull. Seism. Soc. Am., **91**, no. 1, p. 161-171.

Çakir., Z., Barka, A. A., de Chabalier, J. B., Armijo, R., and Meyer, B., (2003a). Kinematics of the November 12, 1999 (Mw=7.2) Düzce earthquake deduced from SAR Interferometry. Turkish J. Earth Sci., **12**, 105-118.

Çakir, Z., de Chabalier, J. B., Armijo, R., Meyer, B., Barka, A., and Peltzer, G., (2003b). Coseismic and early post-seismic slip associated with the 1999 Izmit

earthquake (Turkey), from SAR interferometry and tectonic field observations. Geophys. J. Int., **155**, 93-110, doi: 10.1046/j.1365-246X.2003.02001.x.

Carpenter, B. M., Marone, C., and Saffer, D. M., (2009). Frictional behavior of materials in the 3D SAFOD volume. Geophys. Res. Lett., **36**, L05302, doi: 10.1029/2008GL036660.

Célérier, B., (1988). How much does slip on a reactivated fault plane constrain the stress tensor? Tectonics, **7**, no. 6, 1257-1278.

Chiba, K., Iio, Y., and Fukahata, Y., (2012). Detailed stress fields in the focal region of the 2011 off the Pacific coast of Tohoku EarthquakeImplication for the distribution of moment release. Earth Planets Space, **64**, no. 12, 1157-1165, doi: 10.5047/eps.2012.07.008.

Delouis, B., Giardini, D., Lundgren, and P., Salichon, J., (2002). Joint Inversion of InSAR, GPS, Teleseismic, and Strong-Motion data for the spatial and temporal distribution of earthquake slip: Application to the 1999 Izmit mainshock. Bull. Seism. Soc. Am., **92**, no. 1, 278-299, doi: 10.1785/0120000806.

Delouis, B., Lundgren, P., and Giardini, D., (2004). Slip distributions of the 1999 Düzce (Mw 7.2) and Izmit (Mw 7.6) earthquakes on the North Anatolian Fault (Turkey): A combined analysis. Internal report.

Ergin, M., Aktar, M., Bicmen, F., Yörük, A., Namik Yalcin, M., and Kuleli, S., (1997). Detailed microearthquake monitoring of the Izmit Bay Aktif Tektonik Arastirma Grubu Birinci Toplantisi, ITÜ Istanbul (in Turkish).

Etchecopar, A., Vausseur, G., and Daignieres, M., (1981). An inverse problem in microtectonics for the determination of stress tensors from fault striation analysis. Journal of Structural Geology, **3**, No. 1, 51-65.

Fisher, N., (1996). Statistical Analysis of Circular Data. Cambridge University Press, New York, NY, USA.

Flerit, F., Armijo, R., King, G., and Meyer, B., (2004). The mechanical interac-

tions between the propagating North Anatolian fault and the back-arc extension in the Aegean. Earth Planet. Sci. Lett., **224**, no. 3-4, p. 347-362, doi: 10.1016/j.epsl.2004.05.028.

Gephart, J., and Forsyth, D., (1984). An improved method for determining the regional stress tensor using earthquake focal mechanism data: Application to the San Fernando earthquake sequence. J. Geophys. Res., **89**, 9305-9320, doi: 10.1029/JB089iB11p09305.

Görgün, E., Bohnhoff, M., Bulut, F., and Dresen, G., 2010. Seismotectonic setting of the Karadere–Düzce brand of the North Anatolian Fault Zone between the 1999 İzmit and Düzce ruptures from analysis of Ïzmit aftershock focal mechanisms. Tectonophysics, **482**, 170-181, doi:10.1016/j.tecto.2009.07.012.

Hardebeck, J. L., and Hauksson, E., (2001). Crustal stress field in southern California and its implications for fault mechanics. J. Geophys. Res., **106**, No. B10, 21, 859-21, 882, doi: 10.1029/2001JB000292.

Hartleb., R. D., Dolan, J. F., Akyuz, H. S., Dawson, T. E., Tucker, A. Z., Yerli, B., Rockwell, T. K., Toraman, E., Çakir, Z., Dikbas, A., and Altunel, E., (2002). Surface rupture and slip distribution along the Karadere segment of the 17 August 1999 Izmit and western section of the 12 November 1999 Düzce, Turkey, Earthquakes. Bull. Seism. Soc. Am., **91**, no. 1, 67-78, doi: 10.1785/0120000829.

Hubert-Ferrari, H., Barka, A., Jacques, E., Nalbant, S. S., Meyer, B., Armijo, R., Tapponnier, P., and King, G. C. P., (2000). Lett. Nature, **404**, p. 269-273.

Ickrath, M., Bohnhoff, M., Bulut, F., and Dresen, G., (2014). Stress rotation and recovery in conjunction with the 1999 Izmit M_w 7.4 earthquake. Geophys. J. Int., **196**, 951-956, doi: 10.1093/gji/ggt409.

King, G. C. P., Hubert-Ferrari, A., Nalbant, S. S., Meyer, B., Armijo, R., and Bowman, D., (2001). Coulomb interactions and the 17 August 1999 Izmit, Turkey earthquake. Earth Planet. Sci., **333**, p. 557-569.

Kiratzi, A. A., (2002). Stress tensor inversions along the westernmost North Anatolian Fault Zone and its continuation into the North Aegean Sea. Geophys. J. Int. **151**, 360-376, doi: 10.1046/j.1365-246X.2002.01753.x.

Kuo, L. W., Li, H., Smith, S. A., Di Toro, G., Suppe, J., Song, S. R., Nielson, S., Sheu, H. S., and Si, J., (2013). Gouge graphitization and dynamic fault weakening during the 2008 Mw 7.9 Wenchuan earthquake. Geology, **42**, no. 1, p. 47-50, doi: 10.1130/G34862.1.

Le Pichon, X., Şengör, A.M.C., Demirbağ, Rangin, C., İmren C., Armijo, R., Görür, N., Çağatay, N., Mercier de Lepinay, B., Meyer, B., Saatçliar, R., and Tok, B., (2001). The active Main Marmara fault. Earth Planet. Sci. Lett., **192**, p. 595-616.

LePichon, X., Chamot-Rooke, N., and Rangin, C., (2003). The North Anatolian fault in the Sea of Marmara. J. Geophys. Res., **108**, no. B4, 2179, doi: 10.1029/2002JB001862.

McKenzie, D. P., (1969). The relation between fault plane solutions for earthquakes and the directions of the principal stresses. Bull. Seism. Soc. Am., **59**, No. 2, 591-601.

Meade, B. J., Hager, B. H., McClusky, S. C., Reilinger, R. E., Ergintav, S., Lenk, O., Barka, A., and Özener, H., (2002). Estimates of seismic potential in the Marmara Sea region from block models of secular deformation constrained by global positioning system measurements. Bull. Seism. Soc. Am., **92**, no. 1, p. 208-215.

Medina Luna, L., and Hetland, E. A., (2013). Regional stresses inferred from coseismic slip models of the 2008 Mw 7.9 Wenchuan, China, earthquake. Tectonophysics, **584**, 43-53, doi: 10.1016/j.tecto.2012.03.027.

Michael, A. J., (1984). Determination of stress from slip data: faults and folds. J. Geophys. Res., **89**, B13, 11,517-11,526, doi: 10.1029/JB089iB13p11517.

Michael, A. J., (1987). Use of focal mechanisms to determine stress: a control study. J. Geophys. Res., **92**, B1, 357-368. doi: 10.1029/JB092iB01p00357.

Mosegaard, K., Tarantola, A., (1995). Monte Carlo sampling solutions to inverse problems. J. Geophys. Res., **100**, 12,43112, 447.

Örgülü, G., 2011. Seismicity and source parameters for small-scale earthquakes along the splays of the North Anatolian Fault (NAF) in the Marmara Sea. Geophys. J. Int., **184**, 385-404, doi: 10.1111/j.1365-246X.2010.04844.x.

Parsons, T., Toda, S., Stein R. S., Barka, A., and Dieterich, J. H., (2000). Heightened odds of large earthquakes near Istanbul: An interaction- based probability calculation. Science, **288**, p. 661-665, doi: 10.1126/science.288.5466.661.

Pinar, A., Kuge, K., Honkura, Y., (2003). Moment tensor inversion of recent small to moderate sized earthquakes: implications for seismic hazard and active tectonics beneath the Sea of Marmara. Jeophys. J. Int., **153**, No. 1, 133-145, doi: 10.1046/j.1365-246X.2003.01897.x.

Pinar, A., Üçer, S. B., Honkura, Y., Sezgin, N., Ito, A., Bariş, Ş, Kalafat, D., Matsushima, M., and Horiuchi, S., (2010). Spatial variation of the stress field along the fault rupture zone of the 1999 Izmit earthquake. Earth Planets Space, **62**, p. 237-256.

Reilinger, R. E., Ergintav, S., Bürgmann, R., McClusky, S., Lenk, O., Barka, A., Gurkan, O., Hearn, L., Feigl, K. L., Cakmak, R., Aktug, B., Ozener, H., andÇakir Toksoz, M. N., (2000). Coseismic and Postseismic Fault Slip for the 17 August 1999, M = 7.5, Izmit, Turkey Earthquake. Science, **289**, 1519-1524, doi: 10.1126/science.289.5484.1519.

Schleicher, A. M., van der Pluijm, B. A., and Warr, L. N., (2010). Nano-coatings of clay and creep of the San Andreas Fault at Parkfield, California. Geology, **38**, p. 667-670, doi:10.1130/G31091.1.

Şengör, A.M.C., Tüysüz, O., İmren, C., Sakinç, M., Eyidoğan, H., Görür, N., Le

Pichon, X., and Rangin, C., (2005). The North Anatolian Fault: A New Look. Annu. Rev. Earth Planet. Sci., **33**, 37-112, doi: 10.1146/annurev.earth.32.101802.120415.

Silwal, V., and Tape, C., (2014). Seismic moment tensors in southern Alaska derived from body waves and surface waves. In Seismological Society of America Meeting Abstracts.

Stein, R., Barka, A. A., and Dieterich, J. H., (1997). Progressive failure on the North Anatolian fault since 1939 by earthquake stress triggering. Geophys. J. Int., **128**, 594-604, doi: 10.1111/j.1365-246X.1997.tb05321.x.

Tarantola, A., (2004). Inverse Problem Theory and Methods for Model Parameter Estimation. SIAM, Philadelphia.

Ucarkus, G., Çakir, Z., and Armijo, R., (2011). Western termination of the Mw 7.4, 1999 Izmit earthquake rupture: Implications for the expected large earthquake in the Sea of Marmara. Turkish J. Earth Sci., **20**, 383-398, doi: 10.3906/yer-0911-72.

Wallace, R., (1951). Geometry of shearing stress and relation to faulting. J. Geol., **59**, No. 2, 118-130.

Walsh, D., Arnold, R., and Townend, J., (2009). A Bayesian approach to determining and parametrizing earthquake focal mechanisms. Geophys. J. Int., **176**, 235-255, doi: 10.1111/j.1365-246X.2008.03979.x.

Warr, L. N., Wojatschke, J., Carpenter, B. M., Marone, C., Schleicher, A. M., and van der Pluijm, B. A., (2014). A "slice-and-view" (FIB-SEM) study of clay gouge from the SAFOD creeping section of the San Andreas fault at $\sim$ 2.7 km depth. J. Struc. Geology, **69**, p. 234-244.

CHAPTER 5

Conclusions and Future Work

In this dissertation, I develop and apply a Bayesian Monte Carlo estimation (BMC) technique with novel applications to both coseismic slip models and focal mechanisms. The technique is developed in order to infer the stresses that lead to earthquakes, to constrain uncertainties in stress, and to address the ambiguities that may arise from the use of focal mechanisms alone. The most commonly used methods to invert for stress rely on the use of focal mechanisms (Gephart and Forsyth, 1984; Michael, 1984); however, use of coseismic slip models to estimate stresses prior to large earthquakes has not been done prior to the work in this dissertation. I present the results from application of the BMC technique to geodetically constrained coseismic slip models of the 2008 Wenchuan, China, earthquake, the 1999 İzmit and Düzce, Turkey, earthquakes, to aftershocks from the 2008 Wenchuan earthquake, and focal mechanisms of earthquakes in the Sea of Marmara.

The BMC estimation results in samples of a posterior probability density distribution indicating likelihood of principal stress orientations and relative stress magnitudes. Constraining the likelihood of principal stress orientations allows quantification of uncertainties in the stress interpretation. Additionally, the BMC estimation is well adapted for considering complex coseismic slip models from multiple earthquakes that involve slip on pre-existing fractures with potentially non-optimal fault geometry.

5.1 Wenchuan coseismic slip models

Chapter 2 details the application of the BMC estimation technique on three geodetically constrained slip models of the 12 May 2008, M_w 7.9 Wenchuan, China, earthquake (Feng *et al.*, 2010; Tong *et al.*, 2010; Zhang *et al.*, 2011). During the Wenchuan earthquake, slip mechanism changed along the fault rupture from thrust to strike slip, leading some to believe that heterogeneous stresses led to such diversity in slip. Although slip propagated on fault segments with no large deviation in fault strike, models of fault geometry indicate fault dip varies along fault strike.

The purpose of studying the Wenchuan earthquake was therefore to test whether a homogeneous stress could produce the observed coseismic slip mechanism diversity, or whether a heterogeneous stress needed to be implored. Results indicate that a homogeneous state of stress is fully consistent with the transition of coseismic slip in the earthquake from predominantly thrust slip on shallow dipping fault segments, to predominantly strike slip on steeply dipping fault segments.. Additionally, I find that stresses are consistent with compression across the Longmenshan, with a nearly E-W trending, subhorizontal MCS, subhorizontal and N-S trending ICS, and a vertical LCS. I conclude that the distribution of slip along the Longmenshan is largely dictated by the change in fault geometry from SW to NE, and is defined by the tectonic history and reactivation of faults along the boundary of the eastern Tibetan Plateau and Sichuan Basin. Future work incorporating frictional parameters of faults will provide insight on the strength of the fault segments that coseismically slipped.

5.2 Stress Ambiguities and the Wenchuan Aftershocks

In Chapter 3, I use synthetic focal mechanisms to illustrate ambiguities in interpreting inferred stress from focal mechanisms representing coseismic slip on non-optimally oriented fault planes. Specifically, the likelihood of correctly distinguishing

the ICS from the MCS or LCS decreases when Δ is 1 or 0 (the magnitude of ICS = MCS or ICS = LCS, respectively). I then consider focal mechanisms of aftershocks following the Wenchuan earthquake from Cai *et al.*, (2011) to test whether inferred stress heterogeneities based on interpretation of aftershock focal mechanisms, proposed by Wang *et al.* (2009) and Cai *et al.* (2011) are simply due to ambiguities in the interpretation of stress from focal mechanisms alone.

Results indicate that ambiguities in the stress interpretation can explain the heterogeneities along the Wenchuan rupture proposed by Wang *et al.* (2009) and Cai *et al.* (2011). Assuming an informed prior where stress is compressional, homogeneous stresses are fully consistent with slip from three out of five groups of aftershock focal mechanisms with MCS subhorizontal and trending WSW-ENE, ICS subhorizontal trending NNW-SSE, and LCS vertical. The remaining two groups of aftershocks are located at either end of the Wenchuan rupture and indicate a rotation of stress, with MCS trending NW-SE, ICS trending NE-SW, and LCS remaining vertical.

Of the two groups of aftershocks, the southwestern group consists predominantly of reverse-slip events, while the northeastern group consists predominantly of strike-slip events. Therefore, the rotation of stress is not uniquely restricted to a specific slip mechanism or spatial region. The unique aspect of the strike-slip versus reverse-slip group of aftershocks is in the posterior of Δ, which indicates strike-slip groups favor low Δ, while reverse groups favor $\Delta > 0.5$.

That the rotation of stress is restricted to the southeast and northeast of the Wenchuan earthquake rupture is curious and leads to questions for future studies. One such questions is whether the coseismic stress changes in the mainshock led to rotation of stress in the southwest. However, the stress rotation in the northeast is further from the earthquake rupture, and thus stress changes may not have played a role in the rotation of stress in the northeast. Could the stress changes at the initiation and termination of the Wenchuan rupture be local stress heterogeneities that dictated

the extent of the Wenchuan earthquake rupture? To test whether local heterogeneities yield termination of slip along segments that coseismically ruptured, dynamic rupture models can incorporate the inferred stresses from focal mechanisms that I determined in this study. Additionally, topographic stresses in the southwest and northeast can be further investigated to test whether sedimentary overburden plays a part in the stress at either end of the fault rupture. These avenues for investigating rotation of stress are beyond the scope of this dissertation.

5.3 Westernmost North Anatolian Fault

In Chapter 4, I investigate the state of stress along the westernmost North Anatolian fault (NAF), in particular within the Sea of Marmara. A seismic gap in the Sea of Marmara indicates seismic risk for the city of Istanbul (e.g., Stein *et al.*, 1997; Parsons *et al.*, 2000; Hubert-Ferrari *et al.*, 2000; King *et al.*, 2001; Le Pichon *et al.*, 2003; Şengör *et al.*, 2005). Therefore, understanding the stresses in the region helps determine the slip mechanism potential on the Main Marmara fault (MMF) segments. Coseismic slip models of the İzmit and Düzce earthquakes that occurred to the east of the Sea of Marmara in 1999 are used to infer onshore stress of the westernmost NAF. Focal mechanisms of seismicity prior to 1999 and after 2003 that are located in the Sea of Marmara are used to infer stress on the MMF segments. Combined, the onshore and offshore stress inferences provide a snapshot of stress partitioning along the western NAF.

Coseismic slip models of the İzmit and Düzce earthquakes indicate that homogeneous stresses are fully consistent with coseismic slip on all fault segments, with MCS subhorizontal and trending NW-SE, ICS subhorizontal and trending NE-SW, and a vertical LCS. To understand whether the slip on fault segments from these coseismic slip models is consistent with Mohr-Coulomb failure, we incorporate a mechanical constraint on coefficient of fault friction, μ_f. Results indicate the same homogeneous

stress is consistent with all fault segments provided all fault segments are weak (low $\mu_f \lessapprox 0.2$). The need for low μ_f is driven by Karadere fault segment which deviates in strike from the predominantly E-W striking NAF. Alternatively, solutions in which μ_f is larger are permissible so long as μ_f on the Karadere segment is lower than μ_f on adjacent segments (as much as about 0.2 lower).

The MMF consists of the Çinarcik fault segment (ÇF), which connects to the east with the segments that ruptured during the İzmit earthquake, and the Western fault segment (WF). To the south lies the extensional Armutlu Peninsula. Stress inferences from focal mechanisms on the ÇF and WF segments indicate stress partitioning from east to west along the MMF. Stress prior to 1999 on the ÇF segment is consistent with a subhorizontal MCS trending nearly N-S, ICS off of vertical plunging to the west, and LCS off of vertical plunging to the east. On the WF segment, stress is consistent with a subhorizontal MCS trending E-W, near vertical ICS, and subhorizontal LCS trending N-S. Seismicity recorded after 2003 indicates a rotation of stress along the WF segment with a subhorizontal MCS trending NW-SE, vertical ICS, and subhorizontal LCS trending NE-SW. Such a rotation is not present on the ÇF segment. Stress in the Armutlu Peninsula is as expected with a normal state of stress inferred from focal mechanisms in that region.

The stress heterogeneity from onshore to offshore NAF may have played a role in the termination of the İzmit earthquake rupture. Testing this hypothesis requires dynamic rupture models incorporating the stress inferred from the İzmit-Düzce earthquakes and is beyond the scope of this study. Because there is no rotation of stress along the ÇF segment from 1999 to 2003, I do not believe stress changes in the mainshocks resulted in apparent stress rotation inferred along the WF segment during the same time period. Dynamic models of slip incorporating stresses inferred along the westernmost NAF that I present in this study can be used to estimate slip rupture propagation on both the WF and ÇF or whether the difference in stress can

potentially inhibit rupture to one fault segment.

5.4 References

Cai, C., Yu, C., Tao, K., Hu, X., Tian, Y., Zhang, H., Cui, X., Ning, J., (2011). Spatial distribution and focal mechanism solutions of the Wenchuan earthquake series: results and implications. Earthquake Science, **24**, 115125, doi: 10.1007/s11589-011-0775-5.

Feng, G., Hetland, E., Ding, X., Li, Z., and Zhang, L., (2010). Coseismic fault slip of the 2008 Mw 7.9 Wenchuan earthquake estimated from InSAR and GPS measurements. J. Geophys. Res., **37**, L01302, doi:10.1029/2009GL041213.

Gephart, J. and Forsyth, D., (1984). An improved method for determining the regional stress tensor using earthquake focal mechanism data: Application to the San Fernando earthquake sequence. J. Geophys. Res., **89**, 9305-9320, doi: 10.1029/JB089iB11p09305.

Hubert-Ferrari, H., Barka, A., Jacques, E., Nalbant, S. S., Meyer, B., Armijo, R., Tapponnier, P., and King, G. C. P., (2000). Lett. Nature, **404**, p. 269-273.

King, G. C. P., Hubert-Ferrari, A., Nalbant, S. S., Meyer, B., Armijo, R., and Bowman, D., (2001). Coulomb interactions and the 17 August 1999 Izmit, Turkey earthquake. Earth Planet. Sci., **333**, p. 557-569.

LePichon, X., Chamot-Rooke, N., and Rangin, C., (2003). The North Anatolian fault in the Sea of Marmara. J. Geophys. Res., **108**, no. B4, 2179, doi: 10.1029/2002JB001862.

Michael, A. J., (1984). Determination of stress from slip data: faults and folds. J. Geophys. Res., **89**, B13, 11,517-11,526, doi: 10.1029/JB089iB13p11517.

Parsons, T., Toda, S., Stein R. S., Barka, A., and Dieterich, J. H., (2000). Heightened odds of large earthquakes near Istanbul: An interaction- based probability calculation. Science, **288**, p. 661-665, doi: 10.1126/science.288.5466.661.

Şengör, A.M.C., Tüysüz, O., İmren, C., Sakinç, M., Eyidoğan, H., Görür, N., Le Pichon, X., and Rangin, C., (2005). The North Anatolian Fault: A New Look.

Annu. Rev. Earth Planet. Sci., **33**, 37-112, doi: 10.1146/annurev.earth.32.101802.120415.

Stein, R., Barka, A. A., and Dieterich, J. H., (1997). Progressive failure on the North Anatolian fault since 1939 by earthquake stress triggering. Geophys. J. Int., **128**, 594-604, doi: 10.1111/j.1365-246X.1997.tb05321.x.

Tong, X., Sandwell, D., and Fialko, Y., (2010). Coseismic slip model of the 2008 Wenchuan earthquake derived from joint inversion of interferometric synthetic aperture radar, GPS, and field data. J. Geophys. Res., **115**, B04314, doi: 10.1029/2009JB006625.

Wang., Q. C., Chen, Z. L., and Zheng, S. H., (2009). Spatial segmentation characteristic of focal mechanism of aftershock sequence of Wenchuan Earthquake. Chinese Sci. Bull., **54**, 2263-2270, doi: 10.1007/s11434-009-0367-0.

Zhang, G., Qu, C., Shan, X., Song, X., Zhang, G., Wang, C., Hu, J.C., and Wang, R., (2011). Slip distribution of the 2008 Wenchuan Ms 7.9 earthquake by joint inversion from GPS and InSAR measurements: A resolution test study. Geophys. J. Int. **186**, 207220, doi: 10.1111/j,1365 246X.2011.05039.x.

APPENDICES

APPENDIX A

Chapter 3 Supplement

A.1 Supplement to Potential Ambiguities in the Interpretation of Stress from Focal Mechanisms

Figures A.1 and A.2 are similar to Figures 3.2 and 3.3 of the main text, but correspond to the case when the directions of p_{MLE} the intermediate and least compressive stresses (ICS) and (LCS), respectively, are rotated around the MCS direction from the reference case. Figures A.3 and A.4 show the posteriors of the ICS and LCS, respectively, that correspond to the LCS_{60° case discussed in the main text, and are compliments to Figure 3.5. Figure A.5 shows the individual posteriors of MCS orientation inferred from four thrust mechanism aftershocks in the epicentral region of the Wenchuan earthquake (Figure 3.8), as well as the joint posterior consistent with these four focal mechanisms. Figure A.6 shows the orientations of the principal stress directions in the restricted prior in which LCS is steeply dipping.

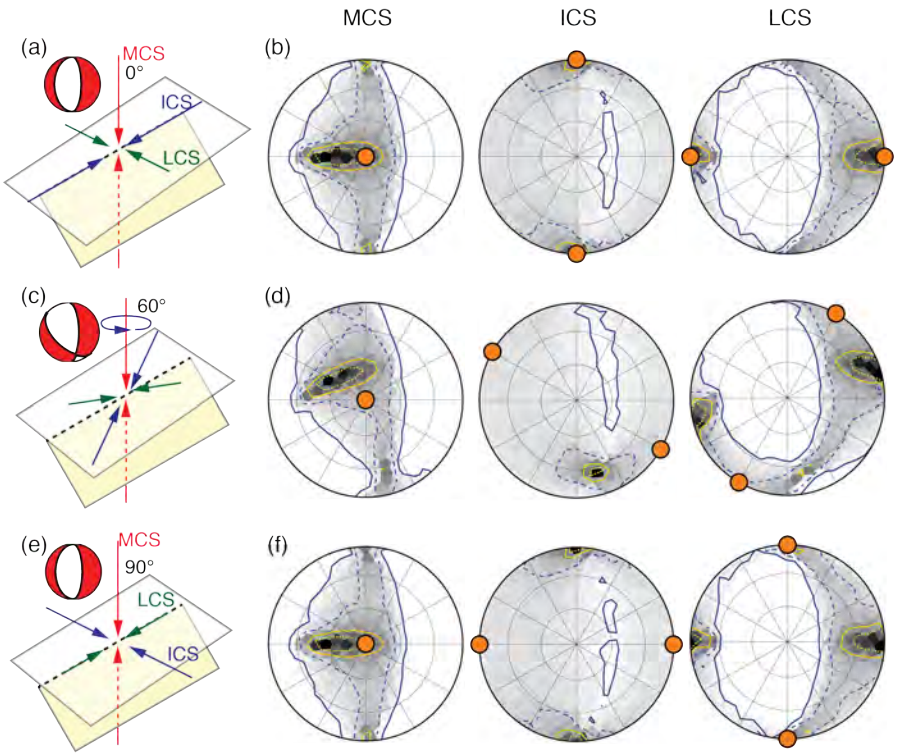

Figure A.1: Synthetic focal mechanisms and illustrations of the fault plane (shaded plane) and principal stresses (arrows) that led to that synthetic earthquake: (a) is the reference orientation, (c) is the MCS_{60° case, and (e) is the MCS_{90° case. Orientations of the principal stresses (solid dots) associated with the synthetic focal mechanisms in the reference (b), MCS_{90° (d), and MCS_{90° (f) cases, along with the posteriors estimated from the nodal plane corresponding to the fault in the associated synthetic focal mechanisms. Posteriors are shown as probability mass functions in Lambert projections of the lower hemisphere: contours indicate the $0.01p_{MLE}$ (dark solid line), $0.2p_{MLE}$ (dark dashed line), $0.5p_{MLE}$ (solid light line), and $0.75p_{MLE}$ (light dashed line) levels, where p_{MLE} is the maximum density; shading indicates density of samples in the posterior, with black indicating highest density (i.e., highest likelihood) and white indicating zero density (i.e., zero likelihood).

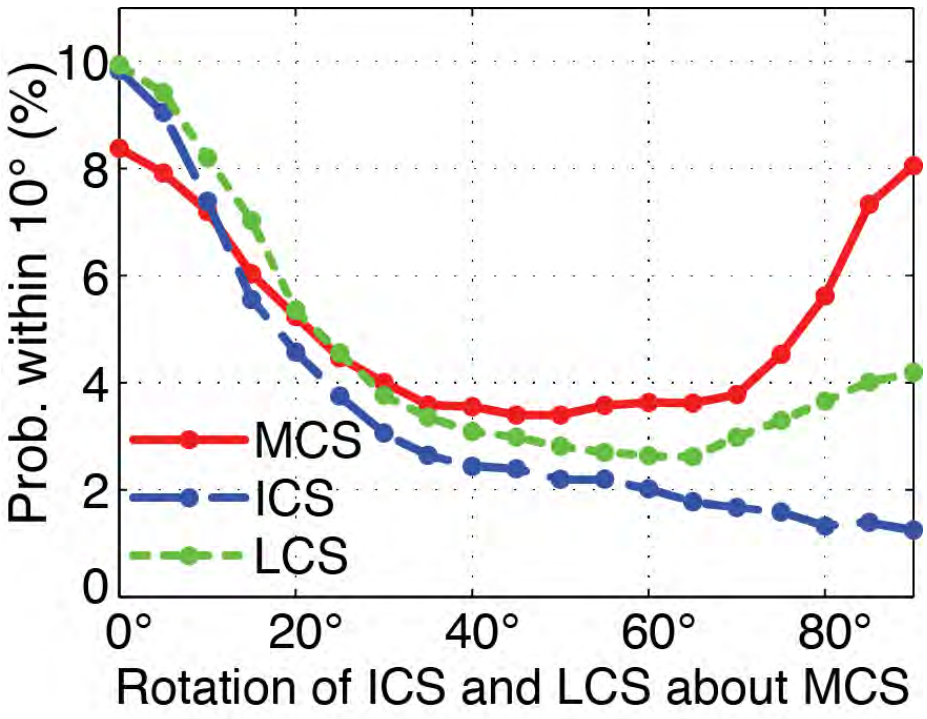

Figure A.2: Probability of correct stress interpretation, MCS_{90° case. Posterior probability of MCS, ICS, or LCS orientations within 10° of the actual orientations (solid dot) estimated from synthetic focal mechanisms generated by progressively rotating ICS and LCS about the MCS orientation in the reference orientation.

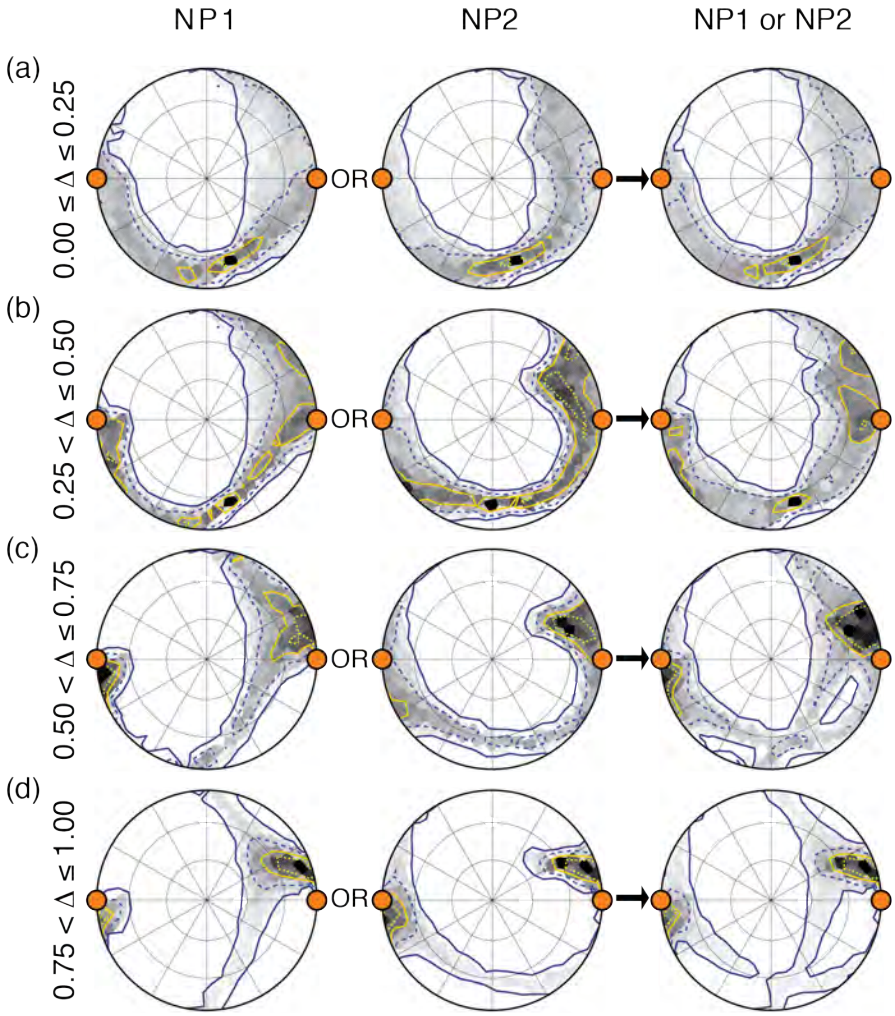

Figure A.3: Posteriors of LCS orientation estimated from the LCS_{60° case, assuming restricted priors on Δ (rows) and that NP1 (left panels), NP2 (center panels), or either (right panels) corresponds to the fault plane. Priors on Δ are that Δ is equally likely within the ranges [0.00, 0.25] (a), [0.25, 0.50] (b), [0.50, 0.75] (c), or [0.75, 1.00] (d). Contours and shading are as in Figure A.1, and solid dots are the true orientation of LCS.

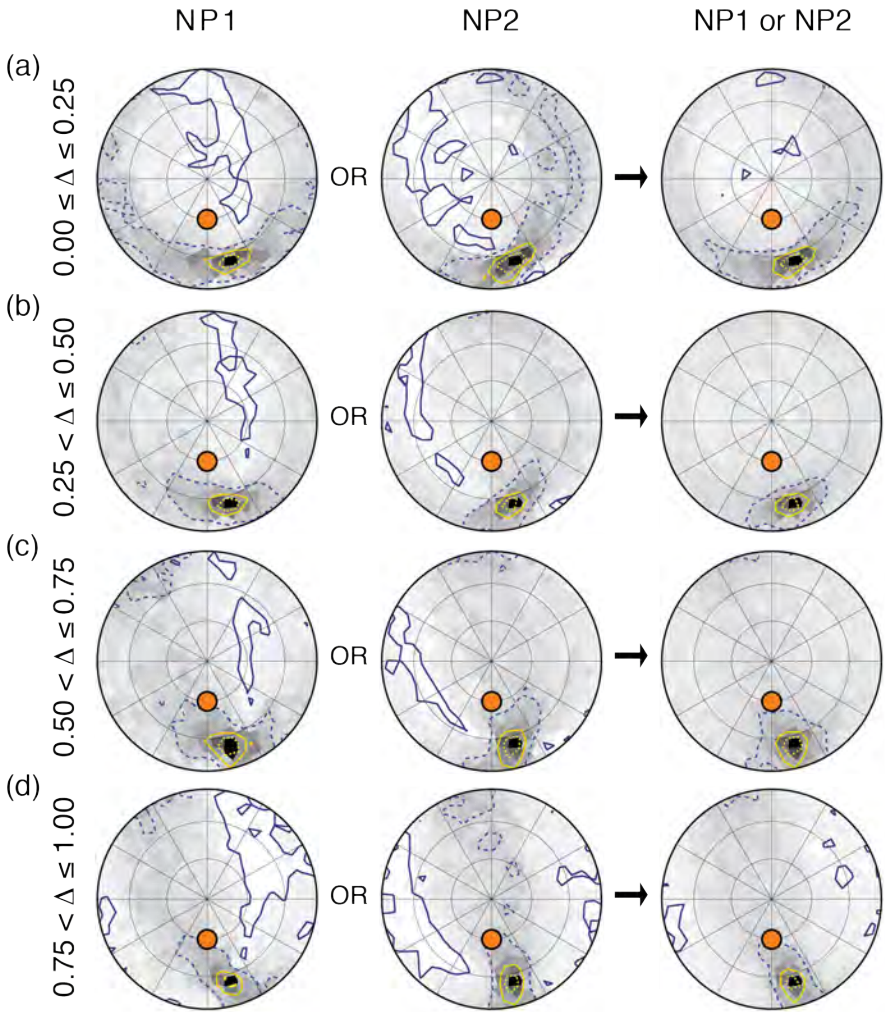

Figure A.4: Posteriors of ICS orientation estimated from the LCS_{60° case, assuming restricted priors on Δ (rows) and that NP1 (left panels), NP2 (center panels), or either (right panels) corresponds to the fault plane. Priors on Δ are that Δ is equally likely within the ranges [0.00, 0.25] (a), [0.25, 0.50] (b), [0.50, 0.75] (c), or [0.75, 1.00] (d). Contours and shading are as in Figure A.1, and solid dots are the true orientation of ICS.

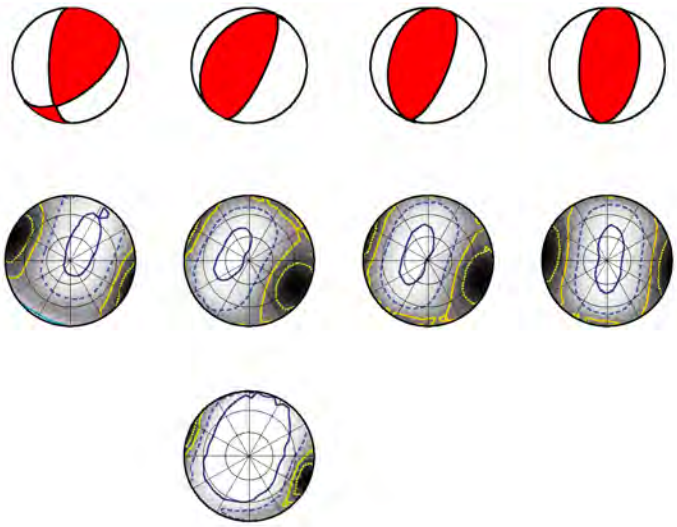

Figure A.5: (top row) Focal mechanisms of four thrust mechanism aftershocks in the epicentral region of the Wenchuan earthquake (Figure 3.8). (middle row) Associated posteriors of MCS orientation estimated from the focal mechanisms above. (bottom panel) Joint posterior of MCS orientation estimated from these four focal mechanisms. Posteriors are shown as probability mass functions in a Lambert projection of the lower hemisphere: contours indicate the $0.01p_{MLE}$ (dark solid line), $0.2p_{MLE}$ (dark dashed line), $0.5p_{MLE}$ (solid light line), and $0.75p_{MLE}$ (light dashed line) levels, where p_{MLE} is the maximum density; shading indicates density of samples in the posterior, with black indicating highest density (i.e., highest likelihood) and white indicating zero density (i.e., zero likelihood).

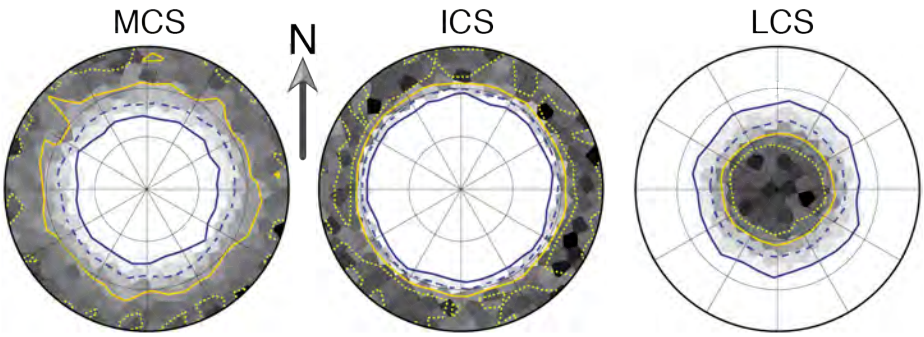

Figure A.6: Orientations of the MCS, ICS and LCS in a restricted prior in which the LCS is assumed to be steeply dipping.

APPENDIX B

Chapter 4 Supplement

B.1 Supplement to State of Stress along the western-most North Anatolian Fault

This appendix contains additional figures of posteriors of stress from the İzmit and Düzce earthquakes and focal mechanisms of earthquakes prior-to and following the 1999 earthquakes.

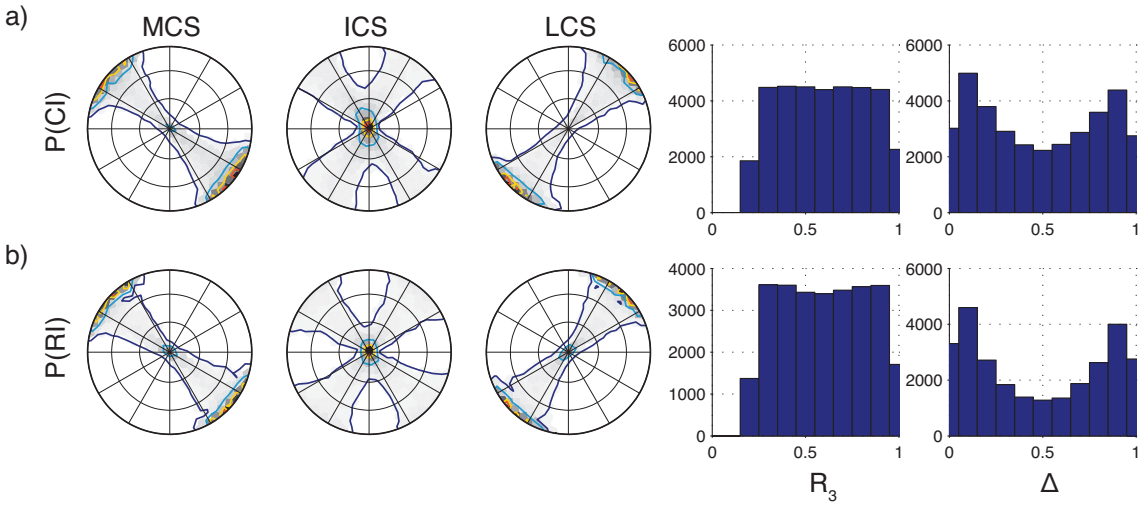

Figure B.1: Principal stress orientations, R_3, and Δ of stress models consistent with the (a) CI and (b) RI coseismic slip models. Posteriors are shown as probability mass functions in Lambert projections of the lower hemisphere: contours indicate the $0.01p_{\mathrm{MLE}}$ (dark blue), $0.2p_{\mathrm{MLE}}$ (light blue), $0.5p_{\mathrm{MLE}}$ (yellow), and $0.75p_{\mathrm{MLE}}$ (red) levels, where p_{MLE} is the maximum density; shading indicates density of samples in the posterior, with black indicating highest density (*i.e.*, highest likelihood) and white indicating zero density (*i.e.*, no likelihood).

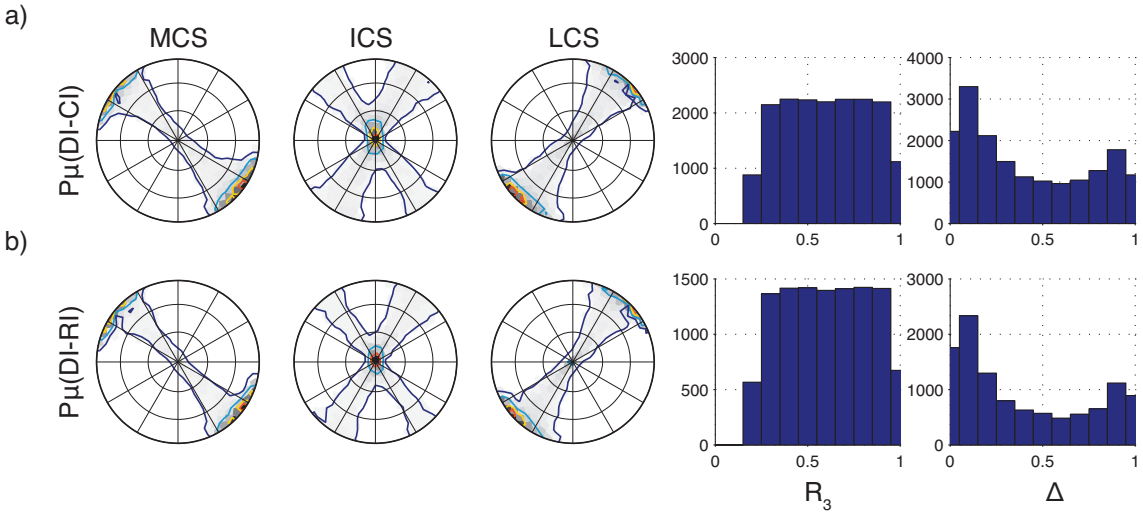

Figure B.2: Principal stress orientations, R_3, and Δ of stress models consistent with both (a) DI and CI coseismic slip models and (b) DI and RI coseismic slip models. Posteriors are shown as probability mass functions in Lambert projections of the lower hemisphere with contours as in B.1.

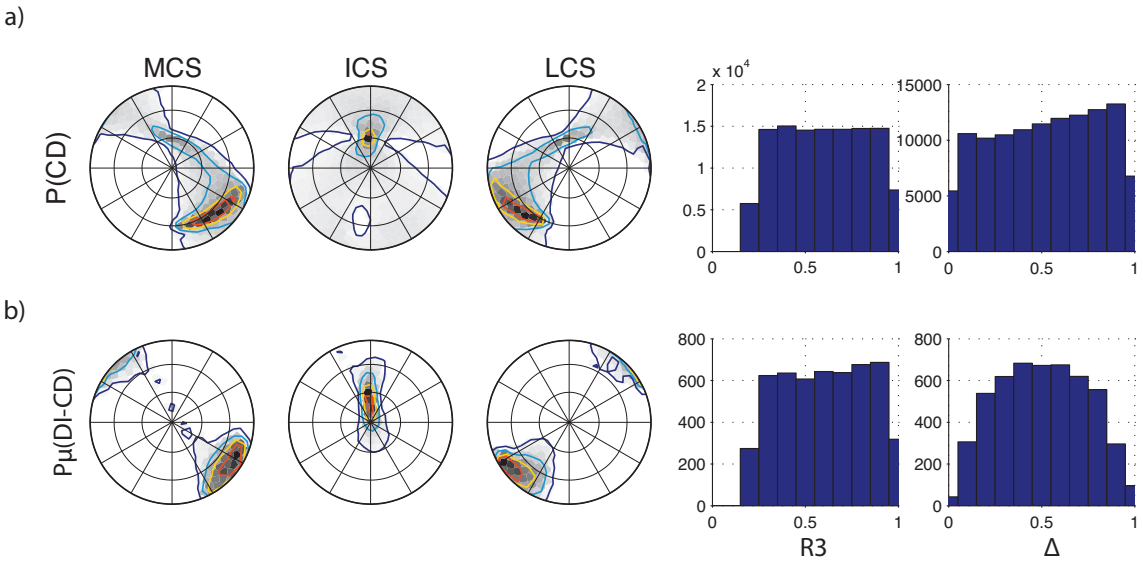

Figure B.3: Principal stress orientations, R_3, and Δ of stress models consistent with the CD coseismic slip model. Posteriors are shown as probability mass functions in Lambert projections of the lower hemisphere with contours as in B.1.